INFRARED MEASUREMENT OF BIOMASS COMBUSTION IN A WIRE MESH REACTOR

A THESIS SUBMITTED TO
THE GRADUATE SCHOOL OF NATURAL AND APPLIED SCIENCES
OF
MIDDLE EAST TECHNICAL UNIVERSITY

BY

KIVANÇ ULUCA

IN PARTIAL FULFILLMENT OF THE REQUIREMENTS
FOR
THE DEGREE OF MASTER OF SCIENCE
IN
MECHANICAL ENGINEERING

AUGUST 2019

Approval of the thesis:

INFRARED MEASUREMENT OF BIOMASS COMBUSTION IN A WIRE MESH REACTOR

submitted by **KIVANÇ ULUCA** in partial fulfillment of the requirements for the degree of **Master of Science in Mechanical Engineering Department, Middle East Technical University** by,

Prof. Dr. Halil Kalıpçılar
Dean, Graduate School of **Natural and Applied Sciences** _____

Prof. Dr. M. A. Sahir Arıkan
Head of Department, **Mechanical Engineering** _____

Assist. Prof. Dr. Feyza Kazanç Özerinç
Supervisor, **Mechanical Engineering, METU** _____

Examining Committee Members:

Prof. Dr. İlker Tarı
Mechanical Engineering, METU _____

Assist. Prof. Dr. Feyza Kazanç Özerinç
Mechanical Engineering, METU _____

Prof. Dr. Ahmet Yozgatlıgil
Mechanical Engineering, METU _____

Prof. Dr. Hakan Altan
Physics, METU _____

Prof. Dr. Murat Köksal
Mechanical Engineering, Hacettepe University _____

Date: 29.08.2019

I hereby declare that all information in this document has been obtained and presented in accordance with academic rules and ethical conduct. I also declare that, as required by these rules and conduct, I have fully cited and referenced all material and results that are not original to this work.

Name, Surname: Kıvanç Uluca

Signature:

ABSTRACT

INFRARED MEASUREMENT OF BIOMASS COMBUSTION IN A WIRE MESH REACTOR

Uluca, Kıvanç
Master of Science, Mechanical Engineering
Supervisor: Assist. Prof. Dr. Feyza Kazanç Özerinç

August 2019, 104 pages

As a consequence of increasing emissions due to the global energy production, new clean combustion options which utilize biomass are being sought. Prior to using biomass in an industrial boiler, the combustion characteristics of the fuel have to be assessed so that the boiler and furnace can be designed or retrofitted. In this study, olive residue (OR), endogenous agricultural residue of Turkey was investigated using a wire mesh reactor (WMR) coupled with two infrared cameras. These cameras recorded radiometric data in mid-wave, 3-5µm, and long-wave, 8-12µm, infrared band. Infrared thermal imaging was used for the first time to observe the combustion of single fuel particles in a WMR. 2D thermal scanning of the WMR that operates at 1100℃ was performed to verify homogenous temperature distribution along the mesh and it was observed that the mesh operates within ~40℃ of average deviation. Single particle combustion experiments with OR particles with mass ranging 5-15mg were conducted to obtain ignition delay time, volatile and char combustion durations from the thermal radiation originated from combustion. Tunçbilek (TL) lignite samples (3mg) were selected for comparison purposes. The observations showed that in order to obtain similar burnout durations, a TL particle with ~3mg and a heavier OR particle ~11mg should be combusted. OR particles were observed to combust in two phases: volatile combustion followed by char combustion. The ignition delay time of OR did

not have a direct relation with the particle mass since the process was initiated with gas-phase reactions. Oppositely, the particle mass influenced the volatile, char, and total combustion durations. Volatile, char combustion and burnout times were longer with increasing particle mass. An OR particle with an average mass of 10mg, burned out in 21s where 2s of volatile and 19s of char combustion. In addition, ignition delay time and char ignition time of the particle was measured as 9s and 11s respectively.

Keywords: Infrared, Combustion, Biomass, Wire Mesh, Single Particle

ÖZ

TEL ÖRGÜ REAKTÖRÜ KULLANILARAK BİYOKÜTLE YANMASININ KIZILÖTESİ ÖLÇÜMÜ

Uluca, Kıvanç
Yüksek Lisans, Makina Mühendisliği
Tez Danışmanı: Dr. Öğr. Üyesi Feyza Kazanç Özerinç

Ağustos 2019, 104 sayfa

Dünyada artan enerji üretimi sebebiyle, biyokütlenin kullanıldığı yeni temiz yanma seçenekleri araştırılmaktadır. Güç santrallerinin kazanlarında biyokütlenin kullanılabilmesi için, yakıtın yanma karakteristiklerinin belirlenmesi ve yakıcı tasarımının da uygun şekilde değiştirilmesi gerekmektedir. Bu çalışmada Türkiye'de yetişen zeytin tortusunun tel örgü reaktöründe tek parçacık yanması ilk defa 3-5µm orta bant ve 8-12µm uzun bant kızılötesinde yanma reaksiyonundan kaynaklanan termal radyasyon ölçülerek analiz edilmiştir. Tel örgünün sıcaklık dağılımının homojen olduğunu göstermek ve düzeneği geçerlemek amacıyla 1100°C sıcaklıktaki tel örgünün iki boyutlu sıcaklık dağılımı analizi gerçekleştirilmiştir ve tel örgü boyunca ortalama ~40°C sapma tespit edilmiştir. 5 ile 15mg kütleli zeytin tortusunun tek parçacık yanma deneyleri gerçekleştirilerek uçucu, kor ve toplam yanma süreleri radyometrik olarak hesaplanmıştır. Parçacık kütlesinin etkisinin yanma gecikme süresine etkisi araştırılmıştır. 3mg kütleli Tunçbilek linyiti parçaları yanma fazlarının kıyaslanması amacıyla tek parçacık yanma deneylerinde kullanılmıştır. Karşılaştırma sonucunda ortalama 3mg kütleli Tunçbilek linyitinin yanma süresini verebilmesi için yaklaşık 11mg kütleli zeytin tortusu parçacığı yakılması gerektiği çıkarımı yapılmıştır. Zeytin tortusunun yanma gecikmesinin parçacık kütlesi üzerine doğrudan etkisi yanmanın gaz fazında gerçekleşmesinden dolayı gözlemlenmemiştir; ancak uçucu ve

kor yanmasının parçacık kütlesini doğrusal olarak etkilediği hesaplanmıştır. 10mg civarı kütleli zeytin tortusunun toplam 21 saniyede yandığı, 2 saniyesinin uçucu, 19 saniyesinin kor yanması olduğu tespit edilmiştir. Uçucu ve kor yanma gecikme süreleri ise 9 ve 11 saniye olarak hesaplanmıştır.

Anahtar Kelimeler: Kızılötesi, Yanma, Biyokütle, Tel Örgü, Tek Parçacık

To My Family

ACKNOWLEDGEMENTS

Firstly, I would like to express my deepest appreciation to my supervisor, Asst. Prof. Dr. Feyza Kazanç Özerinç for providing invaluable guidance throughout this research. Her everlasting patience and prescience made this research possible. I would also like to extend my appreciation to Mammadbaghir Baghirzade for helping me out during the experiments. Without Dr. Duarte Magalhães's emotional support and review process, this study would not be finished. I would also like to thank Advanced Technologies Research Institute of The Scientific and Technological Research Council of Turkey (TÜBİTAK İLTAREN), my coworkers from infrared technologies department Umut Kayıkcı, Emrah Oduncu and my director Dr. Mustafa Sivaslıgil. This thesis would not be complete without their never-ending support. I deeply thank Irmak Özvarış for making my life a lot bearable through recent years. Lastly, I would like to thank my family, Gülşen Uluca and Yavuz Uluca who always believed in me and did everything they can for me. Their patience, support and motivation made me who I am right now.

TABLE OF CONTENTS

LIST OF TABLES

TABLES

LIST OF FIGURES

FIGURES

CHAPTER 1

INTRODUCTION

In today's world; due to the population growth and a more energy demanding lifestyle, the total amount of energy production increases daily. The increasing trend to generate more electricity comes with a drawback which is the emission of pollutants such as CO_2, NO_x, and SO_x, as well as particulate matter to the atmosphere. As global awareness about the damage inflicted on the planet has been raised, countries have started to focus on renewable energy sources like solar, wind, hydro, geothermal and biomass.

The importance of biomass as an energy source is noticeable in countries in which the coal fired power plants still play a significant role in the energy mix due to the fact that coal can be co-fired with various biomass types. Investigation of biomass energy sources has therefore become important in last the decades, since combustion of biomass and coal together provides considerable diminution in CO_2 emission as a consequence of biomass being carbon neutral.

Specifically for Turkey, based on the latest report released in 2017 by the Energy Market Regulation Institute of Turkey (EPDK, 2017), as shown in Table *1.1*, fossil fuels had supplied 71.2% of the total energy demand in Turkey. Specifically, those fossil fuels were stated as natural gas and coal with 37.18% and 33.05% of the total energy produced, respectively. The data underlines the fact that Turkey is still much dependent on coal for electricity production and needs to utilize clean combustion methods to decrease the associated emissions. Table *1.1* also shows that biomass utilization in MWh of electricity produced in Turkey increased by 26.05% when compared to the previous year, 2016. Moreover, the Energy and Natural Resources Ministry of Turkey states that Turkey's biomass waste potential is around 8.6 million

tons of equivalent petrol (Energy and Natural Resources Ministry of Turkey, 2018). Turkey presents a strong agricultural production with the subsequent generation of a variety of agricultural waste that can be used as energy source.

Since Turkey is one of the major olive producers and exporters in the world (Ministry of Customs and Trade, 2018), olive residue has the potential for electricity generation. It is also reported that Turkey produces 450,000 tons of olive per year, standing as the third major producer and in fourth place in terms of olive oil produced per year with 263,000 tons The given amount of olive production and its by-products result in great potential to use olive residue as a renewable source of energy for Turkey.

Table 1.1. *Amount of Energy Produced by Source in Turkey* (EPDK, 2017)

Source	*2016 Value (MWh)*	*Share (%)*	*2017 Value (MWh)*	*Share (%)*	*2016-2017 Change (%)*
Natural Gas	88,244,574	32.38	108,771,841	37.18	23.26
Imported Coal	47,741,879	17.52	51,172,215	17.49	7.19
Hydro Dam	48,906,203	17.94	41,278,222	14.11	-15.60
Lignite	38,543,567	14.14	40,545,711	13.86	5.19
Wind	15,501,030	5.69	17,859,858	6.10	15.22
River	18,396,857	6.75	17,130,234	5.85	-6.88
Geothermal	4,818,523	1.77	5,969,481	2.04	23.89
Hard Coal	3,292,613	1.21	3,453,865	1.18	4.90
Asphaltite Coal	2,873,837	1.05	2,394,637	0.82	-16.67
Biomass	1,590,695	0.58	2,005,069	0.69	26.05
Diesel	1,554,168	0.57	1,008,826	0.34	-35.09
Fuel Oil	1,054,049	0.39	957,859	0.33	-9.13
Sun	2,636	0.00	24,557	0.01	831.35
LNG	42,988	0.02	2,196	0.00	-94.89

Before the utilization of a certain biomass in industrial scale furnaces and boilers, its combustion characteristics have to be investigated. Single particle combustion experiments provide a wide array of data such as ignition delay and burnout times which are analyzed to determine the way that biomass is processed and co-fired in boilers. Moreover, an efficient industrial boiler design also relies on well characterization of the fuel. In order to emulate industrial conditions, like high heating rates and high temperatures, wire mesh reactor can be used with high flexibility, i.e., various types of fuel, temperature, atmosphere composition, can be independently selected for the combustion experiments. A wire mesh reactor setup can be constructed on desktop in a laboratory with a controllable power source that can supply high amount of current to heat up the metal wire meshes to ignite the combustion process. Both configurations, single layer of particles between horizontal meshes and single particle between vertical meshes can be adapted to the reactor.

In single particle combustion experiments with wire mesh reactor, the fuel particle is heated and ignited between two meshes. The preponderant heat transfer modes are radiation and conduction. The combustion process is monitored over time to obtain the desired parameters such as the ignition delay time, the volatile and char combustion times and the burnout time This kind of research had been done by researchers (Flower & Gibbins, 2009; Riaza, Gibbins, & Chalmers, 2017), with cameras that can detect visible light and utilization of image processing techniques. On the contrary, radiometric cameras can detect the thermal radiation originated from the combustion reaction in a specific wavelength interval of the electromagnetic spectrum; similarly a measurement of single particle combustion has been previously conducted by researchers (Bejarano & Levendis, 2008).

CHAPTER 2

LITERATURE REVIEW

2.1. Biomass and Coal

Biomass is an organic compound originated from industrial and agricultural wastes or residues (Koppejan, 2012). As biomass forms in nature, it transforms energy of the sun, gathered by means of photosynthesis, to chemical energy in between the molecular bonds. Biomass, as a fuel, is considered to be CO_2 neutral in terms of emission due to the combustion, because the released CO_2 product of the combustion was absorbed from the atmosphere in the first place (Sami, Annamalai, & Wooldridge, 2001). Hence, biomass is considered as a sustainable source of energy. Moreover, the energetic content of biomass, coupled with the reduction in SO_x and NO_x emissions compared to fossil fuels, enables it as a preferable energy source (Gan et al., 2012).

Depending on the type and origin of the biomass, composition and structure change and those differences have a significant impact on processes that are used to obtain energy from fuel (Trubetskaya, Glarborg, Jensen, Jensen, & Shapiro, 2016). Harvesting and storage conditions of biomass also have an effect on the composition of it by determining the amount of inorganic matter which are alkaline metals, phosphates, chlorides, sulphates and oxides (Koppejan, 2012).

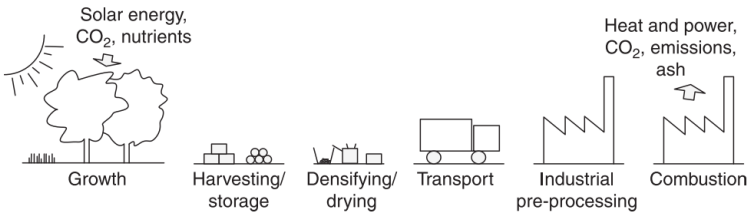

Figure 2.1. Overview of Processes Involved in Biomass Utilization (Mandø, 2013)

Chemical composition of biomass varies from coal since its content of volatile, moisture and elements like Cl, Ca, Mg, Na are higher. According to a previous work (Demirbas, 2004) richness of biomass in terms of volatile matter makes it preferable in thermochemical reactions because of the high reactivity attributed to it. On the other hand, the heating value of biomass is not as high as that of solid fossil fuels since it has low carbon and high oxygen content.

There are many thermochemical applications that are being performed to extract the energy content in biomass fuels (Linghong Zhang, Xu, & Champagne, 2010). Those processes can be named as pyrolysis, gasification and combustion. When the biomass is burned in a combustion process, rapid thermal energy is released which enables achieving moderately high temperatures, 800-1600 °C, and extract heat and/or power by means of a thermodynamic cycle (Brown, 2011).

Because of the large agricultural areas and activities in Turkey, there are various biomass sources available. Agricultural and agroforestry residues can have been widely used as a source of energy to generate electricity since the share of biomass is 52% of domestic energy consumption which is 37% of Turkey's total energy consumption (Gokcol, Dursun, Alboyaci, & Sunan, 2009). Among the agricultural crops grown in Turkey, almond, hazelnut, walnut and olive remain as the most popular biomass fuels and the residues obtained from these are husk, shell and bagasse (Gokcol et al., 2009).

Table 2.1. *Structural and Ultimate Analysis of Olive Residue* (Demirbaş, 2002)

	Olive Residue (wt. % daf)
Hemicelluloses	9.4
Cellulose	36.2
Lignin	54.3
Carbon	48.3
Hydrogen	6.2
Oxygen	44.7
Nitrogen	0.7
Sulphur	0.1
Ash	2.3
High Heating Value (MJ/kg)	19

In Turkey, biomass type olive residue stands out among other sources in terms of availability. In Table *2.1*, the chemical composition and heating value of olive residue from Adana province of Turkey is presented (Demirbaş, 2002). Cultivation of olive in Turkey is done mainly for olive oil production. According to a previous research (Yuzbasi & Selçuk, 2011), Turkey is ranked among the top olive producers in the world along with Spain, Portugal and Italy. From the year 2000 to 2015, the amount of produced olive in Turkey increased from 1.2 to 1.7 million tons (Gürkan, 2015). The increasing trend in olive production resulted in widespread availability of olive residue to be used as an energy source.

Coal is a fossil fuel which consists of organic matters from former plant residues, minerals, volatile gases and water (Neavel, 1981). Compositional variations affect the thermal process that the coal is being subjected to and, subsequently, the efficiency of the process. After the combustion of coal, the organic matters (macerals), are burned and the inorganic part (minerals) are left in form of ashes. The inorganic content of coal can cause corrosion, erosion, as well as surface deposition on thermal power

plants boilers surfaces (van Lith, Alonso-Ramirez, Jensen, Frandsen, & Glarborg, 2006).

Coals are classified in four types based on their carbon content. Namely, in descending carbon content, anthracite, bituminous, subbituminous and lignite. The lower the carbon content, the higher amount of moisture and volatiles, or H, O, S elements, are available in it (Vassilev, Kitano, & Vassileva, 1996). Coals can also be classified in terms of ash composition: lower rank coals include higher amount of compounds like CaO, MgO, whereas the ash from higher ranked coals includes mainly Al_2O_3 and SiO_2 (Vassilev et al., 1996).

As Turkey generates most of its energy from fossil fuels (see *Table 1.1*), coal has a significant importance in the energy mix. Some Turkish coals which are used in power generation are, Soma lignite, Afşin Elbistan lignite, Tunçbilek lignite and their installed capacities are 1494 MW, 2795 MW and 365 MW respectively. These coals are characterized by a low amount of fixed carbon, high Sulphur content, moisture and ash.

2.2. Biomass and Coal Combustion

Combustion is defined as the exothermic oxidation reaction of a fuel in which enough heat is produced to make a self-sustaining reaction (Glassman & Yetter, 2008). In order to ignite a fuel, oxygen and sufficient heat energy to start the reaction are required and sustainability of the combustion process depends on the amount of available oxygen until the fuel is burned completely. Combustion of organic matters yields CO_2 and H_2O in vapor form with other products related to the content of fuel.

Combustion of a solid fuel particle consists of several stages that occur in order. As the particle is being heated; the water found in the fuel, moisture, is released from the particle drying stage. Following the drying stage, volatile matters of the fuel begin to diffuse through the pores in the particle in gas form which - devolatilization stage.

Drying and devolatilization stages take a relatively short time when compared to the other stages. The released volatiles, with the help of the heat supplied to the particle, react with oxygen and are burned. After the volatile combustion stage and the extinction of volatile flames, the char part of the fuel is ignited. The char combustion duration covers most of the total combustion duration (Mandø, 2013), and can also overlap with the combustion of volatiles. The procedure of combustion is shown in Figure 2.2.

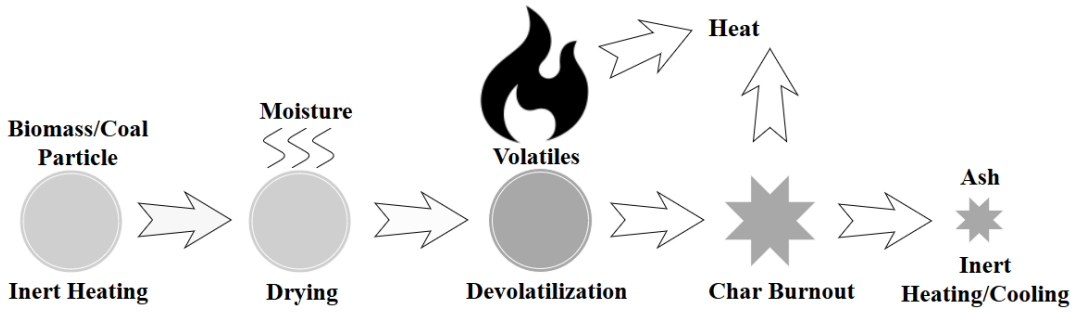

Figure 2.2. Combustion Stages of a Solid Fuel Particle

Solid fuel combustion can occur either in one-phase or two-phase. One phase combustion is defined as the sequential burning of volatiles and char, whereas in two-phase the volatiles and char burn simultaneously (Riaza et al., 2014b). Specifically, biomass particles display a two phase of combustion, as it is observed by different researches undertaken with single particle devices (Levendis, Joshi, Khatami, & Sarofim, 2011; Marek & Wiatkowski, 2015; Riaza et al., 2014b). When a biomass particle's combustion is monitored thermally, in the heating curve, the first and second peak corresponds to volatile and char combustion, sequentially (Riaza et al., 2014a). Contrarily, in lignite coal combustion, since the amount and composition of volatiles differ greatly from that of biomass, a one-phase combustion is observed (Bejarano & Levendis, 2008).

Both fuels', biomass and coal, chemical composition and the heating rate of combustion, moisture content of the fuel heavily impacts the combustion characteristics (Mandø, 2013). The combustion reaction of a hydrocarbon fuel with atmospheric air is given in Figure 2.3.

$$C_\alpha H_\beta O_\gamma N_\delta S_\varepsilon + n\,(3.76\,N_2 + O_2) \xrightarrow{yields} aCO_2 + bH_2O + cO_2 + dN_2 + eCO + fNO_x + gSO_x$$

Figure 2.3. Combustion Reaction of a Hydrocarbon Fuel

There are several challenges encountered upon firing coal and biomass. Pollutant formation is by far the greatest drawback of coal and biomass combustion, with an impact on the environment and human health. Specifically, combustion of lignite coal which has low carbon and high of Sulphur content results in the emission of greenhouse gases such as CO_2, NO_x and SO_x. The combustion of biomass, which is considered a carbon-neutral fuel and furthermore typically has low Sulphur, still results in the emission of NO_x gases. Strategies to mitigate NO_x emission usually consist of (a) reduction of NO_x to N_2 using a catalytic or non-catalytic agent; and (b) use of low-NO_x burners that reduce the peak temperature of the flame and prevent the formation of thermal NO_x (Riaza, Mason, Jones, Gibbins, & Chalmers, 2019).

Moreover, for both coal and biomass, the formation of particulate matter (PM) is particularly acute and induces cardiovascular diseases and lung cancer that lead to premature death (WHO, 2013). Electrostatic precipitators are a common equipment in a coal or biomass plant and have high capture efficiencies for super micron PM. However, during combustion of biomass, the formation of submicron PM is predominant, and this PM cannot be easily sequestrated.

In industrial power plants to reduce pollutant formation, it has become increasingly popular to co-fire biomass and coal together, especially in countries which need to

reduce emissions of CO_2, NO_x and SO_x urgently. There are researches in literature that points out the NO_x reduction effect of co-firing (H Liu, 1995; Sami et al., 2001). According to the researchers, in co-firing hydrocarbons of volatile matters, reduce NO_x emissions of combustion products by converting them to N_2, consequently higher amount of volatile matter in the fuel results in a decrease in emission products. It has been proven that co-firing of olive residue with lignite in a bubbling fluidized bed combustor improved combustion efficiency and reduced N_2O and SO_2 emissions (Gogebakan, Gogebakan, & Selçuk, 2008). Based on a scientific study (Li Zhang, Xu, Zhao, & Liu, 2007) that investigates the synergy of co-firing, when biomass and coal were used together as a fuel, an increase in char reactivity, improvement in quality of pyrolysis products and high yields of tar were observed. In order to achieve benefits of co-firing biomass and coal together, the fuels have to be characterized individually before the utilization.

2.3. Wire Mesh Reactor Studies

In the last decade, the wire mesh reactor has been used as a setup for conducting experiments on solid fuel combustion. The crucial property of this experimental combustion setup is its ability to simulate conditions that are close to real power plant operation, like high heating rates and high temperatures (Paterson, Kandiyoti, Dugwell, Wu, & Gao, 2008). A wire mesh reactor can reach those conditions with the added benefits of compactivity, flexibility and cost efficiency.

Earliest wire mesh reactor was built around 1960s and initially used for pyrolysis experiments (Cogliano, 1963). Later on, a direct current reactor was used (Finch & Taylor, 1969) to study solid fuel properties under high heating rates. Optical transmission windows were also designed for both high speed camera imaging and temperature measurement with a pyrometer.

The most significant contribution in the past decade to improve and modernize the pre-existing wire mesh reactor design was achieved previously and single biomass

combustion experiments were conducted (Flower & Gibbins, 2009). In that study, wire meshes were configured in vertical arrangement and a sample holder with a K type thermocouple was placed in middle of them. The particle was heated by radiation originated from the hot wire meshes. Temperature measurement of the fuel particles could not be achieved since the particle size was too small for thermocouple conduction. The only purpose of the thermocouples was to make sure the heat flux from the meshes was consistent between each trial so that particle to particle comparison could have been made. Combustion parameters like ignition delay and total combustion duration were obtained from image processing techniques that were applied on the data from high speed camera operating in visual band.

Recent applications of wire mesh reactors include single particle combustion used as a sub-model (Mason, Darvell, Jones, Pourkashanian, & Williams, 2015) to predict and model the combustion behavior of pulverized biomass in large scaled furnaces. The data obtained from single particle combustion (e.g. kinetic parameters for pyrolysis, char combustion and ignition delay time) are used to develop combustion models for furnaces (Yang et al., 2008).

In the most recent studies (Riaza, Ajmi, Gibbins, & Chalmers, 2017; Riaza, Gibbins, et al., 2017), single particles of coal and biomass were burned in a novel wire mesh reactor to observe ignition and combustion with high speed cinematography. The wire meshes were set up in vertical configuration with an optical window on the top to allow optical access. Distinct stages of volatile and char combustion were detected by image processing from visual band high speed camera data. An impact of particle mass on ignition and combustion behavior was observed for both coal and biomass particles. Especially coal particles show higher dependency on particle mass for combustion durations.

2.4. Infrared Technology

Molecules of all matters in solid, liquid or gas phases are in ongoing thermal excitation except at the temperature of absolute zero (-273.15 °C). An increase in the temperature of matter also causes an increase in thermal excitation (Colthup, Daly, & Wiberley, 1965). Because of the fact that atoms in molecules have electrical charges, their oscillating centers of electrical charge emit electromagnetic radiation. In a body, molecules have different levels of thermal excitation that causes electromagnetic radiation in different wavelengths.

A hot body which is seen as white in visual band, emits a great amount of energy in infrared region and also visual region of the electromagnetic spectrum (see Figure 2.4). As it gets cooler, red color which represents the longer wavelength of visual band is seen. When the body is cooled further, it cannot emit radiation in visual band wavelengths as the emission shifts to infrared wavelengths that cannot be sensed by human perception. This observation is based on the fact that diminution in temperature, hence in thermal radiation, shifts the energy peak to longer wavelengths (Robinson & Moeller, 1974).

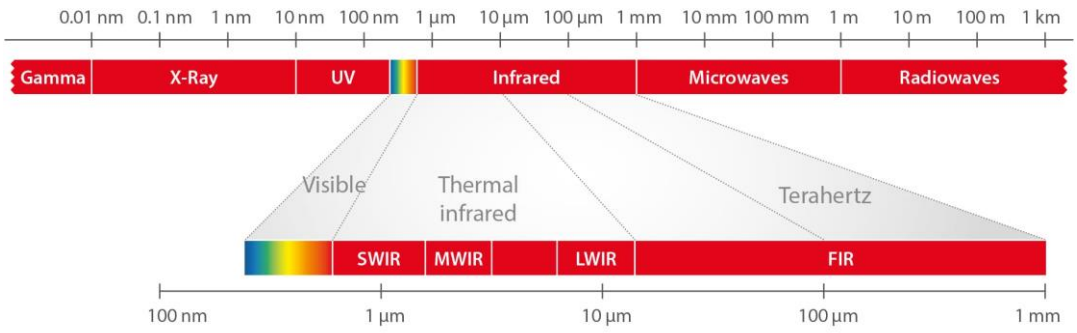

Figure 2.4. The Electromagnetic Spectrum (InfraTec, 2019)

The theoretical concept of blackbody was first introduced by Robert Kirchhoff in 1860 and the correct mathematical description of the radiation emitted by a blackbody was given by Max Planck in 1900 (Stewart & Johnson, 2016). A blackbody theoretically absorbs the whole amount of incident radiation and it is considered as the ideal heat radiator. Consequently, it has the theoretical maximum absorption and emission values of 1. The spectral energy distribution of a blackbody radiator was derived by Planck's radiation law,

$$E_\lambda = \frac{2hc^2}{\lambda^5} \times \frac{1}{e^{\left(\frac{hc}{kT\lambda}\right)} - 1}$$

where E_λ is the energy radiated per unit volume by a blackbody cavity in the wavelength λ, h is Planck's constant, c is the speed of light, k is the Boltzmann constant and T is the absolute temperature. For illustrative purposes, the spectral radiance of a blackbody at 800 Kelvin temperature over wavelength is shown in Figure 2.5. The wavelength for which the body emits maximum spectral radiance was described by Wien's displacement law (Modest, 2013),

$$\lambda_{max} = \frac{b}{T}$$

where λ_{max} is the wavelength of peak spectral radiance and $b \approx 2898\ \mu mK$.

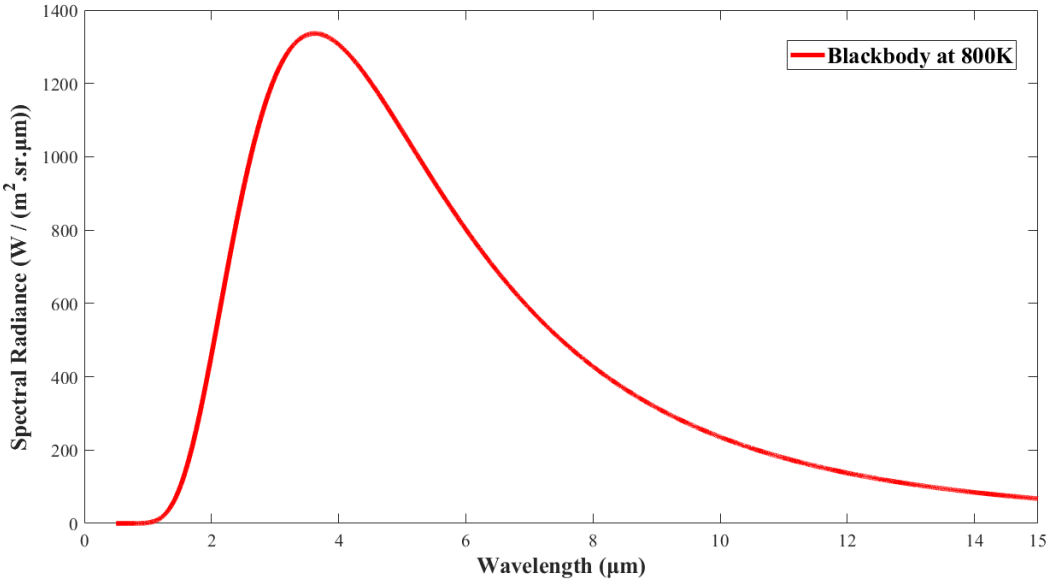

Figure 2.5. Planck's Blackbody Radiation Curve

According to Wien's law; by an increase in temperature, the maximum radiation will be displaced to shorter wavelengths as shown in Figure 2.6. For instance, a blackbody radiator with a temperature of 300 K, has the maximum radiation at 9.66 µm wavelength in the long-wave infrared range; and when its temperature is increased to 800 K, the maximum radiation will shift to 3.6 µm in the mid-wave infrared range.

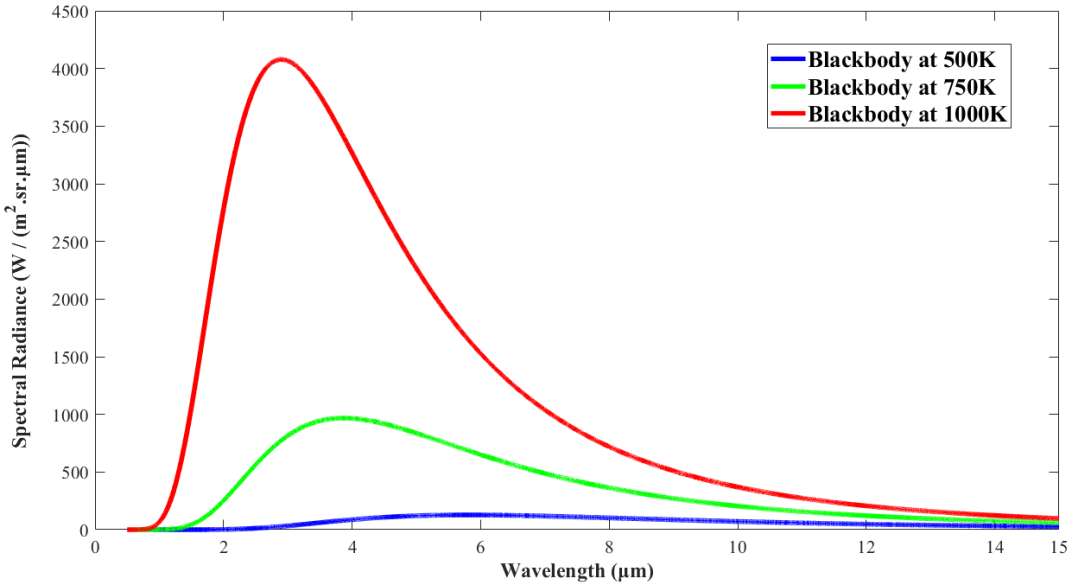

Figure 2.6. Wien's Law and Spectral Radiation

Natural and artificial radiators behave either like gray bodies or selective radiators. Spectral emissivity is defined as the ratio of a body's radiation at a certain wavelength to a blackbody's radiation at the same temperature and it also depends, to a lower extent, on the pressure (Modest, 2013). The emissivity value of a gray body is independent of the wavelength, consequently the spectral radiance at a certain temperature is equal to a constant fraction of a blackbody radiator at that temperature (Modest, 2013). Most of the natural radiators behave as selective radiators and have a characteristic spectral emissivity distribution because of their unique self-excitations. In Figure 2.7, the spectral emissivity of a gray body radiator with and a selective radiator body radiation intensities are shown.

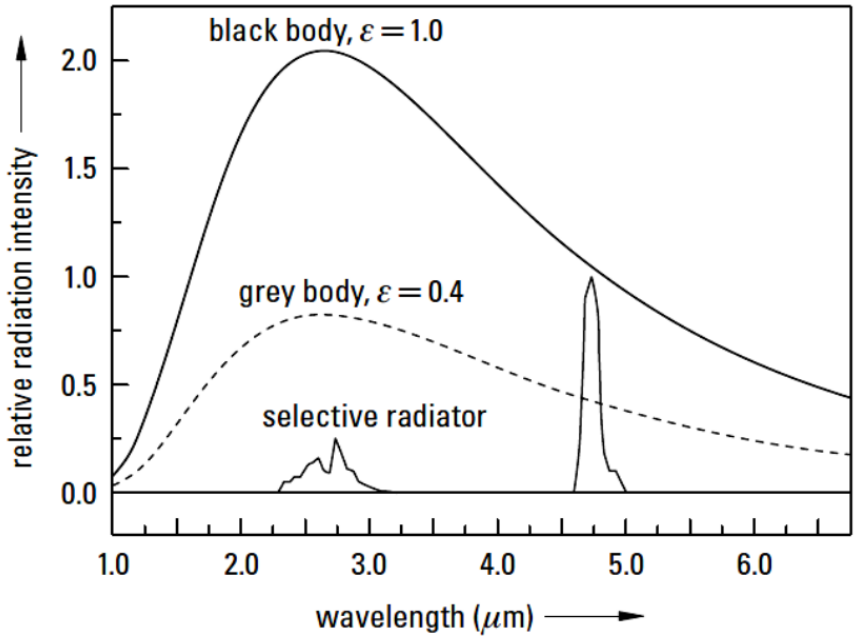

Figure 2.7. Gray Body Radiator and Selective Radiator (Elsaidy, Kassem, Tantawy, & Elbasuney, 2018)

The absorption and scattering due to the gas molecules in the atmosphere, results in weakened electromagnetic radiation emitted by the radiator because the path length increases. Thus, the range of an infrared sensing system is adversely affected by the increment in the path between radiator and sensor. Radiation attenuation in the atmosphere is mainly caused by absorption and scattering. The absorption is caused by excitation of gas molecules, especially H_2O, CO_2 and CO (Leckner, 1972). Molecules of CO_2 and H_2O have strong absorption bands where the radiation is almost absorbed in a very short distance. These strong absorption bands define the atmospheric windows which are the wavelength ranges where the atmosphere is transparent. In Figure 2.8, atmospheric windows at ground level are shown. Wavelength intervals which allow infrared radiation transmittance are named as short-wave infrared (SWIR), mid-wave infrared (MWIR) and long-wave infrared (LWIR). Because of the transmittance characteristics, infrared detectors are also designed to operate in these atmospheric window bands.

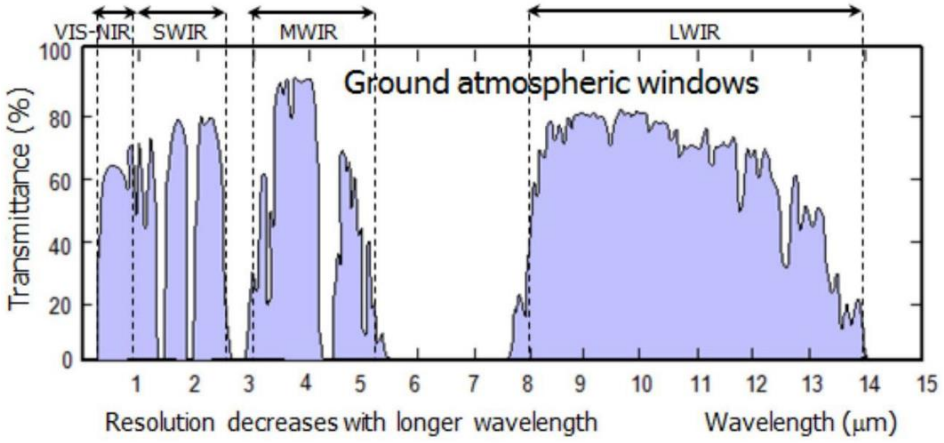

Figure 2.8. Spectral Transmission of Atmosphere (Dhar, Dat, & Sood, 2013)

In order to sense infrared thermal radiation, detectors which are sensitive to photons in infrared region have to be utilized. Many different detector technologies (see Table 2.2) such as thermal photodetectors, quantum detectors, photoelectric and photoconductive receivers have been developed in the last decade (P. Capper & Elliott, 2001). In thermal photodetectors like the most common type bolometers, built-in thermistors change their electric resistance according to the amount of heat absorbed from incident infrared radiation; hence a digital is generated from the electrical signal (Richards, 2013). On the other hand, in quantum detectors, the incident infrared radiation either frees electrons from the detector material or releases charge carriers in the detector material. As a result, the number of charge carriers changes the resistance of the detector and generates digital signal eventually (P. Capper & Elliott, 2001).

Table 2.2. *Types of Semiconductor Photon Detector* (P. Capper & Elliott, 2001)

Type	*Examples*
Photoconductive-extrinsic	Ge:Hg, Si:Ga
Photoconductive-intrinsic	PbS, HgCdTe
Free-carrier Photoconductor	InSb
Homojunction Diodes	InSb, HgCdTe
Photon Drag Detectors	Ge
Photoemissive	GaAs-CsO

In quantum detector, in order to be able to differentiate the incident infrared radiation from the detector's own noise, it has to be cooled down to increase detectivity. Otherwise, the detector will not be able to distinguish the digital signal whether it originates from its own thermal radiation or from the target radiator. To measure radiation from objects in different wavelengths, a detector type that works at the specific wavelength is utilized. In Figure 2.9, different detector materials and their detectivity in spectrum is shown.

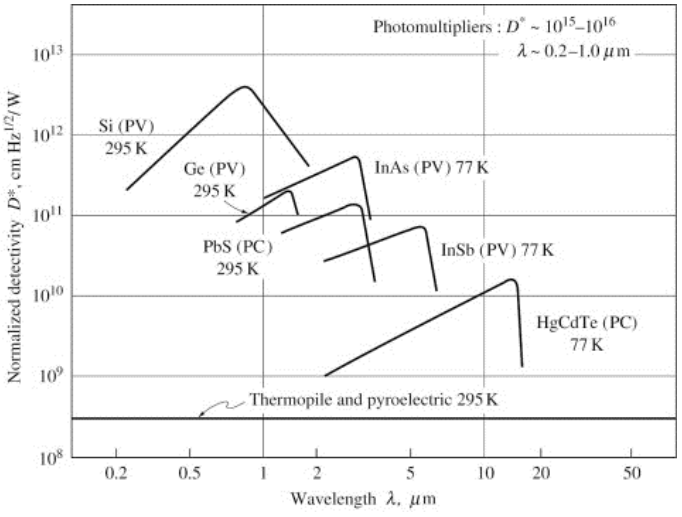

Figure 2.9. Detectivity of Infrared Sensor Materials (Modest, 2013)

2.5. Infrared Measurement Studies

The combustion of a solid fuel particle results in a rapid increase in its temperature due to the exothermic nature of the reaction, and subsequently it radiates infrared radiation. This radiation can be sensed digitally by infrared cameras that are equipped with infrared detectors with multiple pixels aligned as a focal plane array (FPA). These infrared sensing systems enable to measure radiometric signals and allow researchers to observe combustion process and its stages.

In a recent study (Soldani, 2015), an infrared measurement methodology is outlined in detail for a 14 bit infrared camera system. As the pixel in the detector of the camera can hold 14 bits of data, there are 2^{14} different values that can be interpreted by the detector and those different values are called as digital levels (DL). Digital values have to be mapped with radiance values to give meaningful results in terms of the problem physics. This mapping process is called radiometric calibration. The calibration process is done by using a controllable blackbody source. The detector material governs the camera responsiveness, though the responsiveness can be considered as linear in the wavelength interval of the camera. As the blackbody source's temperature changes, digital level values generated in the camera output change linearly with the radiance emitted. Definition of a calibration for an infrared camera is mathematically determining the linear relation between radiance and digital level by calculating the linear coefficients. In order to define a linear relation, at least two measurement data are required. A well performed calibration is done with more than two points and it results in a better confidence interval of linear coefficients.

In the literature, single particle combustion of a solid fuel was previously observed with three-color optical pyrometry (Khatami & Levendis, 2011). The temperature-time history of single particle coal combustion was recorded with an optical pyrometer which operates in three different wavelengths around near infrared region, 0.640 μm, 0.810 μm and 0.998 μm. Two-point calibration was implemented by utilizing a tungsten lamp and a high temperature blackbody cavity. Emissivity of the coal was

assumed as gray body, three different radiance readings were measured from three different wavelengths, and those three points were fit into Planck's radiation curve. The temperature that gave the calculated Planck curve was the measured value from combustion at a certain instant.

More recently single particle ignition and combustion of anthracite, semi-anthracite and bituminous coals under oxy-fuel conditions was investigated with near infrared pyrometry (Riaza et al., 2014b). Deduced ignition temperatures were found to increase as the rank increases and to decrease with the increase in oxygen concentration. Radiance histories of burning particles in infrared were analyzed, ignition modes (i.e. homogenous or heterogenous ignition) were deduced, and burnout times were reported.

Combustion of single biomass particles was also investigated with near infrared pyrometers and high speed cameras in visual band (Levendis et al., 2011; Riaza et al., 2014a). Temperature-time histories of the particles were deduced and parameters like, ignition temperature, ignition delay, maximum char temperatures, burning time of volatiles and char were calculated from the pyrometric signals. Discrepancies between pyrometric and cinematographic visual band data were detected and the duration of volatile combustion could not be assessed reliably because of the physical limitation of observing only in the near infrared region (Riaza et al., 2014a). Moreover, it was reported that for the flame temperature deduction, gray body emissivity was an invalid assumption.

In this research, an infrared sensing system composed of mid-wave and long-wave FPA detectors was used with a wire mesh reactor to investigate the combustion of single biomass particles. The experimental setup and methodology are novel to the investigation of single particle combustion of Turkish olive residue. Relevant parameters such as the ignition delay times and combustion phases' durations of olive residue were studied in this work. Additionally, Tunçbilek lignite single particle combustion experiments were conducted in order to compare with olive residue.

2.6. Motivation and Objective

The motivation in this study is to utilize broadband imaging infrared cameras which are considered as superior to single pixeled pyrometer devices, in single particle combustion experiments and explore the problem physics by temporal and spatial analyses with a novel method.

The objective of this thesis is to characterize olive residue from Balıkesir, Turkey by coupling infrared measurement technics to a single particle wire mesh reactor. The wire mesh setup that was used in this study was configured to a fixed current to provide a high heating rate (~800 °C/s) and temperature (~1100 °C) close to the conditions in actual power plants. A novel approach implemented in this research consists of using an infrared remote sensing system with two broadband imaging infrared cameras in mid-wave (3-5 μm) and long-wave (8-12 μm) infrared to investigate the single particle combustion. The infrared sensing system gathers radiance data over time by capturing images from the wire mesh reactor in both horizontal and vertical configuration. On the one hand, infrared measurement of horizontally configured wire mesh reactor where the single layer of fuel is used, validates the setup as suitable for combustion trials while providing some useful information about mesh repeatability. On the other hand, vertical configuration of the wire mesh reactor is set up to conduct single particle combustion experiments of olive residue and characterize the fuel in terms of its ignition delay time, volatile, char and total combustion time, which show relevance of co-firing of biomass and coal.

CHAPTER 3

MATERIALS AND EXPERIMENTAL METHODS

The fuels and the experimental equipment used in this study are described herein. The details of the wire mesh reactor and the infrared camera system are stated. In addition, the methods used to analyze and post-process the recorded data are elaborated. The problem physics behind radiometric infrared cameras and how they generate meaningful data is also explained. Experimental conditions are given explicitly and the scientific methodology to obtain desired parameters is stated.

3.1. Fuel Selection and Preparation

In this study, one biomass and one coal were used to investigate combustion. Those fuels were; olive residue (OR) which originates from Balıkesir, Turkey and Tunçbilek lignite (TL) of Kütahya, Turkey. The latter fuel was used for comparison purposes only. All fuels were fully characterized. Specifically, proximate and ultimate analysis, inorganic species content and high heating values were previously obtained and reported (Magalhães, Panahi, Kazanç, & Levendis, 2019; Magalhães, Riaza, & Kazanç, 2019) and are shown in Table *3.1*. In brief, the proximate analysis was obtained using a Perkin Elmer 4000 thermogravimetric analyzer, following the procedure described in previous work (Rubio, Mayoral, Izquierdo, & Andre, 2001). The ultimate analysis was undertaken according to the standard D5373-16, and the ash compositions were obtained with an X-Ray Fluorescence analyzer, according to standard TS EN 15309. The high heating values of the biomass and coal samples were computed according to the correlations presented by other studies (Friedl, Padouvas, Rotter, & Varmuza, 2005; Majumder, Jain, Banerjee, & Barnwal, 2008), respectively for biomass and coal.

The fuels were received raw as chunks and had to be processed before utilization in the wire mesh reactor. Both OR and TL were ground in the Mineral Processing Laboratory, Middle East Technical University. Raw samples were crushed to obtain single particles that weighed between 4.9-17.6 mg for OR, and approximately 3 mg for TL, which is used for comparison purposes. It has been reported that (Riaza, Gibbins, et al., 2017) aspect ratio of the single particles between 5 and 30 mg does not considerably affect the results. Additionally, both fuels were crushed to be gathered in a finer particle size to which followed sieving in the Clean Combustion Technologies Laboratory, Department of Mechanical Engineering at Middle East Technical University. Sieving was done with ASTM (American Society for Testing and Materials) sieves until a particle size of 106-125 μm was reached. The final processed form of the fuels is shown below in Figure 3.1.

Figure 3.1. Processed Fuel Samples of Olive Residue and Tunçbilek Lignite with size range 106-125 μm for Horizontal Mesh Configuration

Table 3.1. *Elemental Analysis and Energy Content of Olive Residue and Tunçbilek Lignite* (Magalhães, Panahi, et al., 2019; Magalhães, Riaza, et al., 2019)

Parameter	*Olive Residue (OR)*	*Tunçbilek Lignite (TL)*
Proximate Analysis, wt.% as received		
Moisture	5.9	2.81
Volatiles	71.9	31.1
Fixed Carbon[a]	17.4	52.1
Ash	4.8	14.0
Ultimate Analysis, wt.% dry basis		
C	46.6	61.8
H	6.40	5.60
N	0.58	2.65
S	-	1.45
O[a]	46.4	28.5
Inorganic Species, wt.% dry basis		
Si	4.60	33.3
Al	1.76	12.9
Fe	7.95	22.3
Ca	26.4	1.91
Mg	1.23	1.73
Na	-	-
K	48.6	3.16
P	1.98	0.12
Cl	4.46	2.87
S	2.37	19.1
High Heating Value (MJ kg^{-1}, dry basis)	18.6	27.8

[a]by difference

Prior to the combustion experiments, all processed fuel samples were dried in a muffle furnace to eliminate the effect of moisture on combustion. Especially the ignition delay time parameter in combustion is heavily influenced by the amount of moisture in fuel as stated by previous researchers (Mason et al., 2015). In the Clean Combustion Technologies Laboratory at Middle East Technical University, a Protherm PC442 branded muffle furnace which can be seen from Figure 3.2 was set to 105 ℃ and the samples were placed in open crucibles to dry. The samples were dried overnight before the experimentation process.

Figure 3.2. Protherm PC442 Muffle Furnace

Following the drying process, single particles were carefully selected and weighed in a Mettler Toledo TLE 104 model analytical balance, as shown in Figure 3.3, which has a measurement precision of 0.1 mg. Each particle was separated and labeled according to their mass. Single layer olive residue (OR) fuel was also weighed with the same balance and a single layer of particles dispersed unto the wire mesh was

ensured, which corresponded to approximately 50 mg. Figure 3.4 shows that the single particle samples were classified according to their measured mass values.

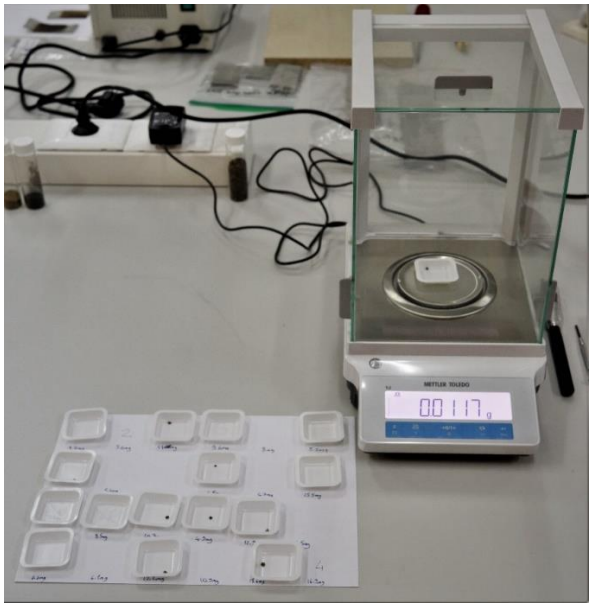

Figure 3.3. Mettler Toledo TLE104 Balance with Single Particle Samples

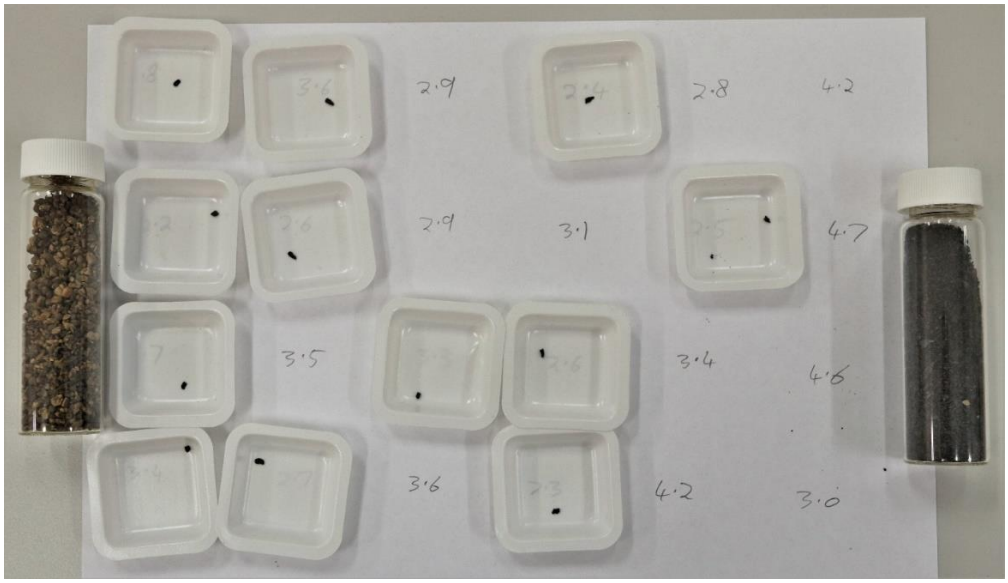

Figure 3.4. Samples of Single Particle Fuels with Particle Masses between 3 and 17.6 mg

3.2. Experimental Setup

The technical specifications and functional properties of the wire mesh reactor (WMR) and the infrared sensing system are described in this subsection. The wire mesh reactor consists of a wire mesh couple through which controllable current flow. This current is supplied by a DC (direct current) supplier and monitored by data acquisition system. The wire mesh reactor is coupled with an infrared sensing system consists of one mid-wave infrared (MWIR) and one long-wave infrared (LWIR) camera and allows the real time measurement of the temperature over time by remotely recording the radiometric signal originated from the combustion of the sample.

3.2.1. Wire Mesh Reactor

The main device used in this study is the wire mesh reactor (WMR) that can be found in the Clean Combustion Technologies Laboratory, Department of Mechanical Engineering at Middle East Technical University. This reactor's working principle is the heating of a stainless-steel (SS-316) mesh couple through Joule effect using electrodes connected to a DC supplier. An overview of the setup is shown in Figure 3.5. Depending on the experimental requirements, the mesh couple can be easily configured in either horizontal or vertical position with respect to the ground, as it can be seen from Figure 3.6 and Figure 3.7 respectively.

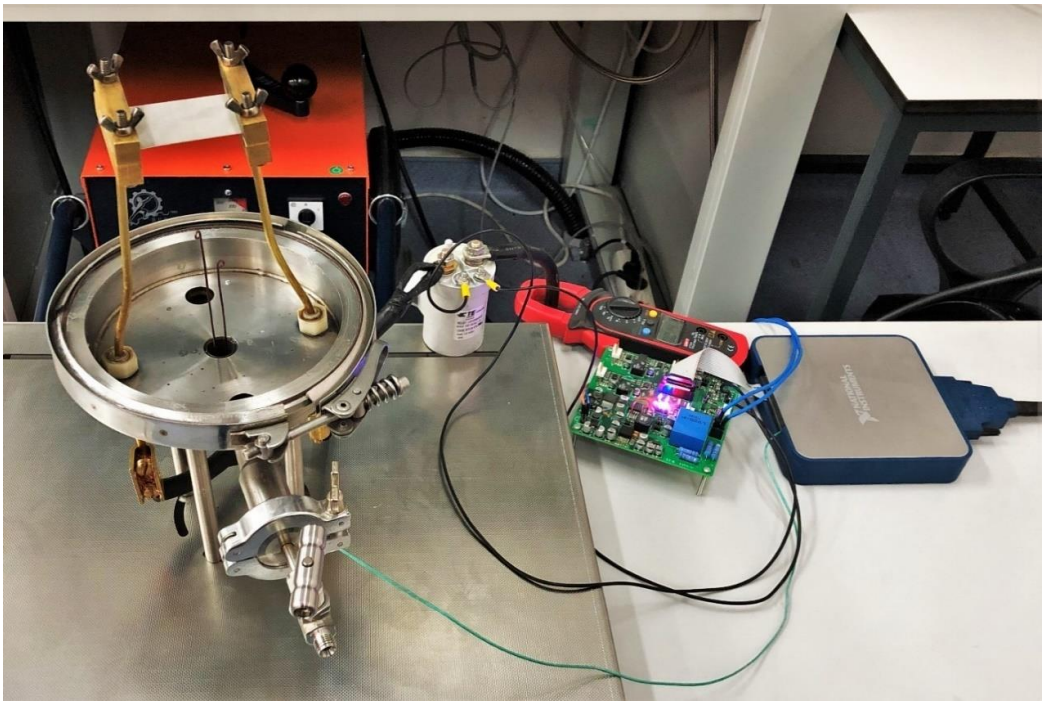

Figure 3.5. Wire Mesh Reactor (left-hand side) with DC Source and Control System (right-hand side)

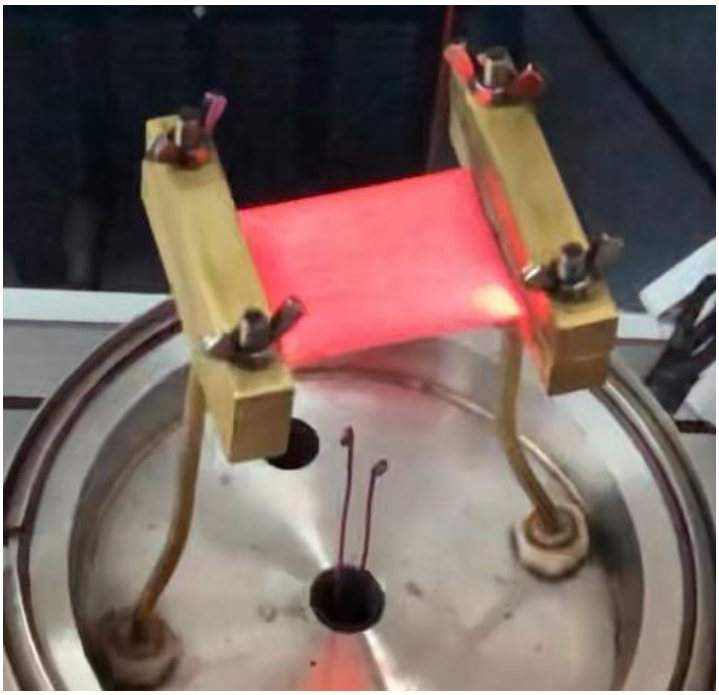

Figure 3.6. Horizontal Configuration of Wire Mesh Reactor during Heating Process

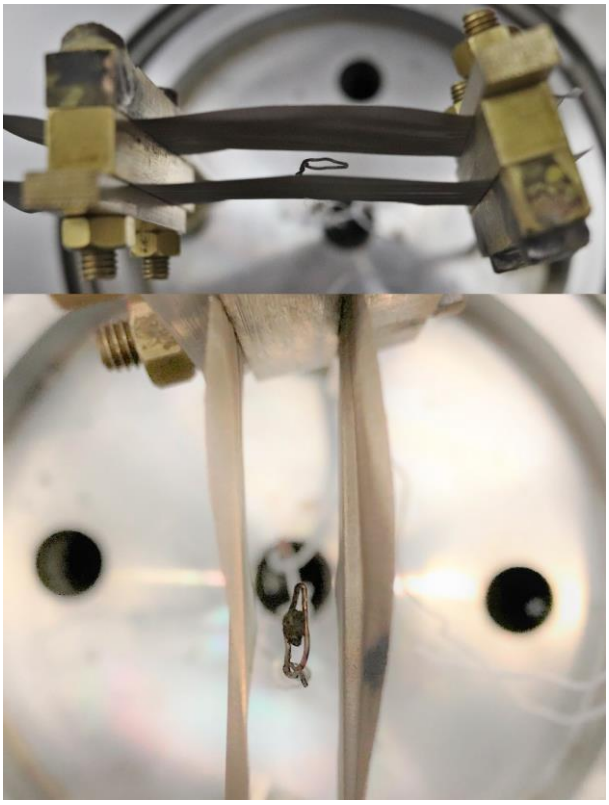

Figure 3.7. Vertical Wire Mesh without Sample (Top) and with OR Particle (Bottom)

The wire mesh couple used in this study is made of stainless-steel (SS-316) that is manufactured with a wire diameter of 25 μm and cut into 75 mm by 40 mm to comply with the physical design of the reactor and the required test conditions.

Ensuring the mesh temperature stability during the combustion trials is crucial, as that factor heavily influences ignition delay and burnout times. In both configurations (i.e. vertical and horizontal), a thermocouple was welded to the mesh and its output was monitored using a data acquisition system and a PC. On the same PC where the data acquisition system is established with LabVIEW software, the amount of current that flows through the wire mesh is also adjusted. The thermocouple used in this study was of R-type with a composition of 100% Platinum for the positive side and %13 Rhodium, 87% Platinum for the negative side. For both configurations of mesh, the thermocouple was welded onto the center of the mesh in a three-point weld. This was

achieved with HL-WD branded orthodontic spot welder in Figure 3.8 which can weld wires with diameter below 1 mm. Thus, the mesh temperature during the combustion experiments was measured from the center of the mesh as shown in Figure 3.9.

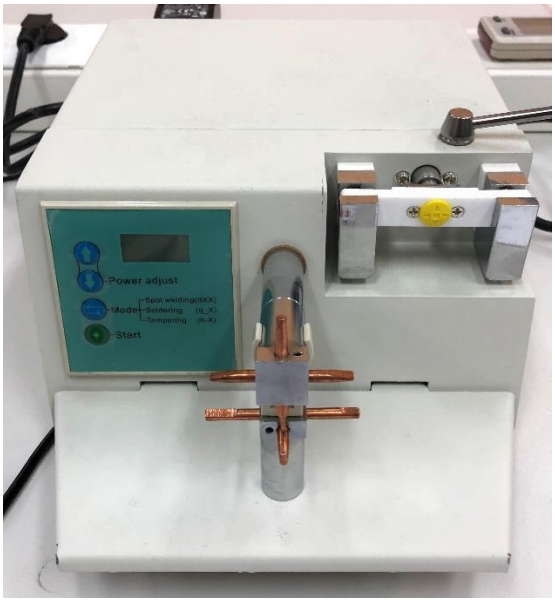

Figure 3.8. HL-WD Model Orthodontic Spot Welder

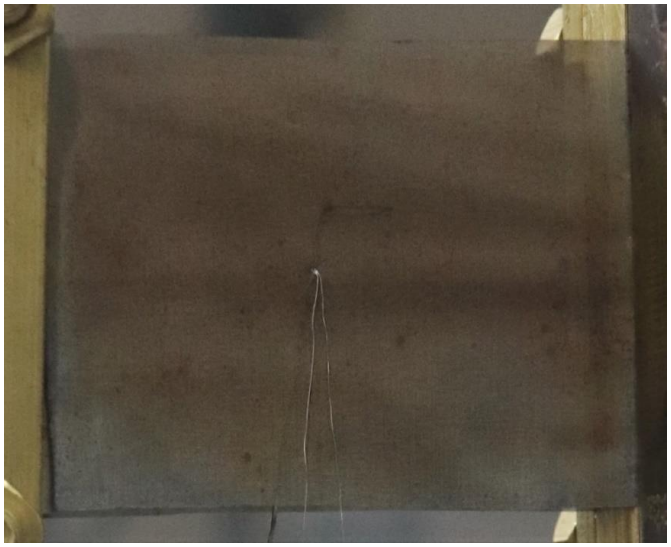

Figure 3.9. A Welded Thermocouple on Vertical Mesh

3.2.2. Infrared Camera System

In previous researches, near infrared pyrometers which are basically a single pixel detectors were used in investigation of single particle combustion (Bejarano & Levendis, 2008; Riaza et al., 2014b, 2014a). As it is governed by Wien's displacement law, majority of the thermal radiation originating from combustion occurs in wavelengths longer that near infrared, additionally observing the whole setup with a single pixel radiance value yields a large margin of error since the region of interest, the particle, cannot be distinguished from the rest of the furnace (Khatami & Levendis, 2011). In this study, FPA detector equipped cameras in which the region of interest, like the particle, can be selected and sense longer wavelengths of thermal radiation are used to investigate single particle combustion.

In the thermal sensing part of the setup, two different thermal cameras were used to observe the combustion of single particles and investigate the mesh. These cameras operate in infrared band of the electromagnetic spectrum and generate certain number of images that can be used to measure radiance from the objects in the field of view. The thermal sensing system consists of a mid-wave infrared (MWIR) and a long-wave infrared (LWIR) camera. The region between 3-5 μm and 8-12 μm is widely accepted as mid-wave and long-wave infrared, respectively. Due to the fact that these intervals enable infrared (IR) measurement in the atmospheric window, these parts of the electromagnetic spectrum are crucial. Hence the measurement in this study is carried out in both of those bands.

Figure 3.10. Long-wave (left-hand side) and Mid-wave (right-hand side) Infrared Cameras

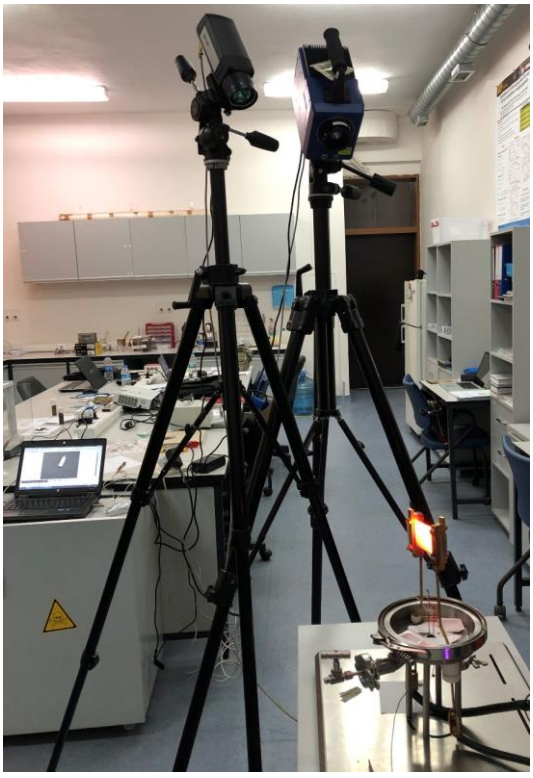

Figure 3.11. Infrared Camera System with Wire Mesh Reactor

The cameras were placed above the wire mesh reactor to observe combustion process without any optical blockage from the system components. The whole system is exposed to atmosphere without any enclosing on them, as it is shown in Figure 3.11, because any kind of enclosing material's radiative transmissivity would cause loss in the amount of radiance which is collected by the sensors. The minimum distance between the camera lenses and the setup was dictated by the minimum focal distance capability of the lenses. To make sure that the generated images were in focus, the distance between the lenses and wire mesh reactor (WMR) was adjusted as 1.2 meters. From the data gathered from the infrared cameras, it is possible to determine radiance and temperature in both infrared bands.

3.2.2.1. Mid-wave Infrared (MWIR) Thermal Camera

The mid-wave infrared sensitive camera used in this study is FLIR branded and SC7200 model. It has an image sensor that can sense emissions between 1.5-5.1 µm wavelengths, although the atmospheric window in mid-wave IR (MWIR) is between 3-5 µm wavelengths. In order to measure the setup correctly, the camera is equipped with a high pass 2.9 µm filter so that the sensor only gathers photons emitted between 2.9-5.1 µm wavelengths and enabling the measurement in the atmospheric window. This type of infrared camera image sensor is InSb made. Resultantly, in order to operate the sensor, it needs to be cooled down to 77 K cryogenically with a built-in Sterling cooler.

FLIR, the manufacturer company, had provided, a calibration file which was created with a blackbody source and valid between 200-1100 ℃. There is a certain amount of time during which camera collects photons that hit the sensor. This period is called as integration time (IT). Due to the electrical capabilities, the camera cannot cover the whole range of temperature sensitivity in a single integration time. SC7200 can operate in two different integration times simultaneously, hence the total amount of frames generated per measurement are split into half for each integration time.

Table 3.2. *FLIR SC7200 Mid-wave Infrared Camera Specifications*

FLIR SC7200	
Imaging Performance	
Detector Type	Mid-wave InSb
Spectral Range	1.5 – 5.1 µm
Resolution	320 x 256
Frame Rate	170 Hz
Detector Pitch	30 µm
NETD[a]	< 20 mK
Measurement	
Temperature Range	5 ℃ up to 3000 ℃
Accuracy	+/- 1% or +/- 1℃
Optics	
Camera Aperture	f/3.0
Lens Focal Length	50 mm
[a]Noise Equivalent Temperature Difference	

3.2.2.2. Long-wave Infrared (LWIR) Thermal Camera

A FLIR branded A655 model long-wave infrared sensitive camera was used in measurements in this study. In contrast with the mid-wave infrared (MWIR) camera sensor, for a long-wave infrared sensitive sensor, micro-bolometer, a cooling system is not required. This camera can sense photons emitted between 7.5-14 µm wavelengths but in order to make it more suitable for the atmospheric transmission conditions, it is equipped with a lens that only permits transmittance between 8-12 µm wavelengths. The calibration file which is provided by the manufacturer is generated with a blackbody source and validated between 200-2000 ℃. Unlike InSb made sensor equipped infrared cameras, micro-bolometers are sensitive can sense the given

temperature range with a single integration time. As a result of it, the maximum number of frames that can be generated by the camera represents the number of frames per second of each measurement.

Table 3.3. *FLIR A655 Long-wave Infrared Camera Specifications*

FLIR A655	
Imaging Performance	
Detector Type	Long-wave µbolometer
Spectral Range	7.5 – 14.0 µm
Resolution	640 x 240
Frame Rate	100 Hz
Detector Pitch	17 µm
NETD[a]	< 30 mK
Measurement	
Temperature Range	-40 ℃ up to 2000 ℃
Accuracy	+/- 2 ℃ or +/- 2%
Optics	
Camera Aperture	f/1.0
Lens Focal Length	41.3 mm
[a]Noise Equivalent Temperature Difference	

3.3. Experimental Methods

The methods applied and the radiometric signal data that are sensed by infrared camera setup analysis conducted are stated herein. The test conditions of the wire mesh reactor and its mesh configuration are explained in this section. Radiometric signal data acquisition from the camera setup for each combustion trial is also elaborated.

3.3.1. Combustion Test Conditions

The test conditions were defined by adjustment of the current directly on the DC supplier. A certain value of current (ampere – A) would result in a heating rate, during the transient period, and a plateau temperature, reached after the transient period. As the temperature of the mesh couple increases, they start to radiate heat and ignite the fuel sample, marking the beginning of the combustion. The heating rate applied was $\sim 10^3$ ºC s^{-1}, a plateau temperature of 1100 ºC, and atmospheric air and pressure. Since the amount of time required to reach the operating temperature was much shorter than the combustion durations, in the analysis part of the data the experiment started with the instant when wire meshes had reached the operating temperature.

The aforementioned test conditions were set, and two distinct configurations of the wire mesh reactor were defined, each serving a specific purpose. On the one hand, to perform single particle combustion experiments, the mesh configuration was adjusted to vertical position so that the particle could be observed on top without the mesh interference. On the other hand, to observe mesh temperature uniformity and the combustion of a single layer of particles, the horizontal configuration was preferred. A mesh couple, with fuel in between, is placed parallel to the ground in horizontal configuration, as shown in Figure 3.6. The clamps that conduct the electricity to the mesh, have to be changed in order to switch the wire mesh reactor's configuration. In vertical configuration, Figure 3.7, the mesh couple is placed perpendicular to the ground and there must be a certain distance between them to insert the single particle fuel on the sample holder.

To ensure that heat transfer took place preponderantly by radiation, the individual fuel particles were placed in a thin support not in contact with the mesh surfaces as shown in Figure 3.7. It should be noted that during the volatile combustion stage, some of the fuel samples fell from the support and outside of the monitoring area because of the rapid gas release and pressure change in the sample and were excluded from the analysis thenceforth.

3.3.2. Radiometric Signal Acquisition

Previous studies were conducted to determine the burnout times of single particles of coal and biomass in visual band (Riaza, Gibbins, et al., 2017; Shan et al., 2018). In these studies, luminosity values from high speed cameras with visual band detectors were gathered as RGB values and converted to grayscale as the radiometric signal. On the contrary, in this work, infrared cameras with photon detectors were able to sense the actual radiometric signals which cannot be sensed in visual band.

Due to the nature of combustion, temperature changes over time at a various rate. Electromagnetic radiation in infrared band is detected by the remote sensing system and saved as raw data. In the infrared thermal sensing system used herein, two cameras record the radiometric signal in different PCs with different software. For the MWIR camera FLIR SC7200 data were recorded with Altair by FLIR Systems version 5.91.010. On the other hand, for the LWIR camera, FLIR A655, data were recorded with a newer compatible software, ResearchIR 4 by FLIR. In Figure 3.12, the radiometric signal recording interface of ResearchIR software during a combustion trial is shown.

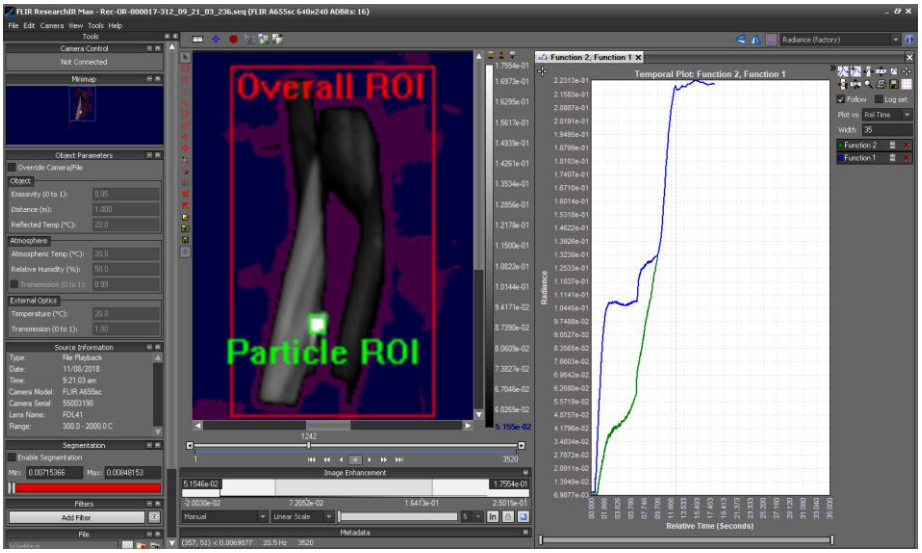

Figure 3.12. ResearchIR Software with Radiometric Signal Recording Interface

The data recording software records the radiance received for each pixel in the focal-plane array (FPA) over time so that the raw infrared data are generated. The region of interest where the combustion occurs needs to be selected in order to process the area of interest in the field of view of the cameras. In the vertical mesh configuration, the region of interest was selected as the single particle itself (see Figure 3.13), since there were other thermal radiation and reflection sources like wire meshes, clamps of the setup, etc. For the horizontal mesh configuration part, as the fuel was distributed between the two meshes as a single layer of particles, and to observe combustion and temperature distribution, the region of interest was selected as the whole mesh area, as shown in Figure 3.14.

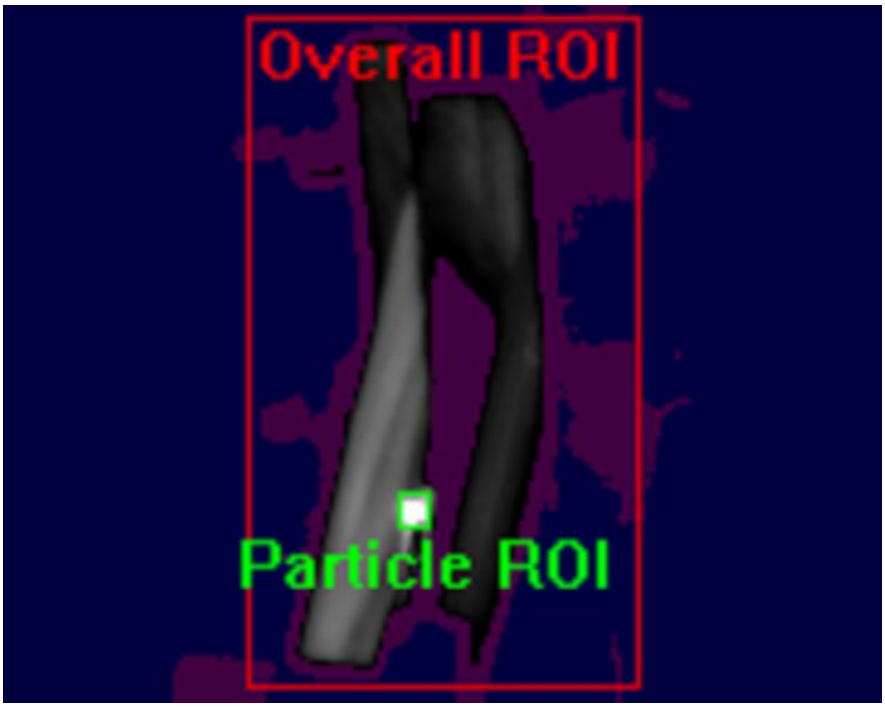

Figure 3.13. Vertical Mesh Configuration Region of Interest

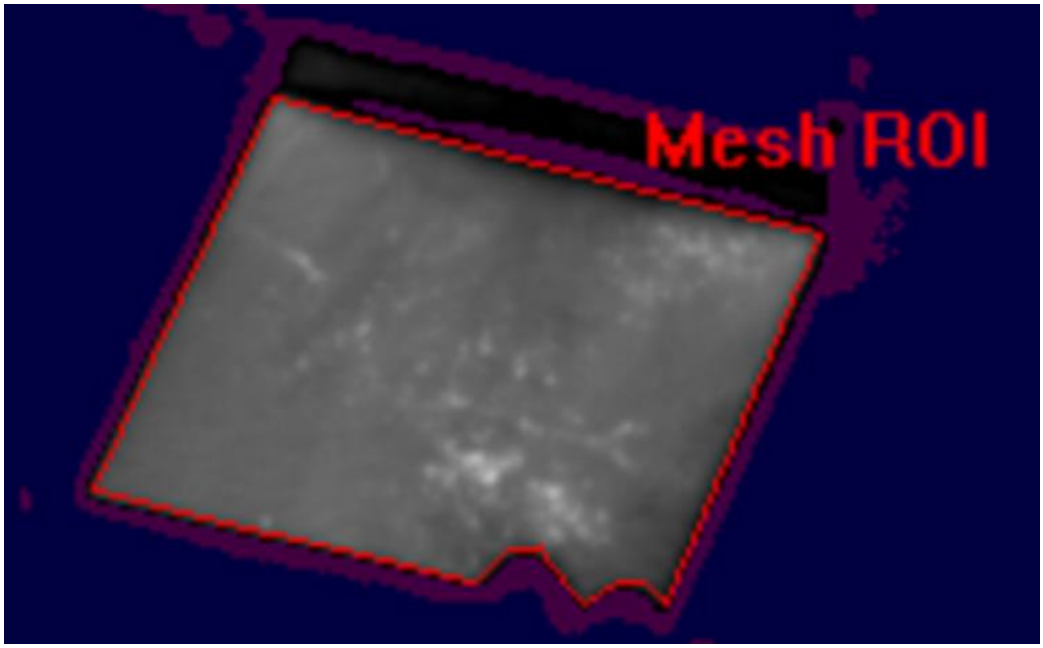

Figure 3.14. Horizontal Mesh Configuration Region of Interest

Each camera operates with a different frame rate hence each has a different time step for the data that being generated. The created region of interest is valid for every frame of camera record during the experiment and only the data in this region was evaluated for processing. Among the many pixels in the region of interest, the pixel which has the maximum radiance value in each frame was plotted against time, and the combustion trial's radiometric signal curve was generated.

An extra region of interest which covers the entire setup was also created to observe the wire mesh reactor's temperature change, detect the instant when it reaches the steady operating temperature which is used in analysis part for determination of ignition delay values, and record the jump in radiance level due to appearance of the volatile flame.

3.4. Parameters and Analysis

Temporal parameters that show fuel characteristics like ignition delay times and combustion durations were obtained by processing the raw infrared data recorded in each experiment. Radiance data collected from both of the cameras, MWIR and LWIR, were analyzed in MATLAB R2018b software to achieve the desired parameters. Analyzes were conducted by investigating the radiometric combustion curve regarding the expected events in biomass combustion. As aforementioned in literature review section, olive residue, a biomass, combusts in two phases, volatile and char combustion. On the contrary, Tunçbilek coal combustion occurs in a single phase. Based on these assumptions, the relevant parameters were calculated in each experiment and the observed results corroborated this assumption.

3.4.1. In-Band Temperature Calculation

Natively, infrared cameras detect the thermal radiation which is collected by their focal plane array image sensors. Due to the fact that the cameras were calibrated by an infrared blackbody source, the temperature value derived from their radiance output will necessarily be an in-band temperature. By definition, in-band temperature or relative blackbody temperature corresponds to the assumption that the measured matter emits energy like a blackbody in the given electromagnetic band interval. Real radiators cannot emit as much as a blackbody, so the emissivity value has to be smaller than 1 in real conditions. Consequently, the calculated in-band temperature value is lower than the real temperature value as it is governed by Planck's radiation law.

Radiance data in the analysis part and in the rest of the work have been converted to in-band temperature values by using the bisection numerical method.

In order to be able to utilize bisection method, spectral radiance of a blackbody between certain wavelengths have to be calculated and it is governed by Planck's law as below,

$$\int_{\lambda_1}^{\lambda_2} \frac{2c^2h}{\lambda^5} \times \frac{1}{e^{\left(\frac{hc}{kT\lambda}\right)} - 1} d\lambda$$

where λ_1 and λ_2 respectively indicates the shorter and longer wavelength of the band, h is Planck's constant, c is the speed of light, k is the Boltzmann constant and T is the absolute temperature of the blackbody. The numerical integration of the radiance integral is solved by using a trapezoidal Riemann sum which is the summation of subintervals that define trapezoids to calculate area under the integral curve (Gilat & Subramaniam, 2013).

To obtain in-band temperature value of the corresponding radiance value, the unique root of the given function below has to be sought,

$$f(T_N) = \left[\int_{\lambda_1}^{\lambda_2} \frac{2c^2h}{\lambda^5} \times \frac{1}{e^{\left(\frac{hc}{kT_N\lambda}\right)} - 1} d\lambda\right] - R$$

where R is the known value of radiance and T_N is the numerically iterated absolute temperature value. The bisection method starts by determining known points a and b that define an interval where a solution exists. First estimation of the numerical solution begins with T_{N1} which is defined as,

$$T_{N1} = \frac{(a+b)}{2}.$$

Then the sign of the product $f(a) \,.\, f(T_{N1})$ is checked. If it is negative, the true solution is between a and T_{N1} and if it is positive, between b and T_{N1} the true solution can be found. The subinterval that contains the true solution is selected as the new interval $[a, b]$ and the process is repeated until T_N converges to a fixed value.

3.4.2. Ignition Delay Time

The ignition point is defined as the first point where the maximum temperature gradient is recorded (Riaza et al., 2014b). The ignition delay time is defined as the time interval between the instant when the mesh temperature reaches the desired adjusted temperature and the ignition point (see Figure 3.15). Each single particle experiment's radiance curve was converted to in-band temperature and the instances were detected accordingly.

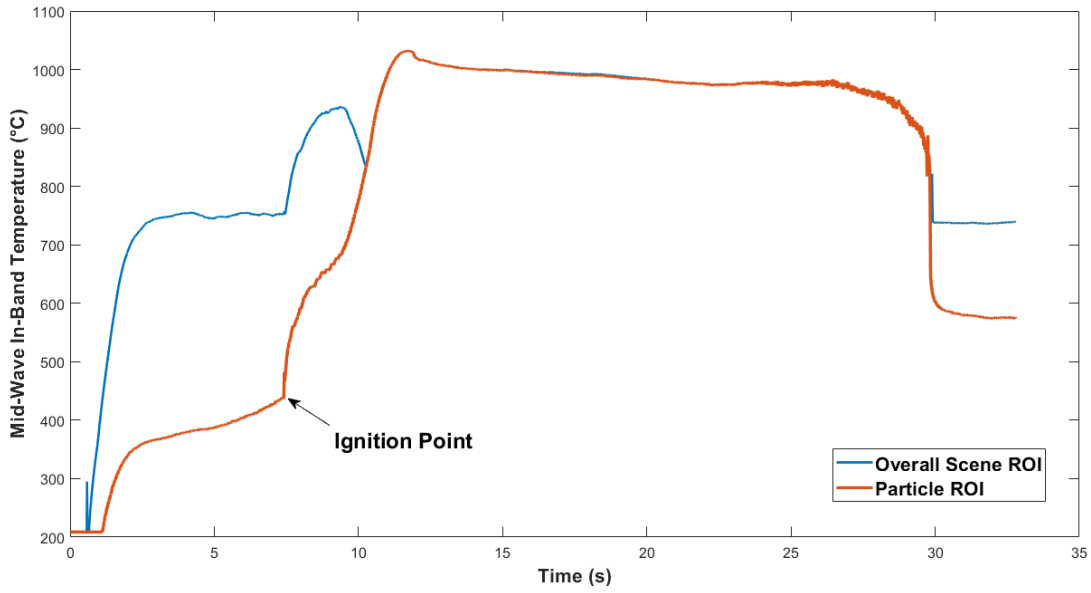

Figure 3.15. Ignition Point on In-Band Temperature Curve (ROI – region of interest)

The instant when the wire mesh setup reaches its plateau temperature was found with the help of the region of interest with greater area, that time value was subtracted from the ignition point's time value, and the ignition delay time was obtained for the single particle.

3.4.3. Volatile Combustion Time

The first stage of the two-phase biomass combustion is volatile combustion which begins with the ignition of the volatiles surrounding the particle and ends just before the char ignition. The char ignition point, necessary for the calculation of the volatile combustion time, is found as the inflection point when the phase switch occurs on the heating curve of the particle. Mathematically, this inflection point is found from the change in concavity, and the second derivative of the curve function is equal to zero. Physically, and particularly in the scope of combustion; after the volatile combustion, the particle continues to absorb energy from the wire meshes which results in increase in temperature. At some point the char is ignited, and the particle starts to release energy, emit radiation, since the reaction switches from endothermic to exothermic. In Figure 3.16, the inflection point can be seen after the first peak, which was the result of volatile flame, on the overall region of interest (ROI) curve. This heterogenous ignition onset definition based on the inflection point in single particle and coal combustion was also chosen by other researchers (Goshayeshi & Sutherland, 2014; Jovanovic, Milewska, Swiatkowski, Goanta, & Spliethoff, 2011).

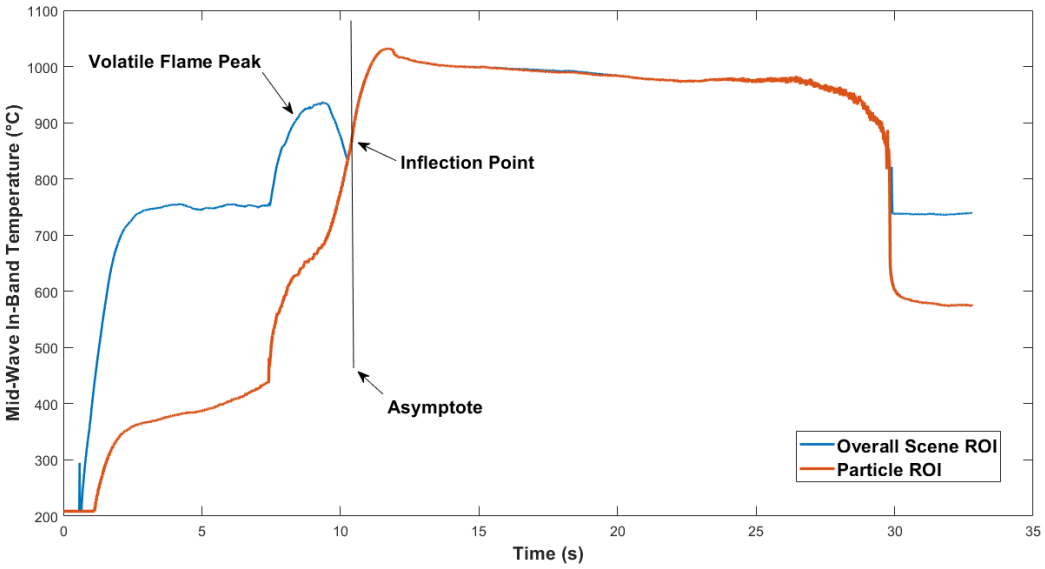

Figure 3.16. Inflection Point on Heating Curve of Olive Residue

Infrared cameras are able to sense the change in reaction kind since a sudden change in the real temperature also causes a change in the thermal radiance emitted. Herein, in order to detect the inflection point, after the first peak in the overall region of interest curve, the heating curve generated with the region of interest being the particle (see Figure 3.16) had to be sought for it. The raw data of radiance and also the converted in-band temperature data, consist of connection of discrete data points that were gathered from the camera system. The nature of data was not suitable for seeking an inflection point, because of the fact that the derivative was undefined in each connection point as shown in Figure 3.17. Therefore, a polynomial function was fitted into the raw data using MATLAB. As visible in Figure 3.17, this fitting did not extensively alter the data collected.

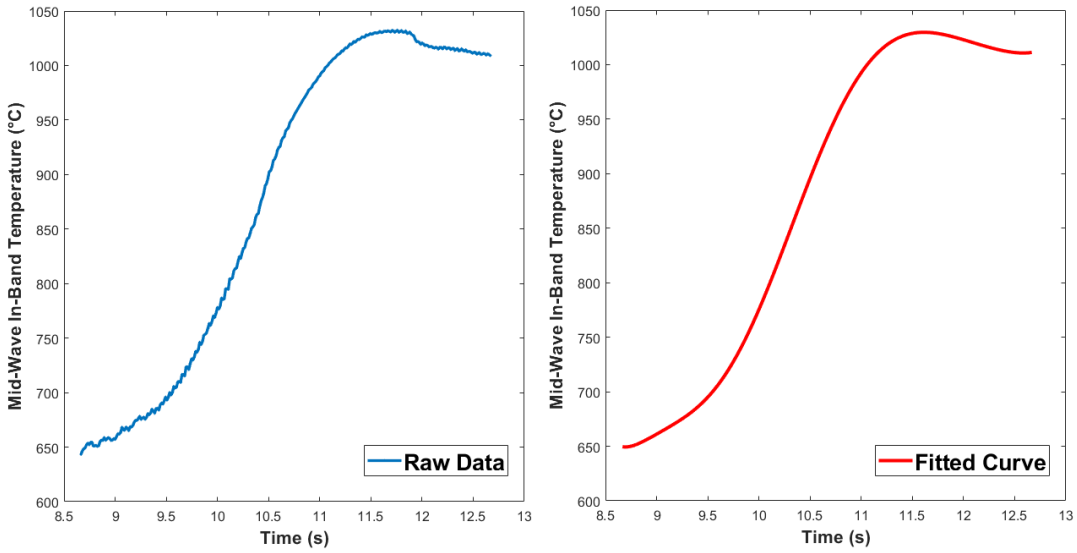

Figure 3.17. Raw Radiometric Curve and Fitted Polynomial Curve

Afterwards the raw radiometric data were fit into a 9^{th} degree polynomial, the point where the second derivative was equal to zero was found and defined as the inflection point. Resultantly; the subtraction of the time values of the inflection point and the

instant when the operating temperature was reached, yields the volatile combustion time.

3.4.4. Char Ignition Delay Time

In a two-phase heterogenous combustion, the particle ignition begins with the volatile ignition stage; after the extinction of volatile combustion the char gets ignited and the char combustion begins. As explained above, char ignition occurs at the inflection point of the radiometric heating curve of the particle. Consequently, char ignition delay time is the time difference between the instant of wire meshes reach operating temperature and the inflection point.

3.4.5. Char Combustion Time

The char combustion phase begins with the char ignition and continues until the particle undergoes extinction. In order to determine the char combustion duration, the point where the particle is extinct has to be found on the heating curve. At the instant of extinction (see Figure 3.18), the amount of radiance received from the particle drops sharply as the particle burns out and the radiance level or in-band temperature decreases to the constant operating temperature. The interval between char ignition and char extinction, yields the char combustion time.

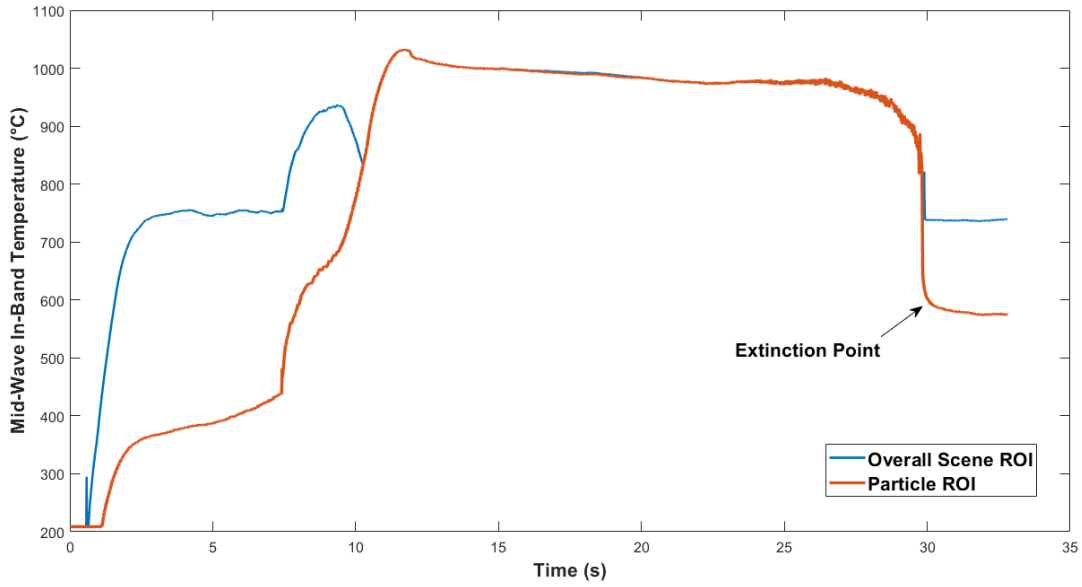

Figure 3.18. Char Extinction on the Heating Curve of Olive Residue

3.4.6. Total Combustion Time

The total combustion time, or burnout time, is defined as the time interval from the point at which the wire mesh reaches its operating temperature and the point at which the particle burns out. Therefore, it is the summation of the volatile and char combustion times. In Figure 3.19, intervals of all major parameters are shown together in heating curve of single particle olive residue. Figure 3.20 shows the entire combustion process in mid-wave and long-wave infrared together in which the radiometric events can be observed.

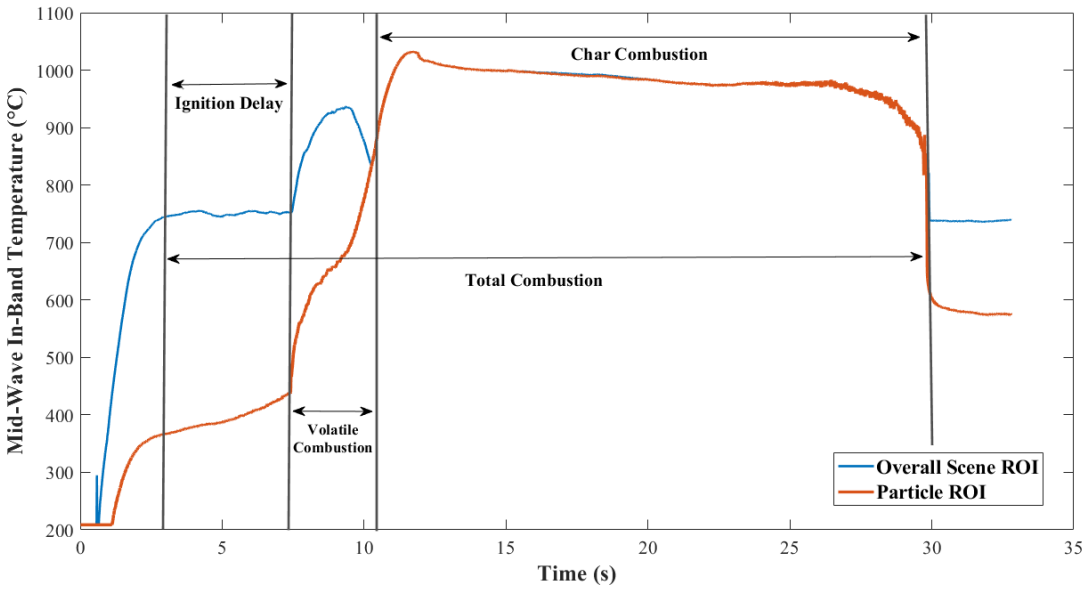

Figure 3.19. Single Particle Combustion Phases in Heating Curve of Olive Residue

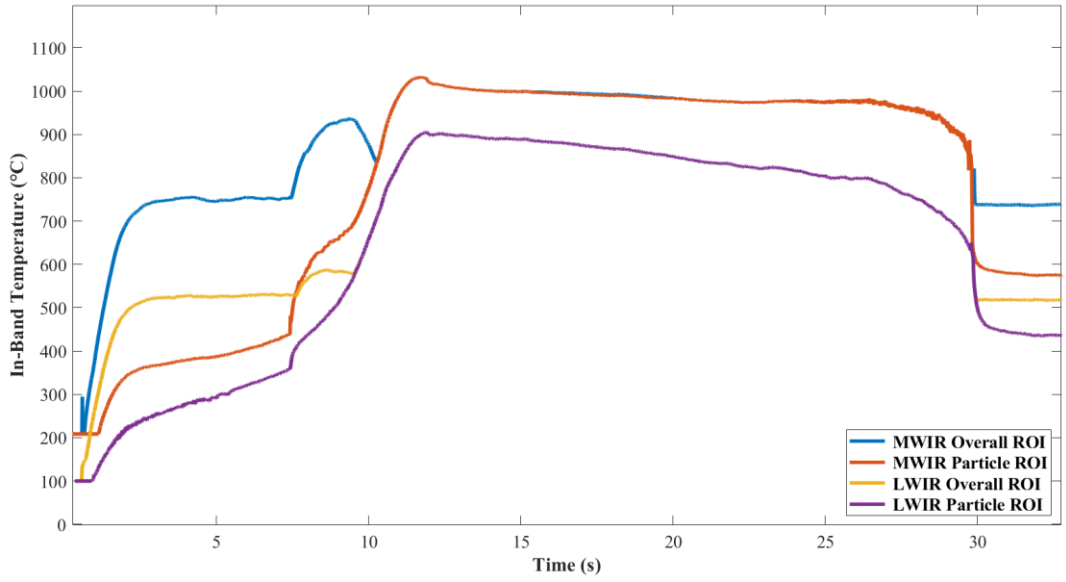

Figure 3.20. Single Particle Combustion in Mid-wave and Long-wave Infrared Heating Curve of Olive Residue

CHAPTER 4

RESULTS AND DISCUSSION

The results of two wire mesh configurations are presented and discussed herein. In horizontal configuration experiments, the wire mesh setup is explored by investigating the temperature distribution among the meshes and the validation of the wire mesh setup and the infrared sensing system is aimed. Temperature standard deviations on the wire meshes, applicability of a combustion experiment using a single layer of olive residue particles, and the effect on the temperature distribution of choosing a new or used mesh are reported. On the other hand, the vertical configuration results focus on the olive residue single particle combustion and on the influence of particle mass, investigated through determination and comparison of combustion parameters. Distinctions between measurement of combustion in mid-wave and long-wave infrared are pointed out and discussed. Single particle Tunçbilek lignite combustion results are also presented to compare with olive residue samples.

4.1. Horizontal Mesh Configuration

Infrared measurement of horizontal mesh configuration has revealed useful information about utilization of the setup and the temperature distribution on the wire meshes in different spectral bands. Horizontal configuration experiments were conducted to show that the wire mesh reactor setup can be operated at distinct temperatures and maintain a homogenous temperature distribution over the whole mesh region. The usability of the wire mesh setup and the infrared sensing capability were validated herein. Additionally, quantitative wire mesh and pulverized olive residue combustion results are presented in this section.

4.1.1. Wire Mesh Temperature Distribution

Before any kind of combustion experiment was conducted, the homogeneity of the temperature distribution has to be observed since the particle or particles have to be exposed to same heat flux simultaneously to emulate power plant furnace conditions. In this section, results of wire mesh at two different operating temperatures, 900 ℃ and 1100 ℃ are shown. In Figure 4.1 and Figure 4.2, the infrared images of meshes at different temperatures are seen in mid-wave and long-wave bands, respectively. These infrared images were obtained upon reaching steady temperature conditions (i.e. when the mean temperature reached a steady value). A few hotspots on the wire mesh have been detected although the related areas can be considered too small to affect the combustion process and consequently the measurement of it. Infrared images show that hotspots become more distinctive in the hotter (1100 ℃) mesh than the cooler (900 ℃) one. Impurities on the mesh were able to be spotted by both of the infrared cameras. As expected, mid-wave and long-wave cameras show consistent locations of hotspots even though their radiance and in-band temperature readings of those spots are different as governed by Planck's radiation law.

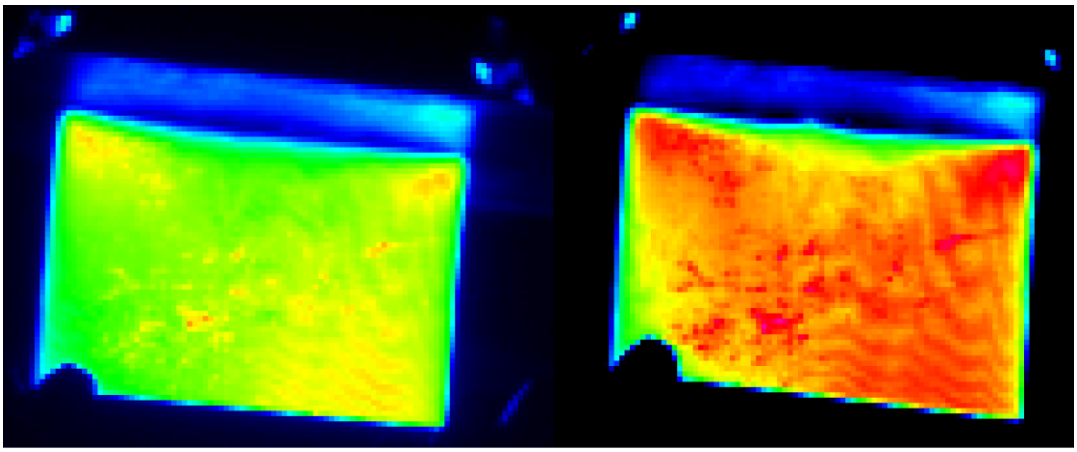

Figure 4.1. Wire Mesh Images in Mid-wave Infrared Camera at 900 ℃ (left-hand side) and 1100 ℃ (right-hand side)

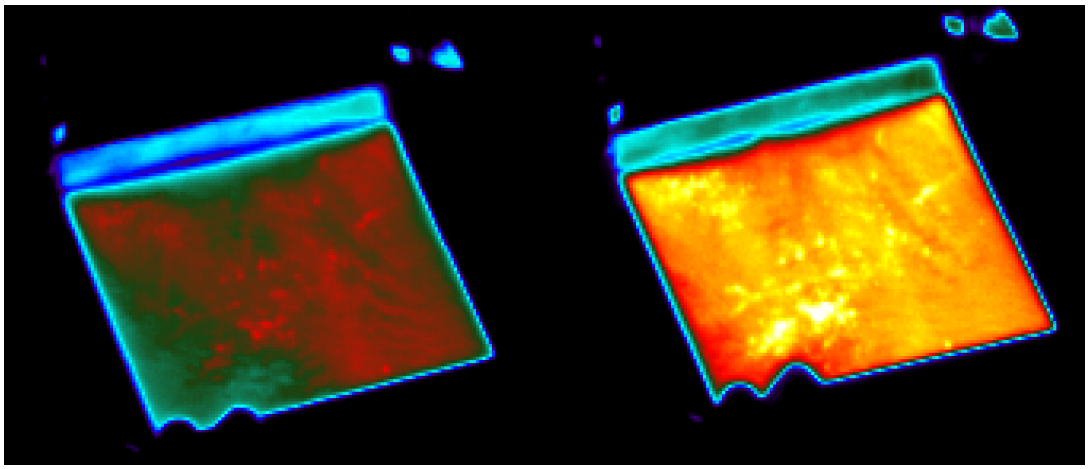

Figure 4.2. Wire Mesh Images in Long-wave Infrared Camera at 900 ℃ (left-hand side) and 1100 ℃ (right-hand side)

Visual inspection of infrared images can spot the irregularities in wire mesh qualitatively, however, quantitative analysis is needed to interpret homogeneity of the temperature distribution along the mesh. Value of each pixel that defines the wire mesh region was gathered and plotted as three dimensional surfaces in Figure 4.3 and Figure 4.4 as mid-wave and long-wave in-band temperatures, respectively. Similar to the previous infrared images in Figure 4.1 and Figure 4.2, three dimensional surface plots also belong to a certain instant when the steady mean temperature is achieved. In these figures, x and y axes represent a pixel's coordinate in respective camera's image detector and those values are generated internally by the camera. As it is not possible to determine the real temperature, the z axis represents the corresponding in-band temperature which is lower than the real temperature of mesh because only a specific part of thermal radiation band is measured by the infrared cameras and the variance in z-axis data is investigated for temperature distribution.

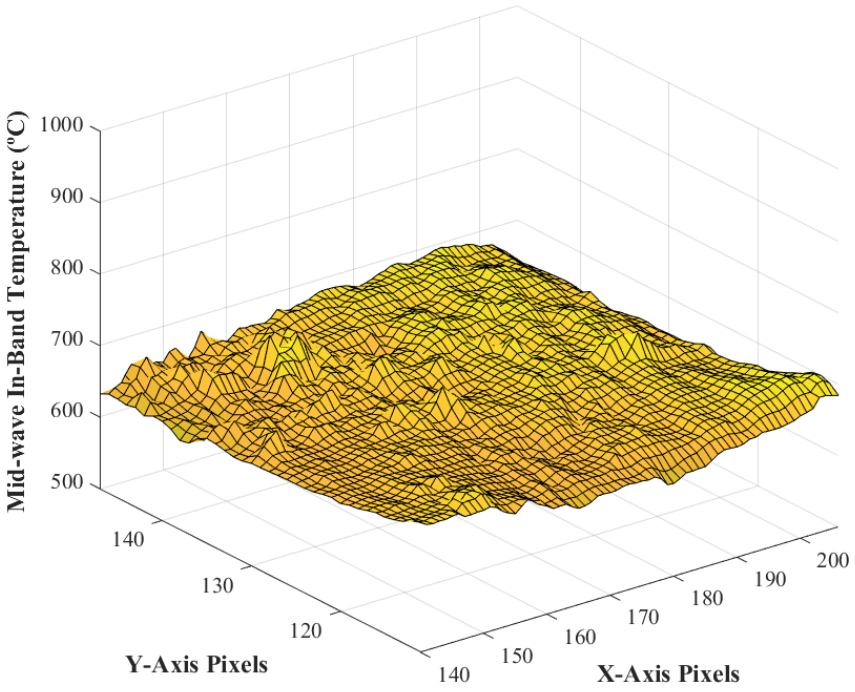

(a)

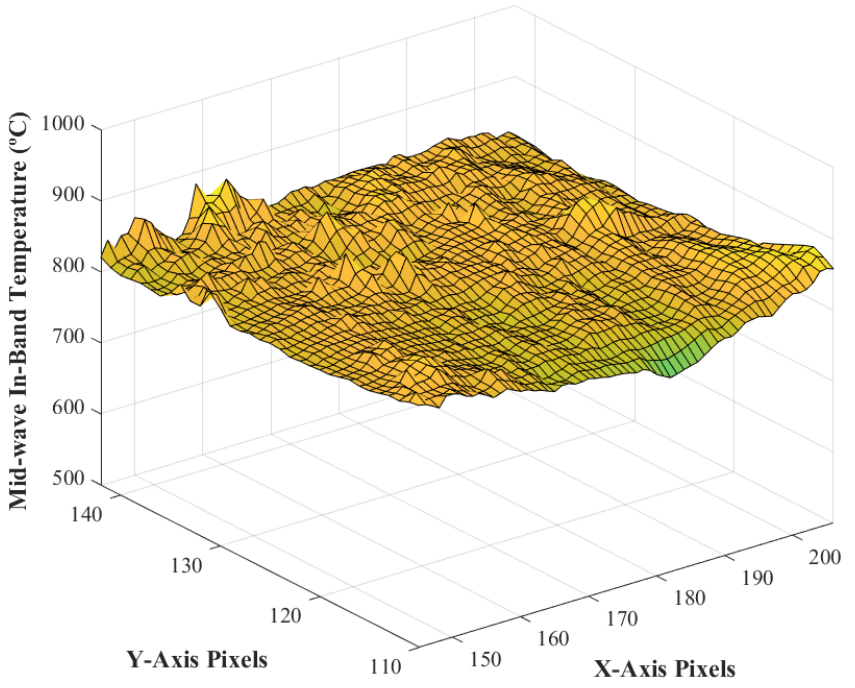

(b)

Figure 4.3. Mid-wave In-Band Temperature Distribution of (a) 900 ℃ Mesh and (b) 1100 ℃ Mesh

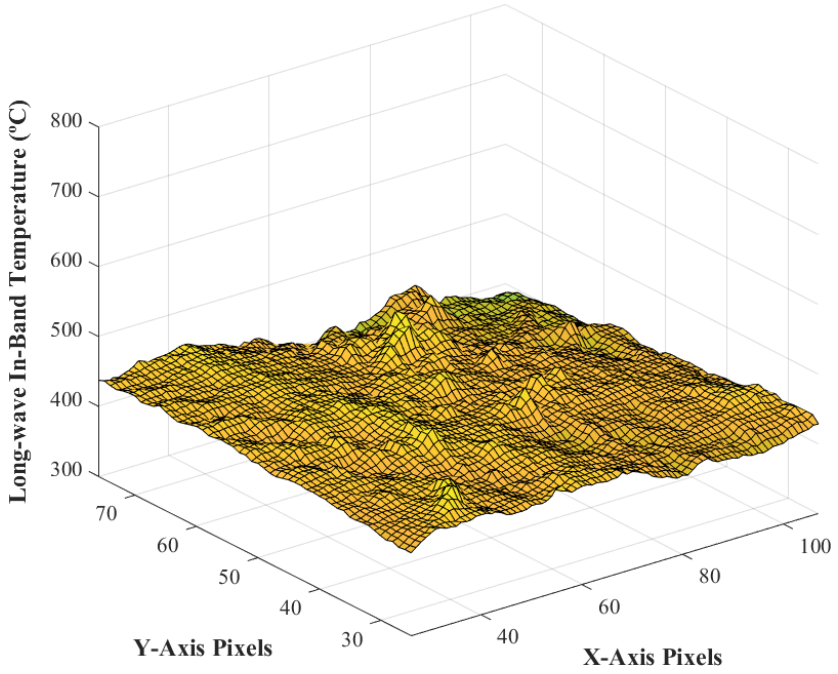

(a)

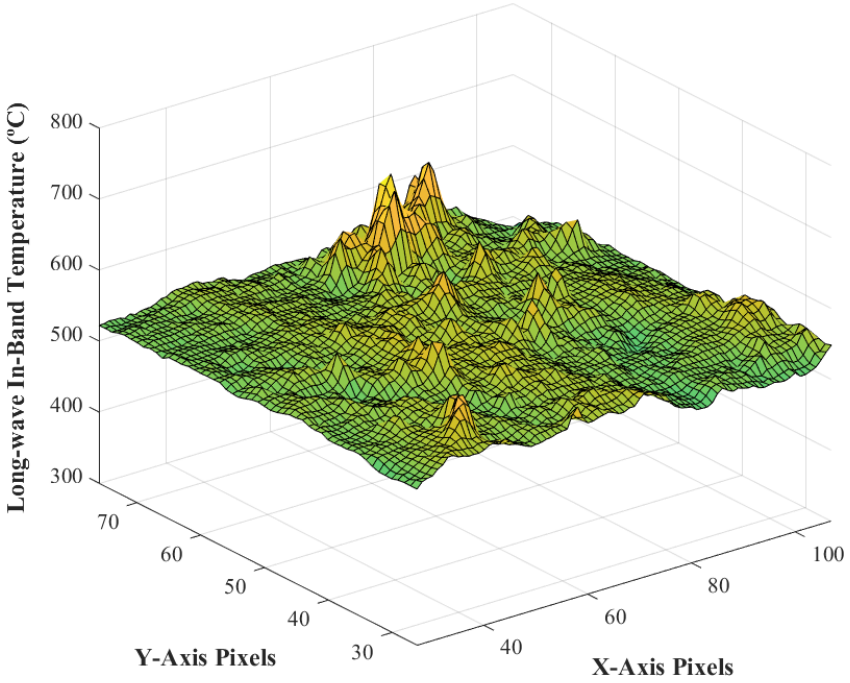

(b)

Figure 4.4. Long-wave In-Band Temperature Distribution of (a) 900 ℃ Mesh and (b) 1100 ℃ Mesh

Each mesh temperature configuration is measured at least twice with both of the infrared cameras and averaged values of important parameters like mean temperature values and standard deviations for both operating temperature cases are tabulated in Table 4.1. It should be noted that results of the individual combustion experiments differed ~4% from the averaged values where the radiometric cameras have 2% accuracy, hence the average values were confidently tabulated.

Due to the fact that infrared cameras sense the radiation in their respective spectral range (see Section 3.2.2), the primary outputs of the experiments are average mean and maximum radiance values along the wire mesh. Average of the mean radiance measured in mid-wave infrared is 78 and 79 percent of the average maximum radiance for 900 ℃ and 1100 ℃, respectively. Similarly, in long-wave infrared, 81 and 70 percent of the average maximum radiance was recorded as the average mean radiance for 900 ℃ and 1100 ℃, respectively.

In terms of temperature, in mid-wave infrared, 91 percent of the average maximum was observed as the average mean for both operating temperatures. Long-wave camera recorded 87 and 78 percent of the average maximum temperature as the average mean for 900 ℃ and 1100 ℃ meshes, respectively. The average standard deviation of temperature in 900 ℃ mesh in mid-wave infrared was calculated as 42.7 ℃, and as the temperature of the mesh increases to 1100 ℃, the deviation increases to 46.3 ℃ (see *Table 4.1*). An analogous change was also observed in long-wave infrared when the operating temperature of the mesh was increased from 900 ℃ to 1100 ℃, the average standard deviation of temperature increased to 39.7 ℃ from 31.9℃ (see *Table 4.1*).

Table 4.1. *Mid and Long-wave Infrared Measurement Results of 900 ℃ and 1100 ℃ Meshes*

Mid-wave Infrared	*900* ºC	*1100* ºC
Average Maximum Radiance (W/m^2/sr)	6913.8	12148.5
Average Mean Radiance (W/m^2/sr)	5418.7	9610.3
Average Standard Deviation (W/m^2/sr)	861.5	1288.3
Average Maximum Temperature (In-Band ºC)	710.9	878.9
Average Mean Temperature (In-Band ºC)	649.2	801.2
Average Standard Deviation (In-Band ºC)	42.7	46.3
Long-wave Infrared		
Average Maximum Radiance (W/m^2/sr)	866.8	1407.9
Average Mean Radiance (W/m^2/sr)	708.4	982.6
Average Standard Deviation (W/m^2/sr)	79.5	107.9
Average Maximum Temperature (In-Band ºC)	475.9	662.5
Average Mean Temperature (In-Band ºC)	415.9	517.1
Average Standard Deviation (In-Band ºC)	31.9	39.7

The measured temperature values of mid-wave camera were reported as higher than long-wave camera. This result is justified by Planck's radiation law (see Figure 4.5) since the integration between the mid-wave band's boundary wavelengths yields higher amount of radiation than long-wave band's. In a similar manner, as the temperature of the mesh went up by 200 ℃ from 900 ℃ to 1100 ℃, the average mean temperature increased in mid-wave by 152 ℃, whereas in long-wave the increase was 101 ℃. This difference is caused by Wien's displacement law, as the temperature increases Planck curve shifts to shorter wavelengths.

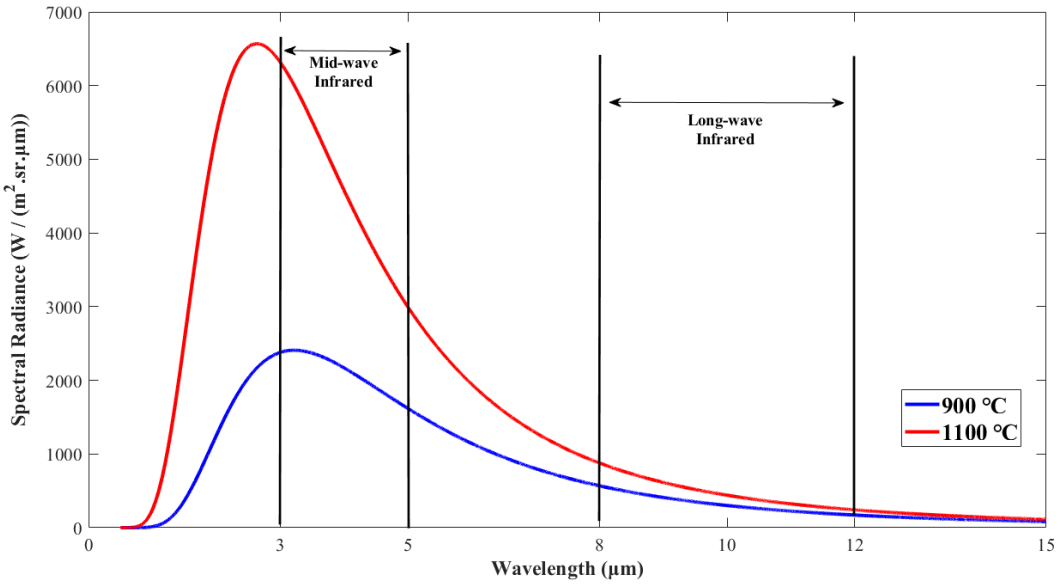

Figure 4.5. Mid and Long-wave Infrared Regions in Planck's Radiation Curve for 900 ℃ and 1100 ℃ meshes

In summary, the temperature distribution of the wire meshes was measured in different spectral bands and considered homogeneous with a mid-wave average standard deviation of 6 percent and a long-wave average standard deviation of 7 percent of the respective mean temperatures.

4.1.2. Wire Mesh Heating and Cooling Rate

The wire mesh's heating and cooling rates are important since the combustion characteristics specifically combustion durations heavily depend on them (Magalhães, Kazanç, Ferreira, Rabaçal, & Costa, 2017). Especially in combustion experiment configurations where the fuel is not in contact with meshes and not replaced in a series of experiment, the cooling rate determines the minimum time between two consecutive experiments. In order to ensure a steady heating rate, heating and cooling procedures were recorded for each mesh temperature configuration. Measurements were done at least in duplicate for both in mid-wave and long-wave infrared whilst the

thermocouple also recorded the real temperature of the mesh. Figure 4.6 shows the mean temperature value of the wire mesh area during heating and cooling procedure in long-wave infrared band.

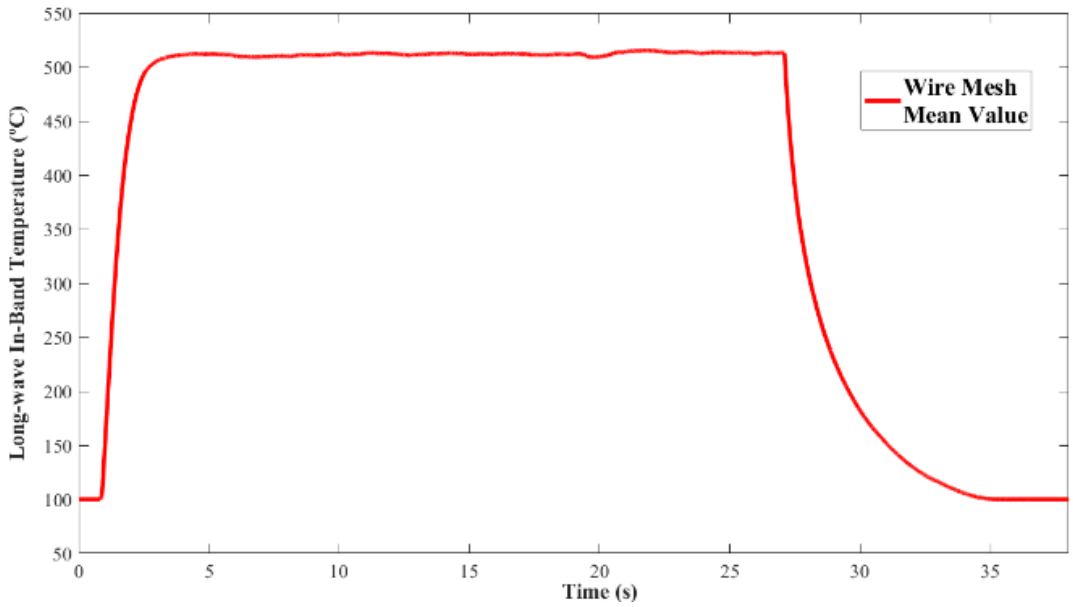

Figure 4.6. Heating and Cooling Profile of a 1100 ℃ Wire Mesh (Long-wave Infrared In-Band Mean Temperature Values)

Average values of the experiments conducted are tabulated in *Table 4.2*. The results of each individual experiment differed ~3% from the reported average values for both thermocouples and infrared cameras. The in-band temperature values which are deduced from the radiance value obtained from both of the cameras, showed an overall profile which was in parallel with the data from the thermocouple welded unto the mesh. Long-wave camera can only sense above 100 ℃ and mid-wave above 200 ℃. This meant that during the calculation of the cooling rate, temperatures below those values were not considered, and that consequently, the actual cooling duration of the mesh configurations are higher. Across all mesh temperatures and all spectral bands, the heating duration from radiometric data differed in 10-40 milliseconds when

compared to the durations acquired from the thermocouple. As expected, the cooling rate measured by infrared cameras increased with an increase in the wire mesh temperature because higher temperature difference between the mesh and ambient result in higher convective and radiative heat transfer rate.

Table 4.2. *Average Heating and Cooling Data of a Wire Mesh at 900 ℃ and 1100 ℃ in Mid-wave and Long-wave Infrared*

Mid-wave Infrared	*900* ºC	*1100* ºC
Average Mean Temperature (In-Band ºC)	649.2	801.2
Average Thermocouple Heating Duration (s)	2.65	1.83
Average Heating Duration (s)	2.62	1.87
Average Heating Rate (In-Band ºC/s)	247.8	428.5
Average Cooling Duration (s)	3.63	4.21
Average Cooling Rate (In-Band ºC/s)	178.84	190.31
Long-wave Infrared		
Average Mean Temperature (In-Band ºC)	415.9	517.1
Average Thermocouple Heating Duration (s)	2.65	1.83
Average Heating Duration (s)	2.69	1.84
Average Heating Rate (In-Band ºC/s)	154.61	281.03
Average Cooling Duration (s)	6.31	7.54
Average Cooling Rate (In-Band ºC/s)	65.91	68.58

As the mesh temperature increased, the measured radiation from the mesh also increased as expected without any decrease in radiance that might be caused by the spectral emissivity of mesh material at different temperatures, stainless-steel (SS-316). Infrared camera inspection results in both spectral bands show that the wire mesh

setup can operate with a high heating rate and the minimum amount of time to use the wire mesh setup again was stated.

4.1.3. Pulverized Olive Residue Combustion Results

In this section, results from olive residue combustion experiments conducted in horizontally configured mesh as a part of validation of the experimental apparatus (wire mesh setup and infrared sensing system), are reported. The wire mesh setup was able to successfully combust the pulverized single layer of fuel meanwhile the distinct combustion phases were able to be detected both in mid-wave and long-wave infrared bands. The combustion stages were identified qualitatively as shown in the infrared image sequences in Figure 4.7 and Figure 4.8 for mid-wave and long-wave, respectively. In these figures, the first infrared frame shows the heating of particle and mesh together before the ignition, later it is followed by ignition and subsequent flames of volatile matter combustion (second frame – b). After the volatile combustion stage, the char combustion begins (third frame – c). At the end, the radiating region shrinks as the fuel burns out and only the radiating region of the ash remains (fourth frame – d). Additionally, it has been observed that volatile flames were more distinguishable in mid-wave band than long-wave.

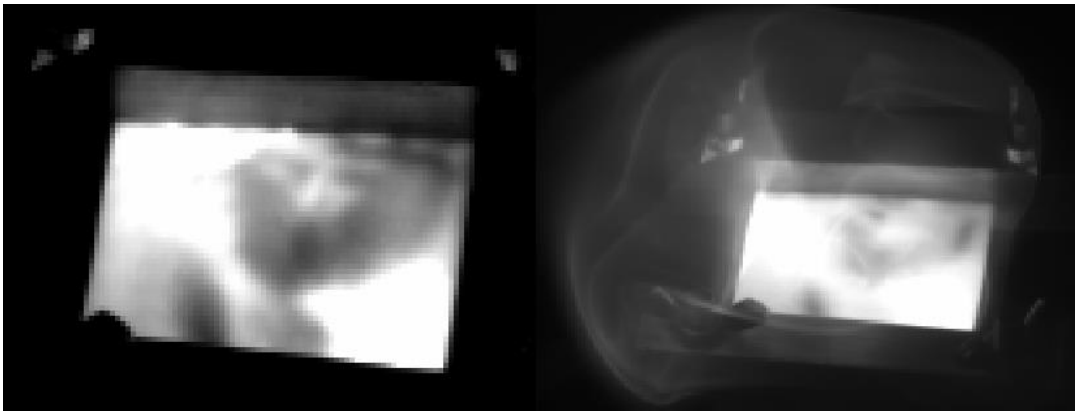

(a) (b)

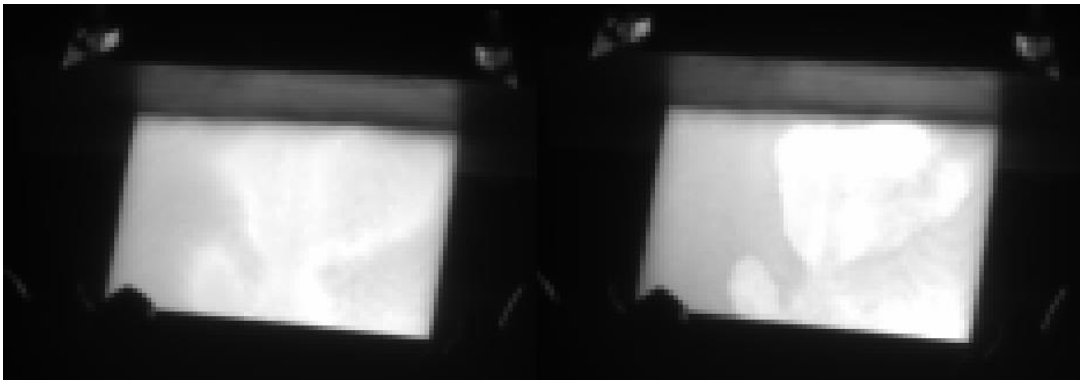

(c) (d)

Figure 4.7. Mid-wave Infrared Images of the Combustion Stages of 50 mg of Olive Residue: (a) heating and pre-ignition (b) ignition and volatile combustion (c) char combustion (d) burnout

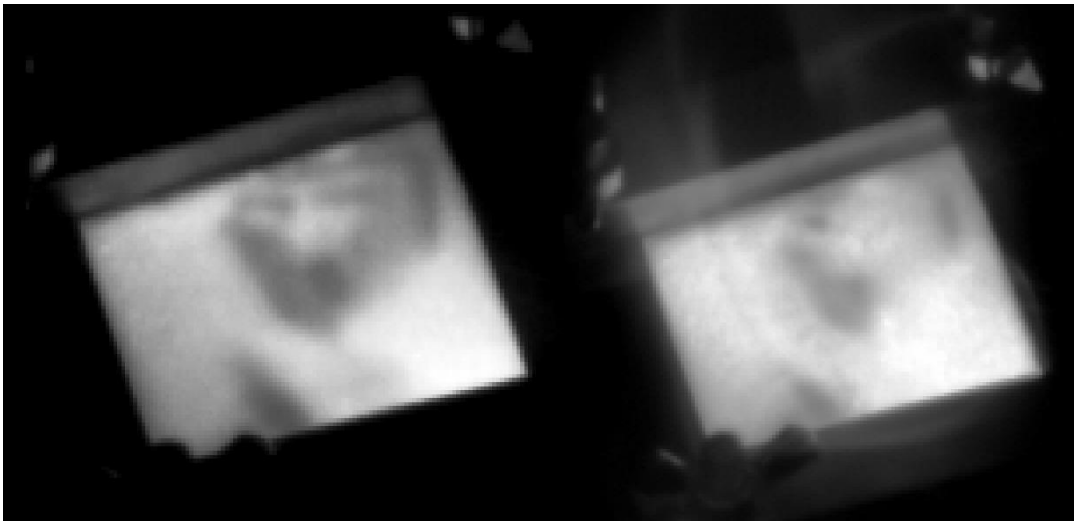

(a) (b)

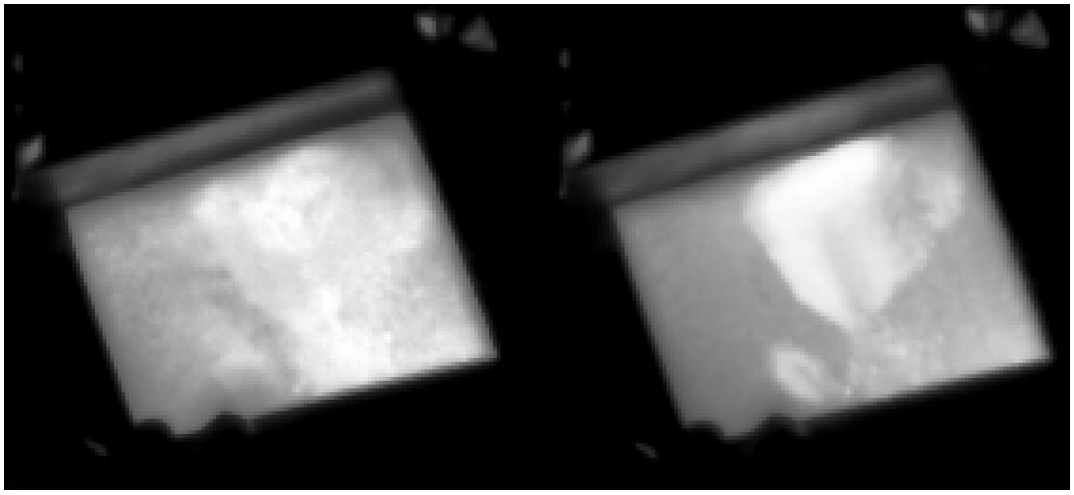

(c) (d)

Figure 4.8. Long-wave Infrared Images of the Combustion Stages of 50 mg of Olive Residue: (a) heating and pre-ignition (b) ignition and volatile combustion (c) char combustion (d) burnout

The maximum deduced temperature from the radiometric signals in the wire mesh area during the combustion process were plotted orderly in Figure 4.9 and Figure 4.10 for mid-wave and long-wave infrared. In these radiometric plots, despite obtaining two separate combustion peaks as expected from biomass combustion (Magalhães, Panahi, et al., 2019; Mason et al., 2015), quantitative assessment of volatile and char ignition points from the measured radiance values was not possible. This result is attributed to the fact that in pulverized form the ignition occurs rapidly, and the fuel and the mesh are in contact together, which results in the overlapping of the measured spectral radiance from the mesh and fuel sample. On the other hand, the burnout instant of the fuel was detected as the radiometric signal received reaches at a constant value which is the operating condition of the wire mesh (see Figure 4.9 and Figure 4.10).

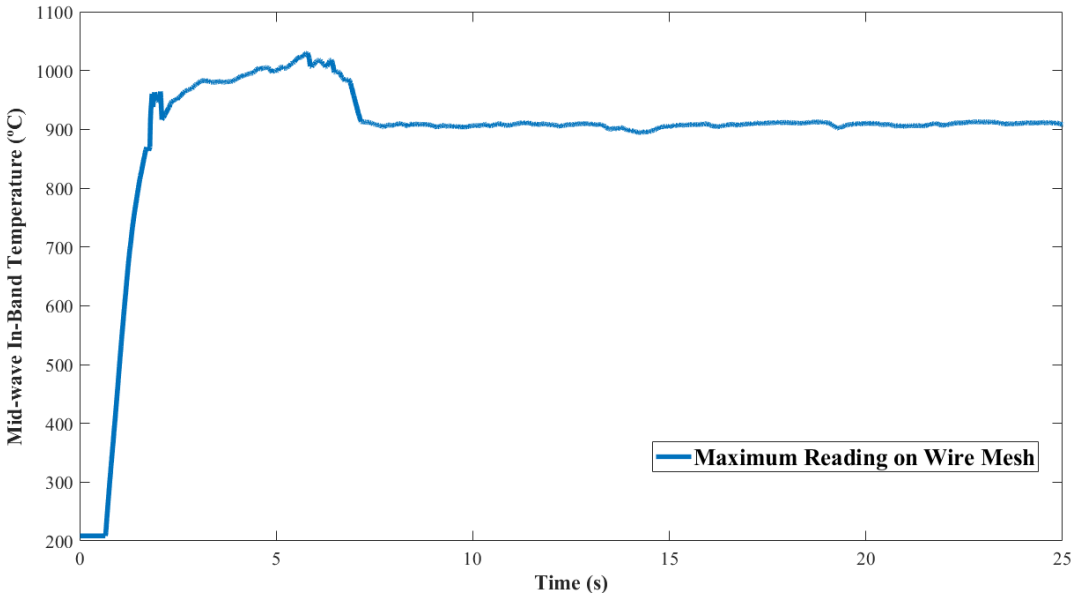

Figure 4.9. Measured Maximum Temperature in Mid-wave Infrared during Olive Residue Combustion with Horizontal Mesh

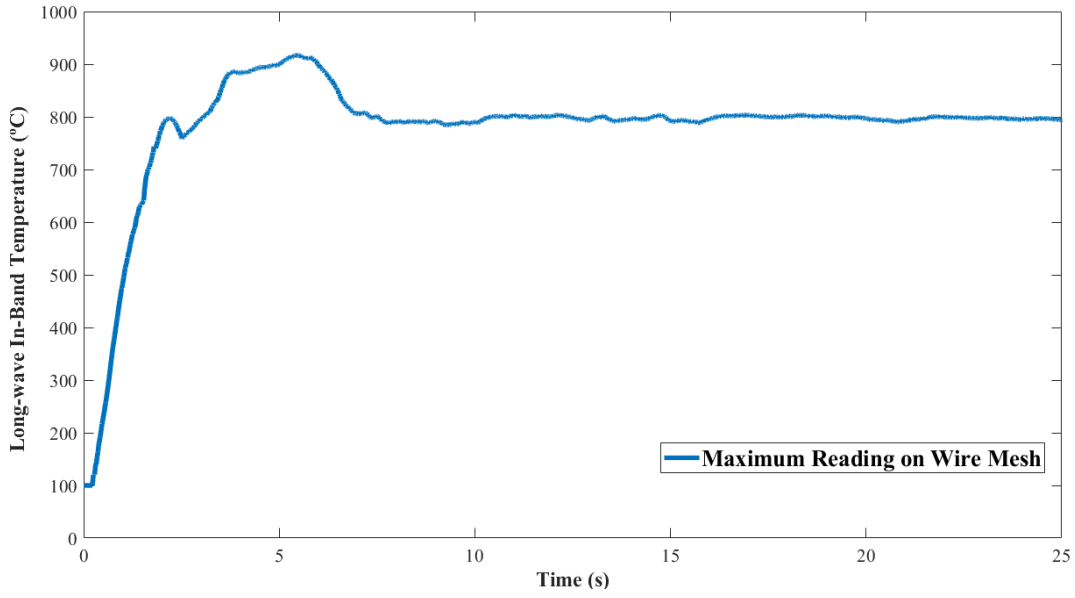

Figure 4.10. Measured Maximum Temperature in Long-wave Infrared during Olive Residue Combustion with Horizontal Mesh

In *Table 4.3* the average combustion measurement data are tabulated for both spectral bands. It should be noted that the results of each individual combustion experiment did not differ more than 5% from the reported average values. Due to the fact that hotter objects emit greater portion of their spectral radiance in shorter wavelengths, as governed by Wien's displacement law, average peak combustion and radiance values were found to be greater in mid-wave than the long-wave band. Although the measured values are different in both bands, the combustion burnout duration is reported to be the same. This concurrency in the result is due to the fact that an increase in temperature shifts the Planck's radiation curve to higher values in all wavelengths of thermal radiation spectrum. Consequently, without considering the absolute value obtained from the measurement, higher amount of radiance corresponds to higher temperature in a certain spectral band.

Table 4.3. *Average Combustion Data of 50mg Olive Residue in Horizontal Mesh Configuration in Mid-wave and Long-wave Infrared*

Mid-wave Infrared	
Average Peak Combustion Radiance ($W/m^2/sr$)	15985.3
Average Peak Combustion Temperature (In-Band ºC)	979
Average Combustion Burnout Duration (s)	6.13
Long-wave Infrared	
Average Peak Combustion Radiance ($W/m^2/sr$)	2207.6
Average Peak Combustion Temperature (In-Band ºC)	911.7
Average Combustion Burnout Duration (s)	6.13

The results of this subsection comprise, the applicability and validation of the infrared remote sensing system coupled with wire mesh for combustion experiments. In both

spectral bands, it is possible to measure combustion radiometrically and conclusions can be drawn based on timings of radiometric events.

4.1.4. Effect of Reusing Wire Mesh

At the end of the combustion process, the inorganic content, ash, that did not vaporize remains. In such configuration of the wire mesh setup where the mesh is in contact with the fuel, ash leftovers remain on the mesh. After an experiment is conducted, the effect of the leftover ash on the radiance sensed can be qualitatively distinguished in infrared images of both mid-wave and long-wave cameras (see Figure 4.11 and Figure 4.12). Investigation of the quantitative effect of leftover ash is conducted in this section and the necessity of using a new mesh in each and every experiment is discussed.

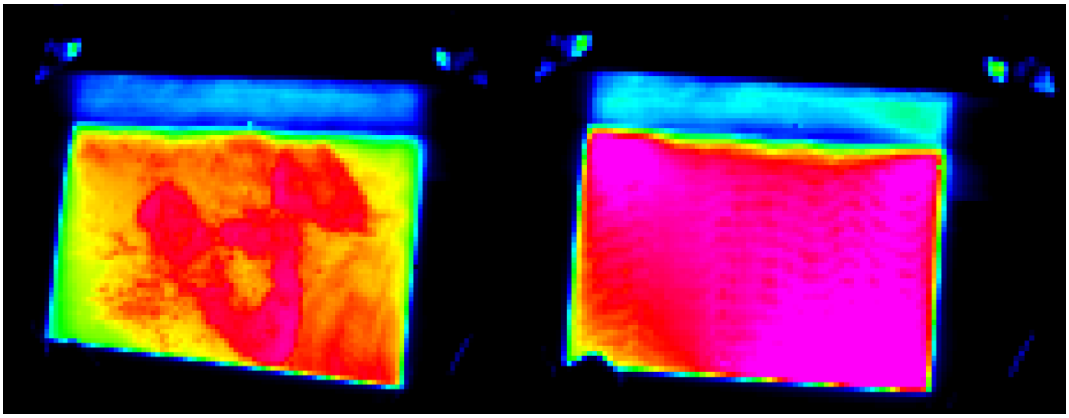

Figure 4.11. Infrared Mid-wave Images of Used (left-hand side) and New (right-hand side) Wire Mesh at 1100 ℃

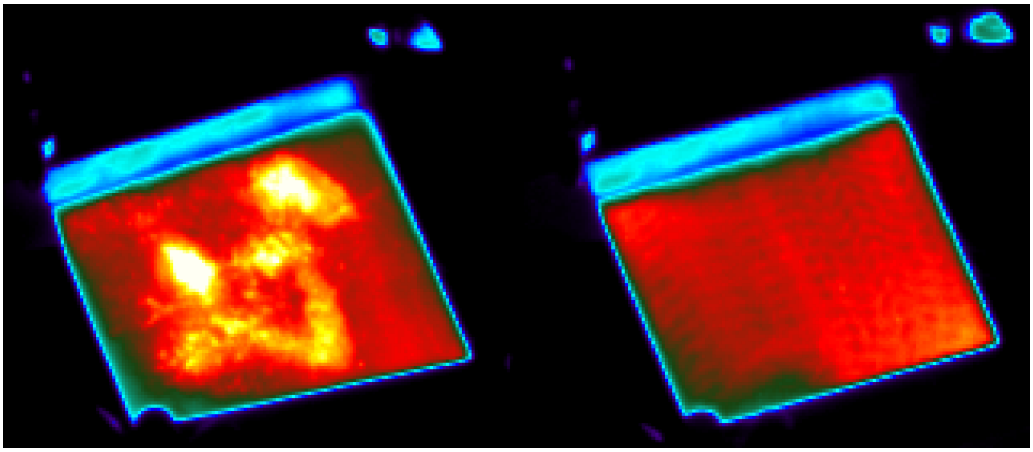

Figure 4.12. Infrared Long-wave Images of Used (left-hand side) and New (right-hand side) Wire Mesh at 1100 ℃

Three dimensional plots of new and used wire meshes in mid-wave and long-wave infrared are given in Figure 4.13 and Figure 4.14, respectively. These figures represent the instant when the mean temperature value of the mesh is steady, and the operating temperature is 1100 ℃. In the figures, the z axis value is the calculated in-band temperature of corresponding pixels and the quantitative comparison of used and new mesh was made according to that data.

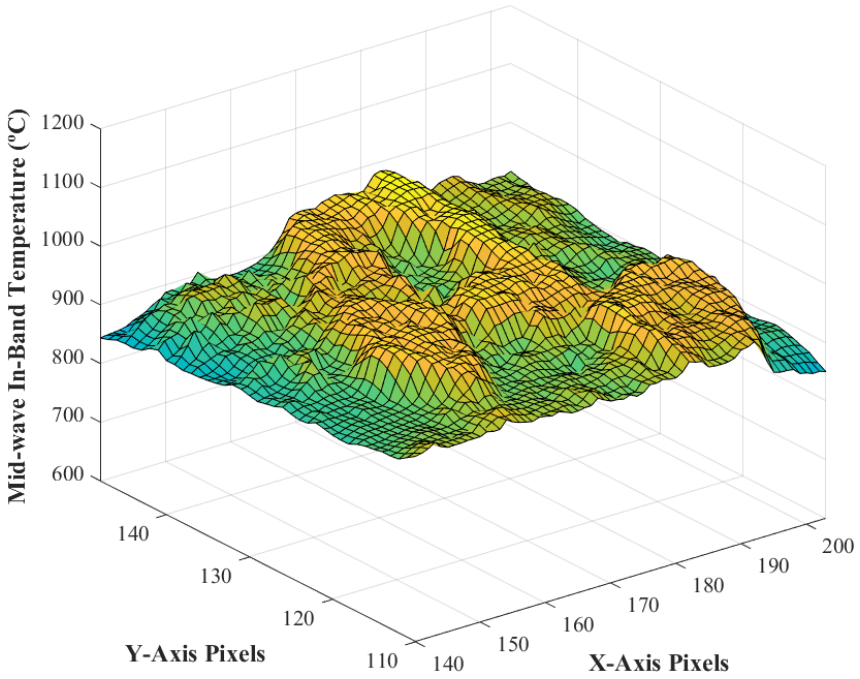

(a)

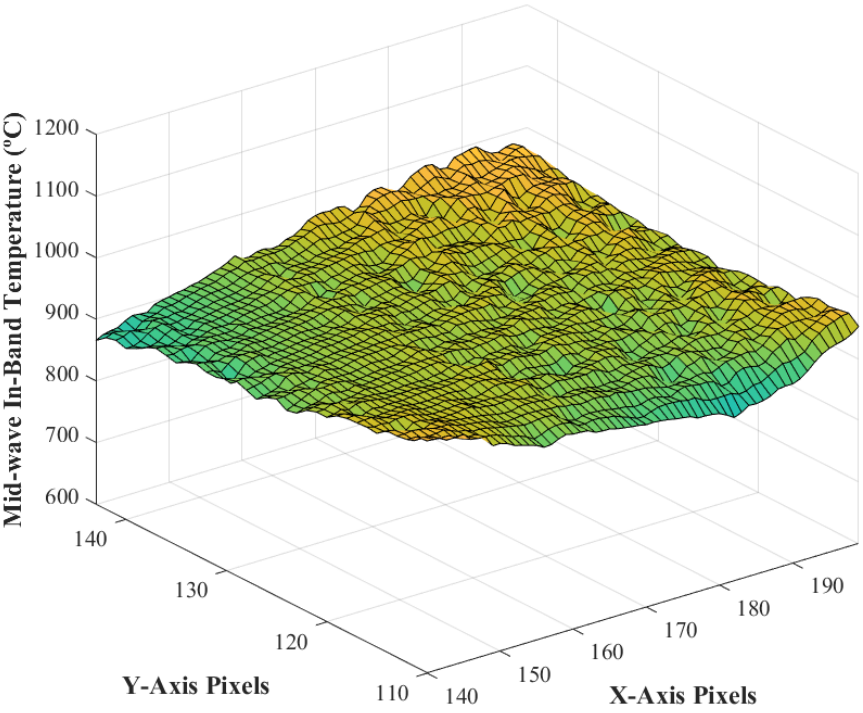

(b)

Figure 4.13. Used (a) and New (b) Mesh at 1100 ℃ in Mid-wave Infrared

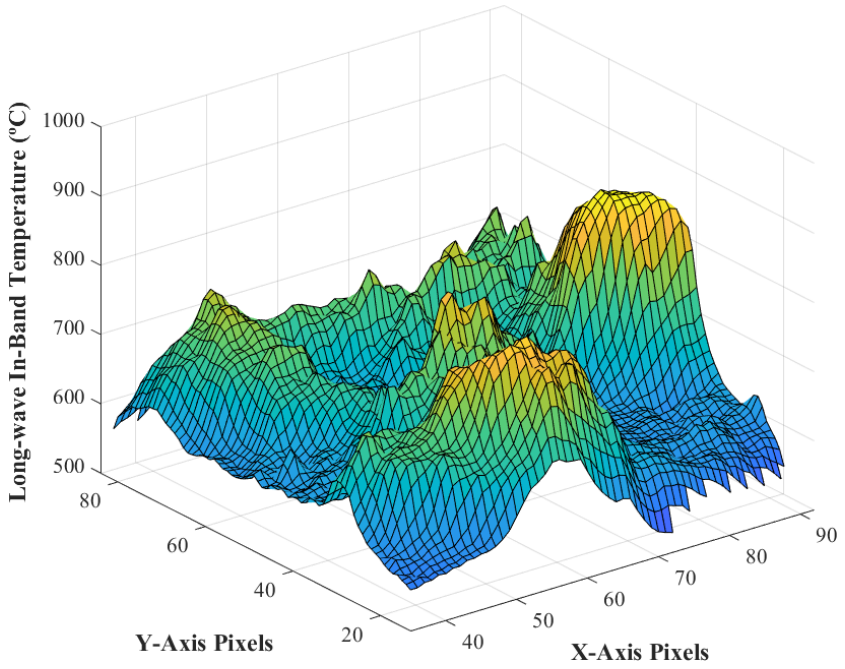

(a)

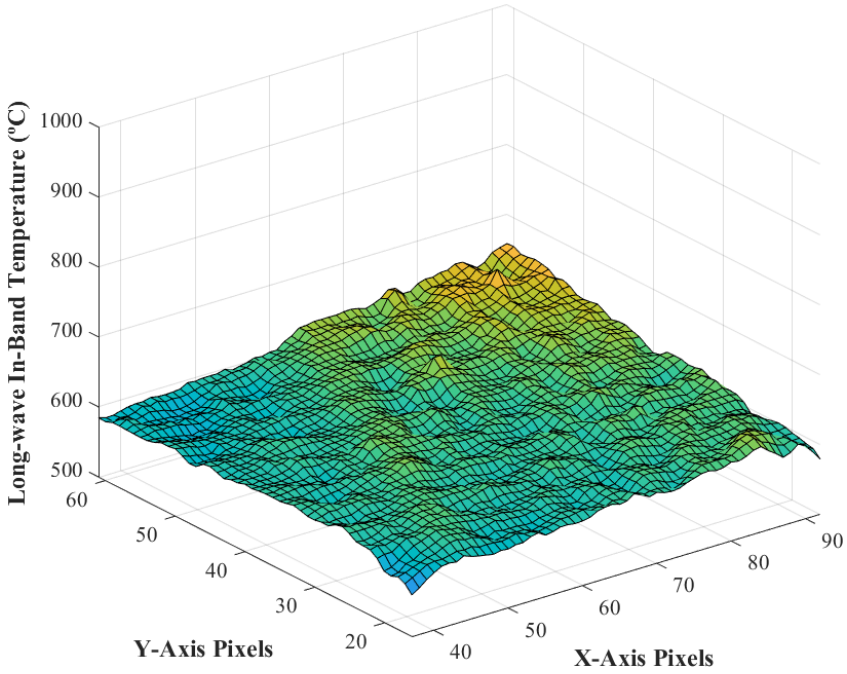

(b)

Figure 4.14. Used (a) and New (b) Mesh at 1100 °C in Long-wave Infrared

The quantitative results of used and new mesh in both spectral bands are tabulated in *Table 4.4* below. On the one hand, mid-wave infrared data shows that the mean temperature of the new mesh is 22 ℃ higher than that of the used mesh. On the other hand, long-wave results indicate that used mesh has a mean temperature 26 ℃ higher than the new one. In spite of the discrepancy about which mesh has the highest mean temperature, an increase in standard deviation for the used mesh is observed in both spectral bands. Especially, in long-wave measurements, using a used mesh instead of a new mesh increases the standard deviation of temperature along the mesh by 42 percent.

Table 4.4. *Results of Used and New Mesh at 1100 ℃ in Mid-wave and Long-wave Infrared*

Mid-wave Infrared	*Used Mesh*	*New Mesh*
Maximum Radiance ($W/m^2/sr$)	16189.3	18244.2
Mean Radiance ($W/m^2/sr$)	13407.7	14230.7
Standard Deviation ($W/m^2/sr$)	1269.2	1165.4
Maximum Temperature (In-Band ºC)	985.8	1035.6
Mean Temperature (In-Band ºC)	912.9	935.1
Standard Deviation (In-Band ºC)	34.8	30.9
Long-wave Infrared		
Maximum Radiance ($W/m^2/sr$)	2066.5	1477.1
Mean Radiance ($W/m^2/sr$)	1311.9	1222.3
Standard Deviation ($W/m^2/sr$)	196.6	81.7
Maximum Temperature (In-Band ºC)	871.1	685.2
Mean Temperature (In-Band ºC)	626.4	600.5
Standard Deviation (In-Band ºC)	66.4	27.8

The disparity between the two spectral bands indicates that the leftover ash exhibits a selective radiator behavior according to the wavelength. In mid-wave infrared measurement lower amount of radiance was obtained from the used mesh when compared with the new mesh, however, long-wave radiance measurements indicate

just the opposite. This outcome can be attributed to the fact that olive residue ash contents spectral emissivity value is different in mid-wave and long-wave infrared. Since there is no study in literature that reports the spectral emissivity values of Turkish olive residue ash, it is not possible to check the discrepancy quantitively. In order to compare the result qualitatively, a fuel ash which has similar content with Turkish olive residue ash (see inorganic species in *Table 3.1*) has been investigated. A study on Absaloka coal ash emissivity (Zygarlicke, McCollor, & Crocker, 1999), conducted at 925 ℃, can be considered close to the present study in this thesis. It should be noted that comparison of the emissivity at high temperature is crucial since spectral emissivity changes at elevated temperatures. In Figure 4.15, the relative emissions of Absaloka coal in different wavelengths are shown.

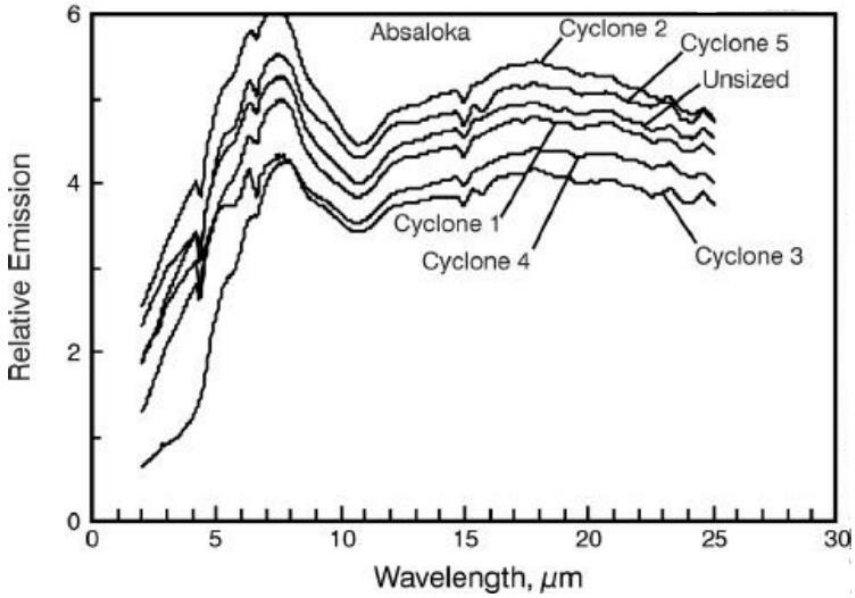

Figure 4.15. Relative Emission of Absaloka Coal Ash at 925 ℃ (Zygarlicke et al., 1999)

Although the relative content of inorganic species in Turkish olive residue ash is different from Absaloka coal, Figure 4.15 shows that the inorganic species in that coal radiate differently in mid-wave and long-wave infrared by nearly two-fold. Hence, the

difference in measurement of used and new mesh originates from the spectral emissivity of inorganic contents of Turkish olive residue.

The given results prove that utilizing the same mesh in more than a single experiment results in higher standard deviation in wire mesh temperature and alters the homogeneity of temperature on the mesh as observed in both spectral bands. It has been shown that contamination of the mesh from a previous combustion experiment affected the infrared sensing results. Using a new mesh in each experiment is expected to yield a more uniform heat flux from the meshes to the fuel particle or particles.

4.2. Vertical Mesh Configuration

In this wire mesh reactor configuration, the fuel in single particle form does not contact with the wire meshes, which consequently allows for the measurement of the particle's emission without any interference. In contrast with the horizontal mesh configuration, in this study, additional combustion parameters other than the burnout duration were able to be quantified and discussed.

Single particle combustion experiments were conducted to observe the influence of the mass of a olive residue particle on ignition delay, volatile and char combustion times, and burnout times. Tunçbilek lignite was also combusted to compare with olive residue results. In Figure 4.16 and Figure 4.17, olive residue single particle combustion sequences are shown in mid-wave and long-wave infrared, respectively. At the beginning, the particle absorbs the energy radiated from the meshes and at the ignition point volatile combustion begins as flames are formed (see Figure 4.16 (c) for volatile flames). Char combustion follows the volatile combustion stage and the radiating region in the infrared image shrinks as the particle is consumed and burns out. The same single particle combustion experiment series were also conducted for Tunçbilek lignite for comparison purposes only. Homologous spectral band images of Tunçbilek lignite combustion are shown in Figure 4.18 for mid-wave and Figure 4.19 for long-wave infrared. Qualitative inspection on olive residue particles shows that the volatile

flames are more distinguishable in mid-wave than long-wave infrared. Moreover, in Tunçbilek lignite single particle combustion, volatile flames and combustion cannot be distinguished (see Figure 4.18 (c) and Figure 4.19 (c) for both bands). This result indicates that Tunçbilek lignite particle combusts in a single phase during which volatiles and char combust simultaneously as observed in a previous study (Riaza, Ajmi, et al., 2017) of coal single particle combustion experiments in a wire mesh reactor.

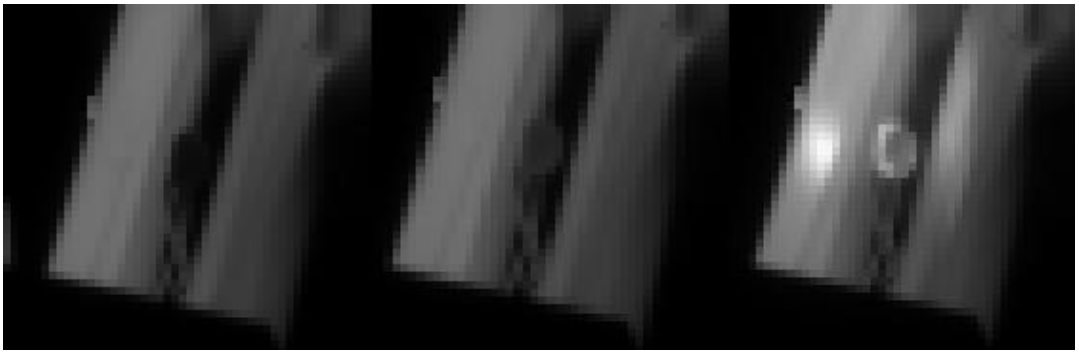

(a) (b) (c)

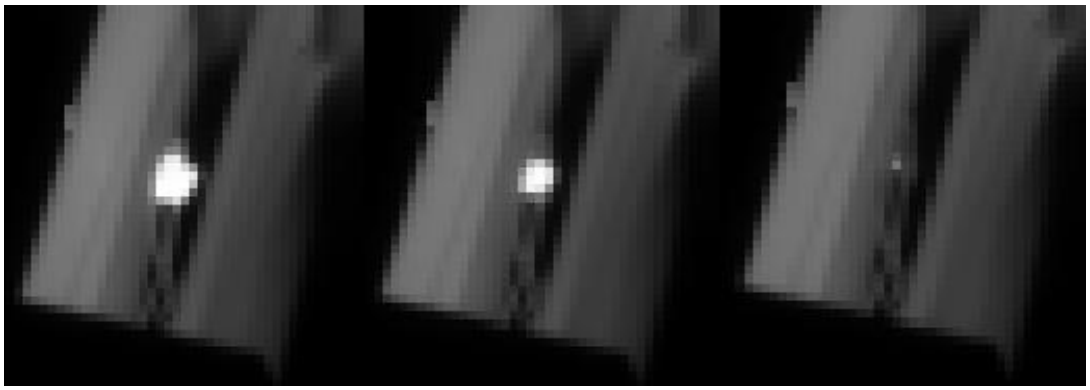

(d) (e) (f)

Figure 4.16. Mid-wave Infrared Images of the Combustion Phases of a 10 mg Olive Residue Single Particle: (a) particle heat up (b) further particle heat up and pre-ignition (c) ignition and volatile combustion (d) char combustion (e) char shrinkage (f) burnout

(a) (b) (c)

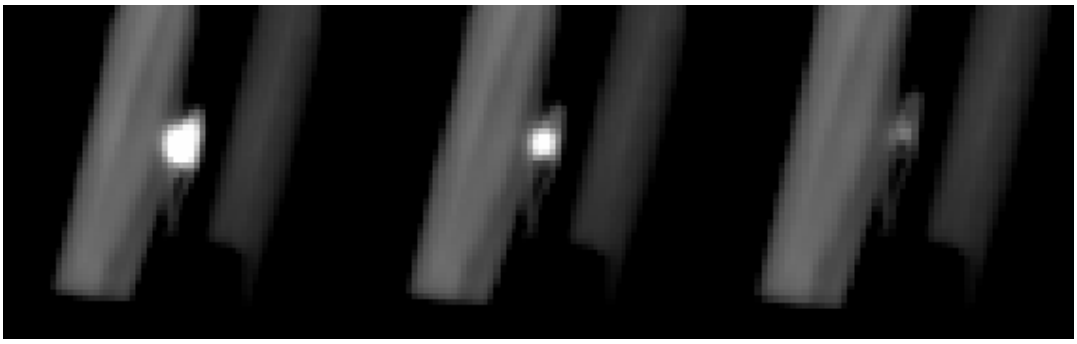

(d) (e) (f)

Figure 4.17. Long-wave Infrared Images of the Combustion Phases of a 10 mg Olive Residue Single Particle: (a) particle heat-up (b) further particle heat-up and pre-ignition (c) ignition and volatile combustion (d) char combustion (e) char shrinkage (f) burnout

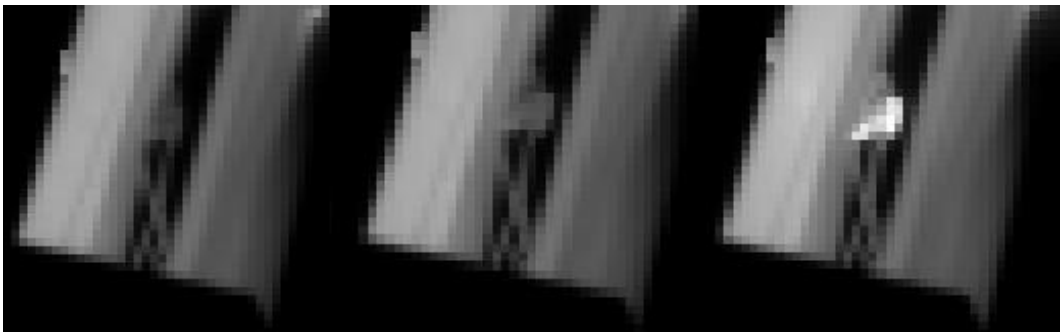

(a) (b) (c)

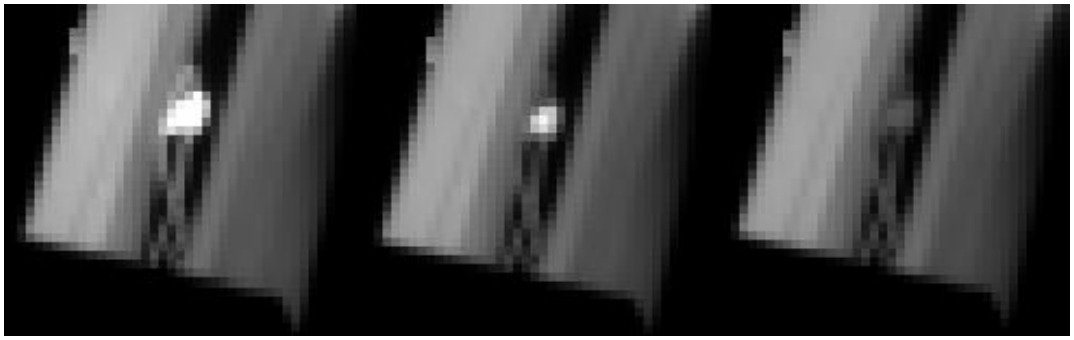

(d) (e) (f)

Figure 4.18. Mid-wave Infrared Images of the Combustion Phases of a 3 mg Tunçbilek Lignite Single Particle: (a) particle heat-up (b) further particle heat-up and pre-ignition (c) ignition (d) volatile and char combustion (e) char shrinkage (f) burnout

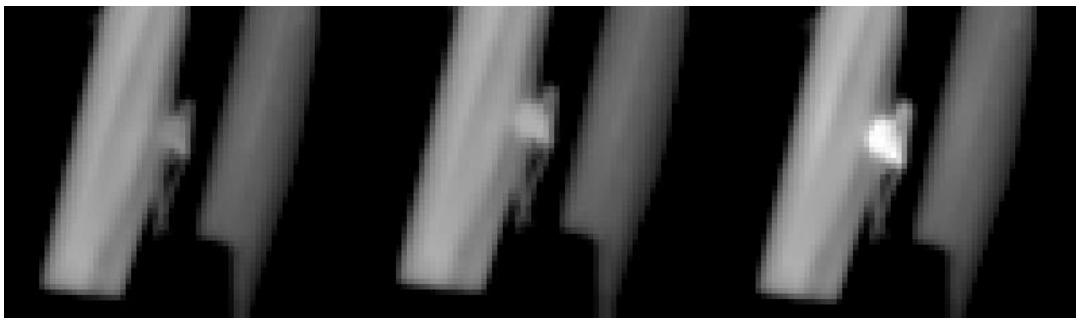

(a) (b) (c)

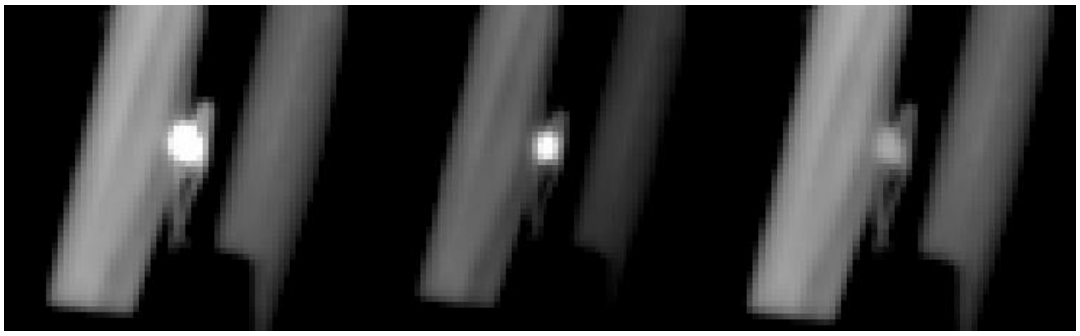

(d) (e) (f)

Figure 4.19. Long-wave Infrared Images of the Combustion Phases of a 3 mg Tunçbilek Lignite Single Particle: (a) particle heat-up (b) further particle heat-up and pre-ignition (c) ignition (d) volatile and char combustion (e) char shrinkage (f) burnout

4.2.1. Ignition Delay Time Results

The ignition delay time of single particle olive residue was calculated and plotted as a function of the particle mass, in mid-wave and long-wave infrared bands as shown in Figure 4.22 and Figure 4.23 respectively. As explained in previous sections, olive residue has two distinct combustion phases and the ignition delay time corresponds to the gas phase ignition, which is the beginning of the first phase, volatile combustion.

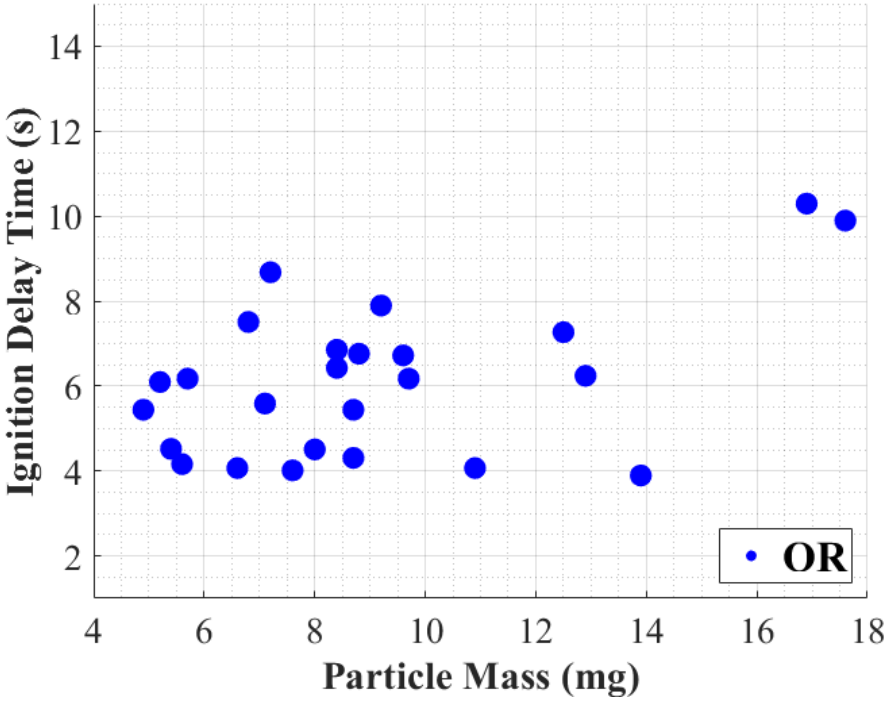

Figure 4.20. Ignition Delay Time versus Particle Mass for Single Particle Olive Residue in Mid-wave Infrared

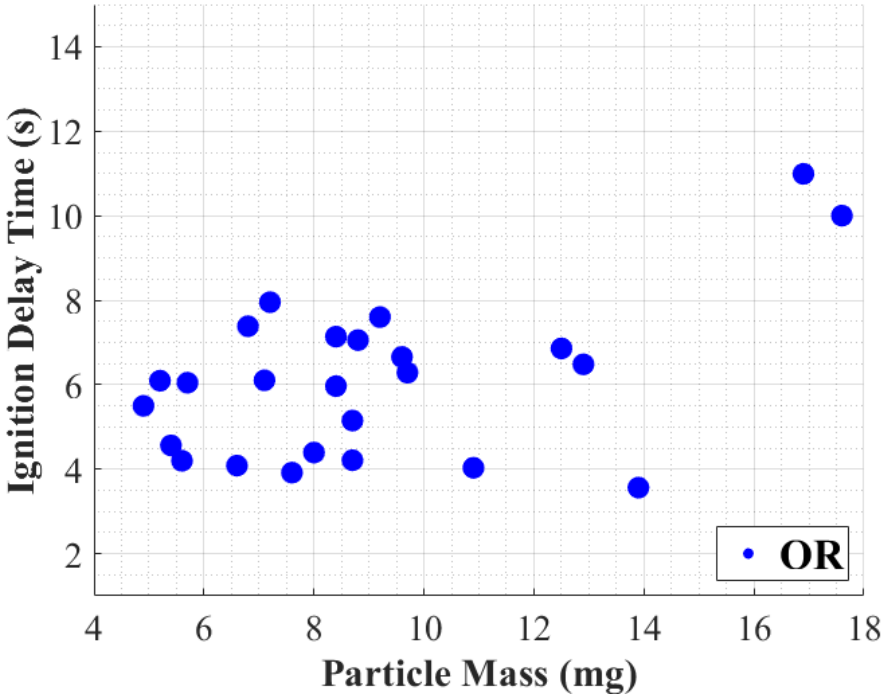

Figure 4.21. Ignition Delay Time versus Particle Mass for Single Particle Olive Residue in Long-wave Infrared

Mathematically, the ignition point can be determined straightforwardly as it is the maximum change of temperature over time in the radiometric heating curve of the particle. Consequently, mid-wave and long-wave infrared were expected to yield consistent results. Since the temperature change in the combustion process also changes the emitted radiation in each band, ignition delay time which is a temporal parameter was expected to be the same in both spectral bands with a negligible error of around 13 milliseconds originating from different sampling rates of the cameras. For each trial, the difference of ignition delay time between mid-wave and long-wave infrared was calculated and it has been found that on average the mid-wave infrared durations are 15 milliseconds longer. The difference can be neglected since the average ignition delay times were longer by two orders of magnitude than the reported 15 milliseconds error.

As the particle mass increases, also with size increase, the ignition delay time tends to increase (Goshayeshi & Sutherland, 2014), however, a strong correlation between particle mass and ignition delay time could not be established. The result can be attributed to the fact that since the ignition occurs in gas phase, and particle mass does not have a direct impact on it. Moreover, at a specific particle mass value, e.g. 8 mg, the variance in ignition delay time is ~4 seconds. This variation can be caused by the non-homogeneity of the olive residue fuel batch and the different shapes of the single particles.

4.2.2. Volatile Combustion Time Results

After the ignition onset of olive residue particles, the volatile combustion begins, and continues until the onset of char ignition which is also defined in previous sections as the inflection point in the radiometric heating curve. The calculated volatile combustion time results from each particle's radiometric heating curve are plotted in Figure 4.22 and Figure 4.23 for mid-wave and long-wave infrared, respectively. Based on the results of combustion in horizontal mesh configuration, it is expected to observe volatile combustion duration longer in mid-wave than long-wave band, since the qualitative results proved that the volatile flames were more detectible in mid-wave infrared. Consequently, quantitative results are expected to demonstrate same physics by the calculated average volatile combustion time of mid-wave infrared being longer than long-wave. In fact, the difference between mid-wave and long-wave infrared results are coherent with the qualitative results as the mid-wave results are 33 milliseconds longer on average than the long-wave results.

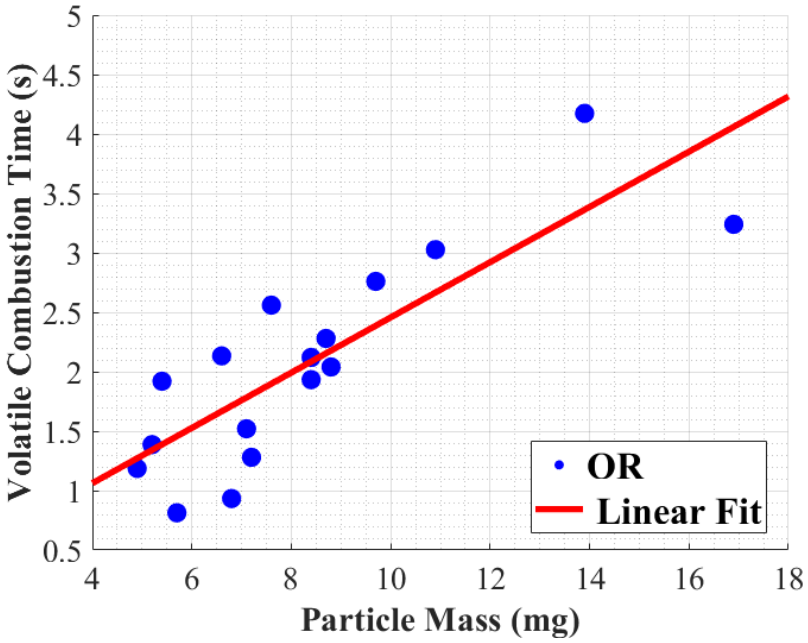

Figure 4.22. Volatile Combustion Time versus Particle Mass for Single Particle Olive Residue in Mid-wave Infrared

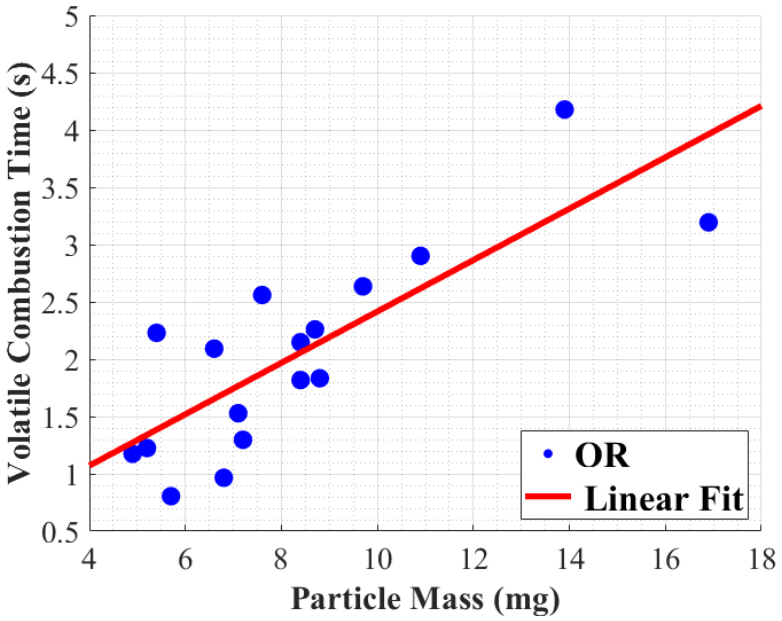

Figure 4.23. Volatile Combustion Time versus Particle Mass for Single Particle Olive Residue in Long-wave Infrared

The effect of single particle mass on volatile combustion time was observed and a linear correlation was found with a R-square value of 0.6546 averaged in both spectral bands (see Appendix A, Volatile Combustion Time section). Correlation of the parameter to particle mass is more distinguishable than on the case of the ignition delay time. This result indicates that the more a particle weighs the more it tends to contain volatile matter in it, consequently the volatile combustion time tends to be longer for both spectral bands.

4.2.3. Char Ignition Delay Time Results

Char ignition point defines the instant when the combustion of volatiles ends, and the char part of the fuel is ignited. The duration until the char ignition point is achieved in radiometric heating curve is called as char ignition delay time. In Figure 4.24 and Figure 4.25, the char ignition delay times of each successful single particle olive residue trials are plotted for mid-wave and long-wave infrared respectively. In summary, this parameter represents the time elapsed until the second phase of combustion of olive residue begins.

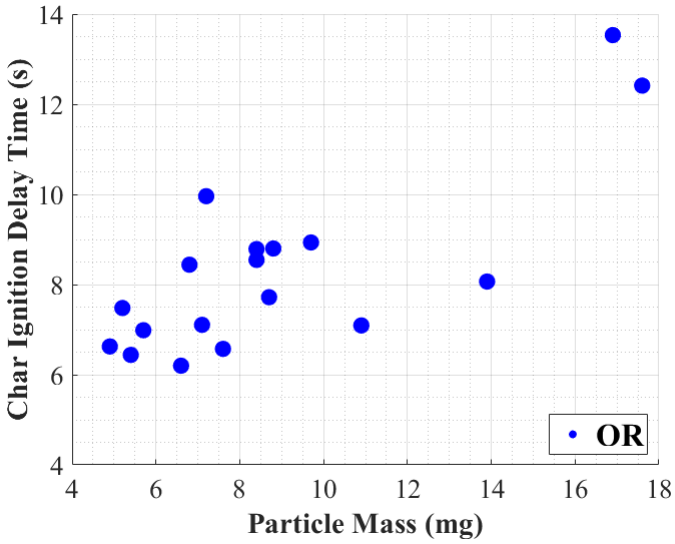

Figure 4.24. Char Ignition Delay Time versus Particle Mass for Single Particle Olive Residue in Mid-wave Infrared

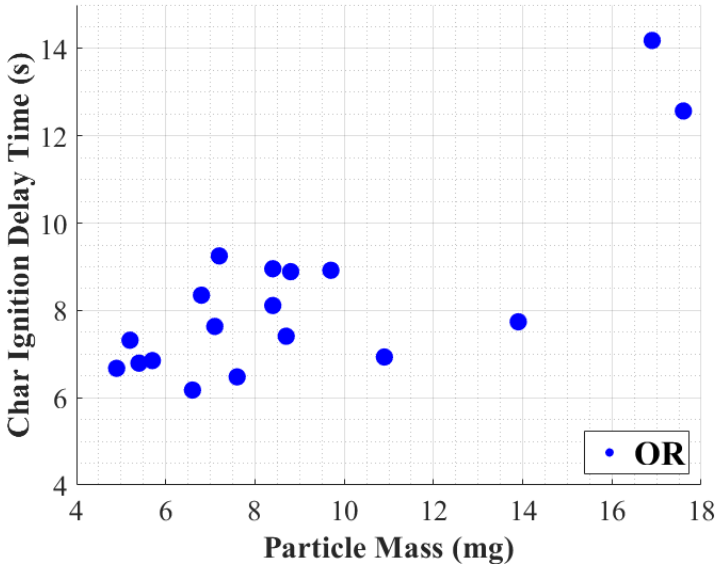

Figure 4.25. Char Ignition Delay Time versus Particle Mass for Single Particle Olive Residue in Long-wave Infrared

Due to the fact that the char ignition occurs in solid-gas phase as opposed to the first ignition mechanism which was in gas-gas phase, the results show a better correlation with the single particle mass. As shown in Figure 4.24 and Figure 4.25, char ignition delay results have higher linear tendency over the particle mass when compared with ignition delay time results.

Comparison of the averaged values in two spectral bands has shown that the difference between them in terms of time was unobservable. The results show that the inflection point in the particle's heating curve (i.e. the point at which the global reaction switches from endothermic type to exothermic), can be distinguished quantitatively both in mid-wave and long-wave infrared. Char ignition delay value considered as important since char ignition requires more time and energy to be achieved. Char ignition delay times can be used for applications in which the devolatilized form of the fuel, olive residue, is utilized and in that case the char ignition delay time becomes the ignition delay time for devolatilized fuel.

4.2.4. Char Combustion Time Results

Char combustion is the second combustion phase for olive residue single particle where the fixed carbon content in the fuel burns and heat radiates during a considerably longer time than volatile combustion. Char combustion time covers the duration between the char ignition and the total burnout of the particle, and it is plotted for each successful trial in Figure 4.26 and Figure 4.27 for mid-wave and long-wave infrared bands, respectively.

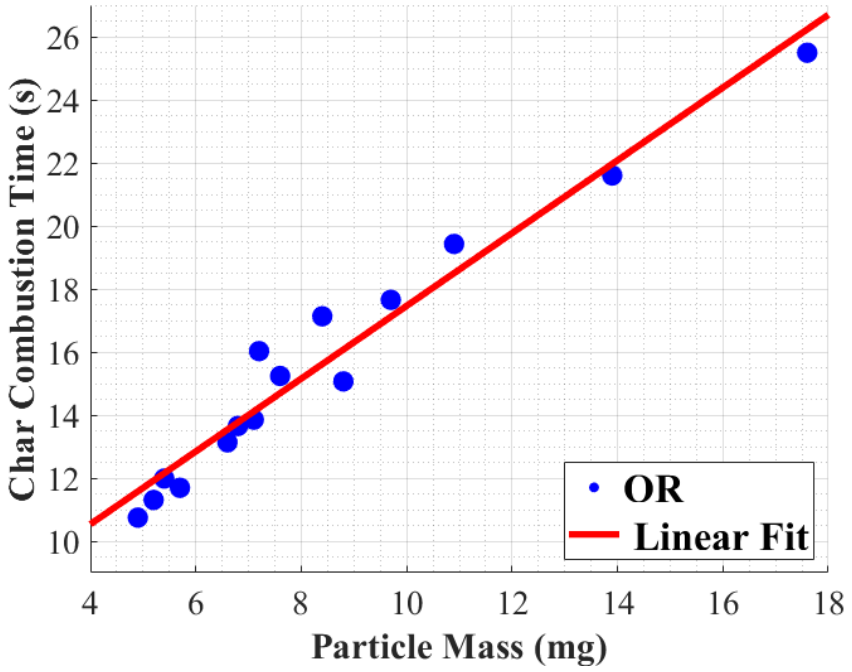

Figure 4.26. Char Combustion Time versus Particle Mass for Single Particle Olive Residue in Mid-wave Infrared

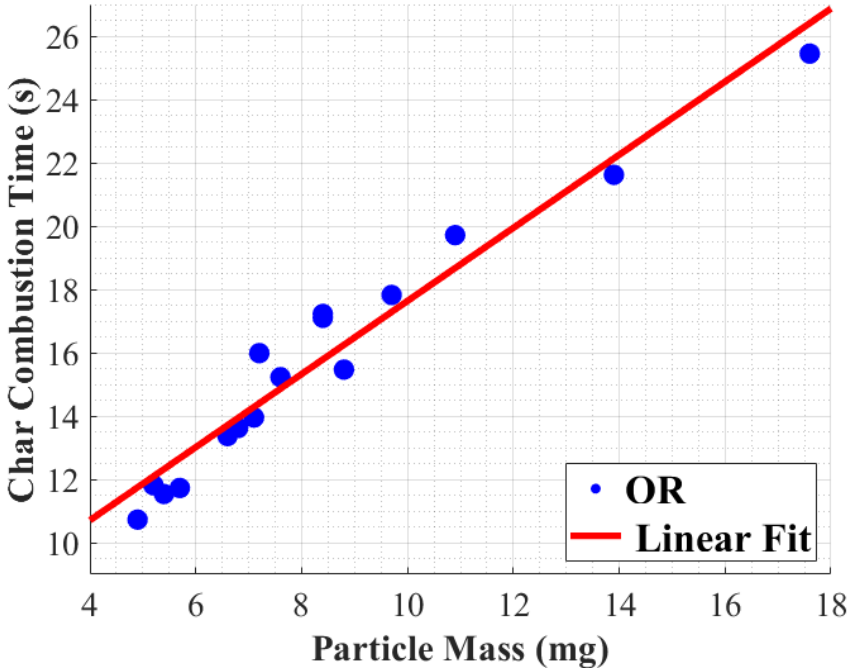

Figure 4.27. Char Combustion Time versus Particle Mass for Single Particle Olive Residue in Long-wave Infrared

The effect of particle mass on char combustion time can be modeled as a linear fit with a R-square value of 0.9481 averaged in both spectral bands as the details are shown in Appendix A, Char Combustion Time section. A correlation between char combustion time and the particle mass is more evident since the R-square value of the char combustion time linear model is larger than the volatile combustion time. As a result of it the devolatilized fuel combusts proportionally to the amount of fixed carbon, char.

On average, long-wave infrared char combustion time results were calculated as 74 milliseconds longer than mid-wave infrared results. Although the amount of difference in time is small when char combustion time's order of magnitude is considered, it can be explained with the fact that the particle's burnout duration was sensed longer by long-wave infrared camera since in burnout phase the temperature

relatively decreases and the particle begins to emit thermal radiation in longer wavelengths in electromagnetic spectrum.

4.2.5. Total Combustion Time Results

The total combustion time covers the duration from the first instant when the particle is ignited until its total burnout. This parameter has a key role when a fuel needs to be co-fired with another fuel. The successful total combustion results of single particle olive residue versus particle mass are plotted in Figure 4.28 and Figure 4.29 for mid-wave and long-wave infrared, respectively. The summation of volatile and char combustion times yields the total combustion time; however, the char combustion time is expected to influence it heavily since it is approximately 10 times longer than the volatile combustion time.

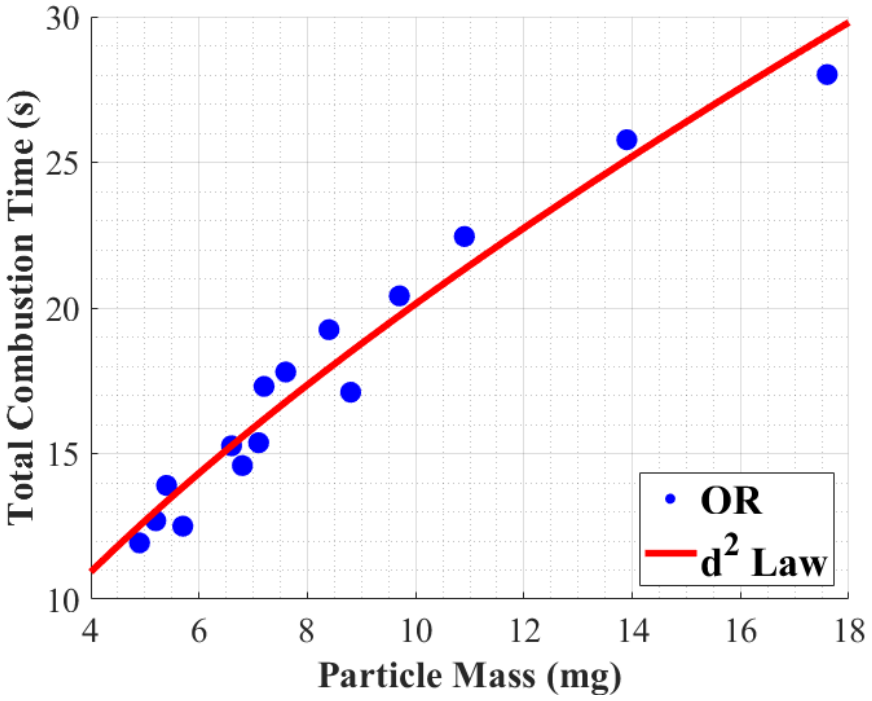

Figure 4.28. Total Combustion Time versus Particle Mass for Single Particle Olive Residue in Mid-wave Infrared

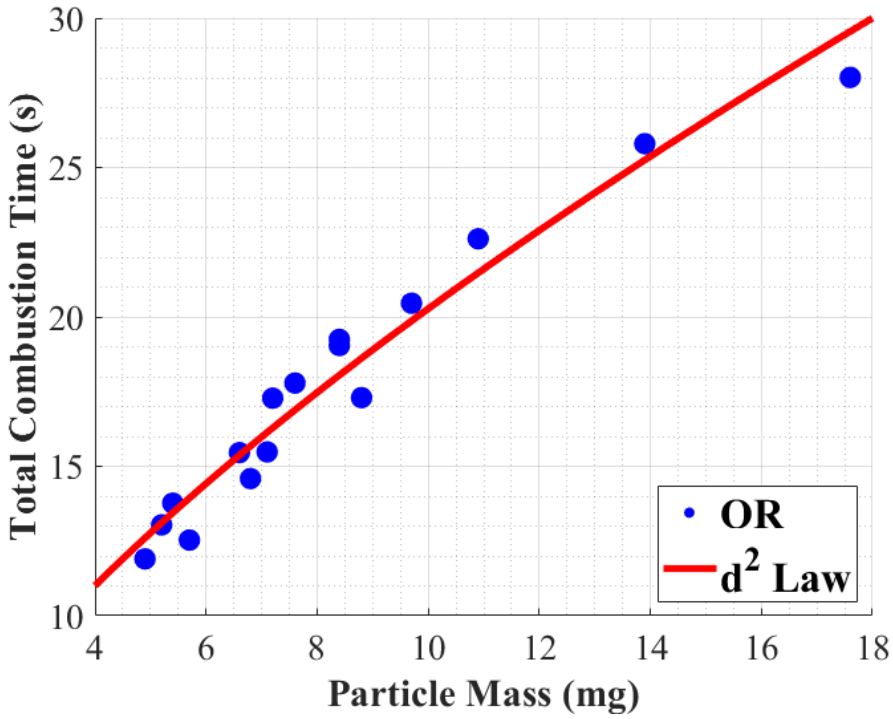

Figure 4.29. Total Combustion Time versus Particle Mass for Single Particle Olive Residue in Long-wave Infrared

The correlation of the total combustion duration with particle mass was found out to be strong and in line with the char combustion time. In Figure 4.28 and Figure 4.29, the single particles were assumed as spherical shape (Rawle, 2003) and the total combustion data were fit into d^2-law which explains droplet combustion (Goddard, 2016) as analogous to single particle combustion (Law, 2006). For olive residue single particle, it can be easily concluded that the combustion duration depends heavily on the particle mass as the average R-square values in both spectral bands for d^2-law is 0.9563 (see Appendix B for d^2-law implementation and subsection 4.2.6 for further discussion on the d^2-law).

The average of all calculated results in each spectral band showed that long-wave infrared results are 40 milliseconds longer than mid-wave results. For the volatile combustion time, mid-wave camera was able to distinguish the stage on average for a

longer duration and in char combustion stage long-wave camera sensed the stage longer; this means that in the total combustion time, due to the fact that char combustion dominates, long-wave cameras are able to detect a longer duration of the total combustion process. Nevertheless, this difference for each spectral band can be considered as negligible when compared with the total combustion times.

4.2.6. Discussion

Comparison of olive residue burning times with literature results

In order to validate the obtained vertical configuration results in this thesis, other single particle biomass combustion experiments are compared in which the same combustion characteristics were analyzed. Since there is no previous Turkish olive residue single particle combustion study in the literature for similarly sized particles, similarities and differences between the combustion characteristics were discussed with the closest results found in the literature in terms of fuel and test conditions.

Single particle biomass combustion experiments of European ash (Fraxinus excelsior) were conducted in a wire mesh reactor operated at 900 °C (Flower & Gibbins, 2009). The mass of selected particles varied roughly from 5 to 25 milligrams, similarly, olive residue particles in this research were 5 to 17 milligrams. In Figure 4.30, combustion characteristics of the biomass fuel are plotted. The results show that; volatile, char and total combustion (burnout) times have increased for heavier particles. Additionally, the correlation between combustion times and the particle mass was plotted as a linear function. The outcomes are on par with the results of olive residue single particle combustion as the results were also presented by a linear fitting in the sections 4.2.2, 4.2.4. On average, the burning time of a 10 milligram European ash particle was ~12.5 seconds: ~5 seconds for volatile combustion and ~7.5 seconds for char combustion. Herein, an olive residue particle with the same weight, totally combusted in ~20 seconds where ~2 and ~18 seconds were volatile and char combustions respectively. Evidently, the volatile burning time was halved for olive residue and the char burning

time doubled, when compared with the European ash studied (Flower & Gibbins, 2009). The shorter devolatilization times measured herein are likely a consequence of the higher surface area of elongated olive residue particles that permitted a faster devolatilization, unlike the cube like particles used.

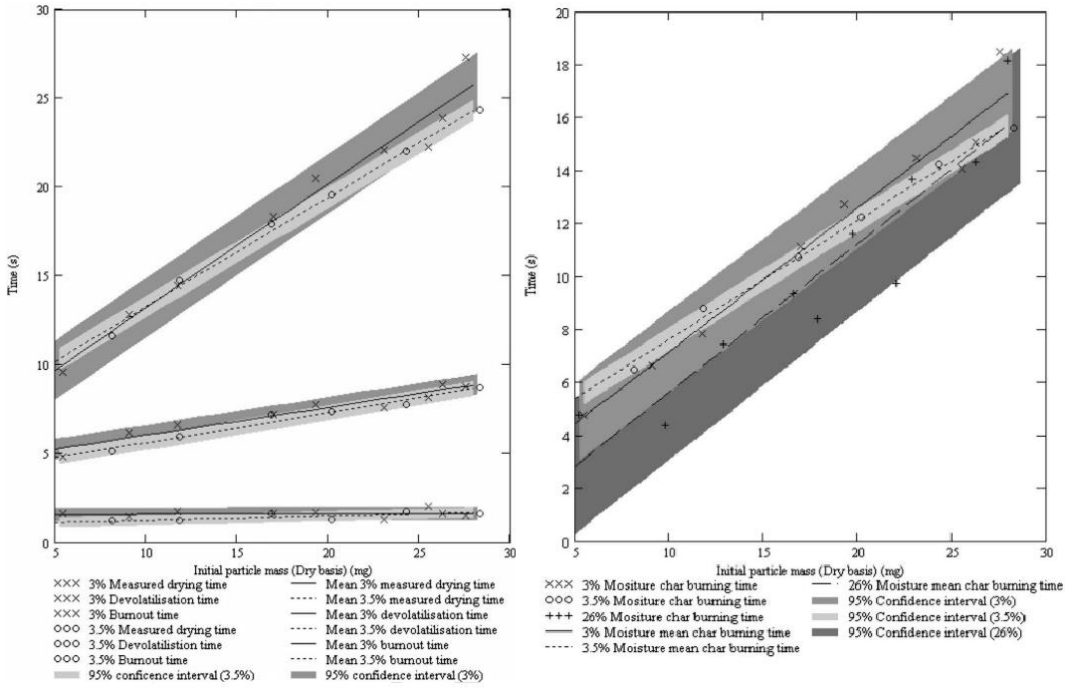

Figure 4.30. European Ash Devolatilization, Burnout Time (left-hand side) and Char Burning Time (right-hand side) Graphs for Different Moisture Percentages (Flower & Gibbins, 2009)

Other researchers (Mason et al., 2015) have observed the combustion of single particles of biomass such as pine, eucalyptus and willow in an entrained gas flow. Although the combustion setup is different from the wire mesh reactor, similar particles with initial mass ranging 1-20 milligrams were used. In Figure 4.31, ignition delay time of three biomasses were plotted. In line with the results obtained herein (see subsection 4.2.1), the study concludes that particle mass does not directly influence the ignition delay time.

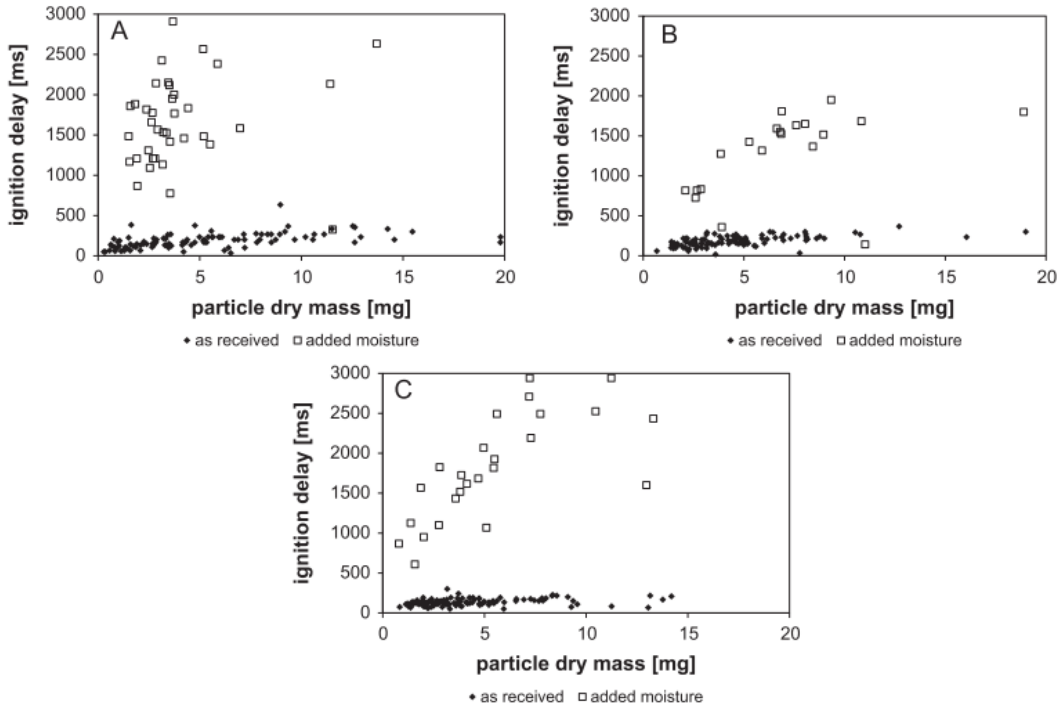

Figure 4.31. Ignition Delay Time of Pine (A), Eucalyptus (B), Willow (C) Single Biomass Particles (Mason et al., 2015)

Moreover, it was also observed (Mason et al., 2015) a linear dependence of the char combustion time of pine, eucalyptus and willow particles as presented in Figure 4.32. Similarly, olive residue char combustion times did also show the same linear dependence trend in this study.

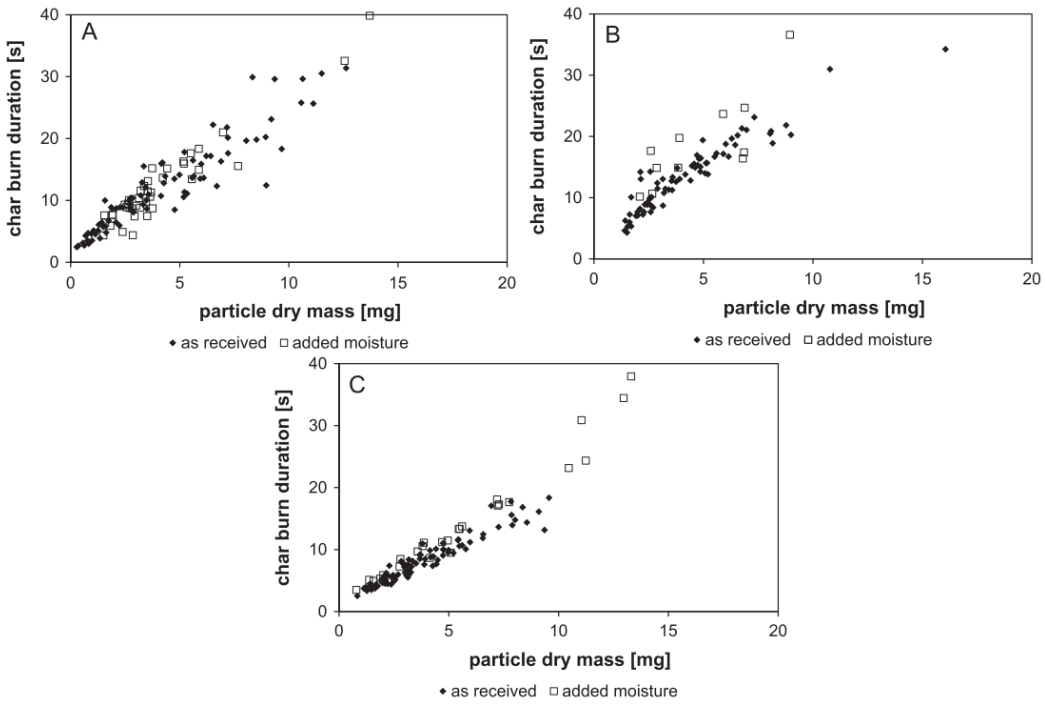

Figure 4.32. Char Combustion Time of Pine (A), Eucalyptus (B), Willow (C) Single Biomass Particles (Mason et al., 2015)

On the potential of olive residue towards co-firing with Tunçbilek lignite

As a part of this thesis, Tunçbilek single particles were also combusted for comparative purposes and to assess the potential of olive residue to be co-fired in existing Tunçbilek lignite boilers. One phase combustion in which the volatile and char parts of the fuel ignite together is expected from single particle combustion of Tunçbilek lignite coal, and the heating curve of a 3 mg single particle combustion is plotted orderly in Figure 4.33 and for mid-wave and long-wave infrared.

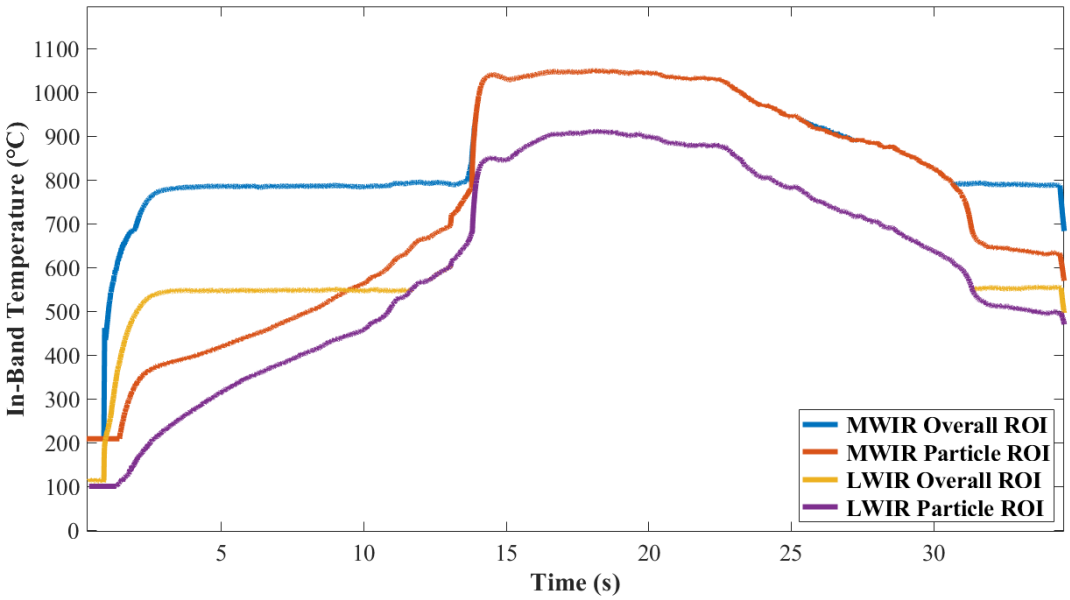

Figure 4.33. Heating Curve in Mid-wave and Long-wave Infrared of a 3 mg Tunçbilek Lignite Particle

Unlike olive residue biomass combustion radiometric curves, Tunçbilek lignite did not present two distinct combustion modes in neither spectral band. Therefore, volatile and char combustion times cannot be defined when a single particle of Tunçbilek lignite combustion is measured remotely by broadband infrared cameras in a wire mesh reactor. Accordingly, only the total combustion times are reported for Tunçbilek lignite.

The total combustion time reflects the importance of the fuel milling process in power plants as the particle size affects the combustion efficiency. The results of single particle Tunçbilek lignite combustion averaged for particle mass of ~ 3 mg showed that the total combustion time was approximately 21.5 seconds. When the same total combustion duration for olive residue single particles are achieved from d^2-law fits in Figure 4.28 and Figure 4.29, ~11 mg fuel was found to correspond to that duration. Thus, olive residue particles are allowed to have a mass three-fold that of Tunçbilek lignite and still reach burnout in the same time period. A lignite coal has a density ~766 kg/m^3 (Sciazko et al., 2016) and olive residue typically has ~570 kg/m^3 density

(Calero, Blazquez, Perez, & Ronda, 1966). Based on these density values, the results in this study show that, for a spherical particle geometry assumption a Tunçbilek lignite particle of 2 mm diameter size combusts in the same time as a 3.3 mm diameter olive residue particle. This means that, to co-fire olive residue with Tunçbilek lignite, the biomass particles do not need to be milled to diameters as low as the coal particles, hence allowing to reduce milling costs. Further quantitative investigation is required on the particle diameter of each fuel that will results in similar burnout times since particle density may change within the same fuel batch and the particle diameter is the required parameter for milling purposes.

Effect of the combustion equipment on the combustion mode of olive residue and Tunçbilek lignite

The effect of the combustion equipment on the single particle combustion mode of olive residue and Tunçbilek lignite can also be discussed. Single particle studies rely on widely used setups such as wire mesh reactors, drop tube furnaces, and entrained flow reactors that provide conditions (e.g. heat transfer modes, temperature, heating rate, residence time, gas composition (Rabacal, Pereira, & Costa, 2018)) similar to those encountered in larger scale furnaces. Nonetheless, the conditions reached by these setups differ and affect the combustion process of the fuel. On the one hand, the main heat transfer mode in a drop tube furnace is convection and the heating rate is of the order of 10^5 ^oC s^{-1}, while on the other hand in a wire mesh reactor radiative heat transfer dominates and the heating rate is comparatively lower (~ 10^3 ^oC s^{-1}).

In the present study olive residue combusted in two phases and Tunçbilek lignite in one phase. The combustion of olive residue appears to be dominated by the large amount (see Table 3.1) and fast release of low density volatiles that quickly ignite and form a cloud that prevents oxygen diffusion inwards onto the particle surface, for either wire mesh reactor (results of this study) or drop tube furnace (Magalhães, Panahi, et al., 2019). This results in a two-phase combustion process in which the char

ignites immediately after the volatiles are extinguished. In contrast, due to the lower volatile content of Tunçbilek lignite (see Table 3.1), ignition and combustion are more dependent on how quickly these volatiles are converted and released. For this fuel, the lower heating rates in the wire mesh reactor allow for the particle to heat up and ignite before a sufficient amount of volatiles has been released to block oxygen diffusion, and a one-phase combustion is registered. This is also in line with other results obtained using a thermogravimetric analyzer (TGA) at low heating rates (Magalhães, Kazanç, Riaza, et al., 2017). In drop tube furnace, however, the higher heating rates allow for a quick devolatilization and ignition of the volatiles before the char particle ignites, and a two-phase combustion is observed.

Applicability of d^2-law to olive residue single particle combustion

The olive residue single particles under the combustion test conditions in this study combusted in accordance with d^2-law that was also accepted as applicable for single particle combustion (Law, 2006). Goodness of the d^2-law fit indicates that the total combustion time results obtained in this thesis represent the combustion physics sufficiently (see Appendix B for goodness of fit, d^2-law implementation and coefficient). Fittings of d^2-law are represented in Figure 4.28 and Figure 4.29. It should be noted that, as explained in Appendix B, the d^2-law applied herein is in fact a modified version since it correlates the total combustion time of a particle with its mass rather than its diameter. The need to apply this modified law was the absence of information on the density of the studied olive residue particles.

CHAPTER 5

CONCLUSIONS AND FUTURE WORK

In this study, a wire mesh reactor was thermally scanned to check temperature uniformity by two broadband infrared cameras, mid-wave and long-wave, and validated as suitable for combustion experiments. Single particle combustion experiments of a biomass, Turkish olive residue, were conducted and the thermal radiation from the processes were recorded and analyzed in mid-wave and long-wave infrared bands. The ignition and combustion times were calculated from radiometric signals and the results were discussed by comparing with Tunçbilek lignite single particle combustion results.

In this section, the outcomes of the conducted study and the main conclusions are presented. Moreover, an outline of possible future researches having the presented work as a starting point is provided.

5.1. Conclusions

In the thermal scanning part of the wire mesh reactor, it has been concluded that the wire mesh can operate at constant high temperature(s) and maintain a uniform temperature distribution with an acceptable temperature deviation throughout the mesh. This result has shown that the setup can supply a homogeneous heat flux to the fuel particle or particle(s) under analysis.

Additionally, as a validation section of the setup, heating and cooling rates of the wire mesh were able to be detected with a non-intrusive method, infrared remote sensing. The heating rate is a crucial parameter as it determines the combustion behavior, and

the cooling rate was stated to determine the amount of time required between two consequent experiments.

A single layer of pulverized olive residue combustion experiments were conducted in horizontal configuration of the wire mesh, and two phase ignition was observed for olive residue in both spectral bands; in addition, in mid-wave infrared the volatile flames were found to be more distinguishable when compared to long-wave results.

The effect of reusing the same wire mesh in two consecutive experiments in which the fuel is in contact with the mesh has been investigated. It was concluded that after the combustion, fuel ash contaminated the wire mesh. This contamination affected the uniform temperature distribution along the mesh and resulted in different physical conclusions in different spectral bands due to the spectral emissivity characteristics of the ash. Consequently, if the fuel is in contact with the wire mesh, the latter cannot be used for a second time in combustion trials in which non-intrusive measuring methods are used.

In single particle combustion experiments, combustion parameters were measured and analyzed. It has been concluded that as the ignition delay time tends to increase for olive residue as its particle mass increases. Due to the fact that the ignition of volatiles occurs in the gas phase, a direct relation of the delay time with the particle mass was not observed.

In contrast with the volatile ignition delay, char ignition occurs in solid form and as a result of it char ignition delay has presented a better correlation with the particle mass. The char ignition point was found to be the same in each spectral band and as a conclusion as the particle's mass increases the char ignition delay time tends to increase.

Other than the ignition times, volatile and char combustion times of the single particle olive residue were analyzed. Both were found out to be dependent on the particle mass, an increase in mass enlarged the volatile and char combustion together. Although both durations were increased, the dependency on mass was much higher in char

combustion time. Volatile combustion time was distinguished 33 milliseconds longer in mid-wave infrared and char combustion was longer by 74 milliseconds in long-wave infrared.

Both infrared band results showed that the total combustion time abides to the d^2-law and that the duration increases with the particle mass. Increase of combustible content directly impacted the total combustion time. Tunçbilek lignite single particle combustion experiment has also been conducted and the total combustion times were compared. The comparison resulted in the fact that in order to achieve the same combustion durations of a 3 milligrams single particle Tunçbilek lignite (2 mm equivalent diameter), a heavier 11 milligrams olive residue particle (3.3 mm equivalent diameter) has to be combusted.

5.2. Future Research

As a future research, not only 3 milligrams of Tunçbilek lignite but various masses of single particles can be used as fuel in experiments. The combustion data of various masses of particles can be used to generate a tendency line between combustion times and particle mass of Tunçbilek lignite so that the comparison between olive residue will be stronger and represent wider range of particle size which eventually establishes more useful relations for milling and power plant applications. If there exists a possibility in which other indigenous Turkish coal(s) can be co-fired with olive residue, conducting the same experimental methodology as in this work will also yield useful data for the future.

In single particle combustion experiments, more than one heating rate and operating temperature can be set to observe, how those parameters effect the ignition modes and combustion durations. Consequently, different combustion systems can be partially emulated and the dependency of volatile and char combustion times on the heating rate and temperature might be concluded.

In this research, broadband infrared cameras were used which integrate the radiance over a wavelength interval. Instead of a broadband infrared camera, a hyperspectral infrared camera that can sense the radiation at specific wavelengths can be utilized. By the help of the hyperspectral data, the spectral radiance of combustion will be able to measure more accurately, hence the in-band temperature values deduced will be closer to the real temperature. Hyperspectral imaging can also enable the plotting of spectral radiance over wavelength so that the radiation originating from biomass or coal combustion can be compared to Planck's radiation curve and the conclusion whether it acts like a gray or selective radiator can be drawn.

REFERENCES

Bejarano, P. A., & Levendis, Y. A. (2008). Single-coal-particle combustion in O2/N2 and O2/CO2 environments. *Combustion and Flame*, *153*(1–2), 270–287. https://doi.org/10.1016/j.combustflame.2007.10.022

Brown, R. C. (2011). *Thermochemical Processing of Biomass* (R. C. Brown, Ed.). https://doi.org/10.1002/9781119990840

Calero, M., Blazquez, G., Perez, A., & Ronda, A. (1966). Characterization of the physical and chemical properties of olive cake for its use as fuel. *The British Journal of Psychiatry*, *112*(483), 211–212. https://doi.org/10.1192/bjp.112.483.211-a

Capper, P., & Elliott, C. T. (2001). *Infrared Detectors and Emitters: Materials and Devices* (Peter Capper & C. T. Elliott, Eds.). https://doi.org/10.1007/978-1-4615-1607-1

Cogliano, J. A. (1963). Apparatus for Rapid Pyrolysis Under Controlled Conditions. *Review of Scientific Instruments*, *34*(4), 439–440. https://doi.org/10.1063/1.1718397

Colthup, N. B., Daly, L. H., & Wiberley, S. E. (1965). Introduction to Infrared and Raman Spectroscopy. In *Journal of the American Chemical Society* (Vol. 87). https://doi.org/10.1021/ja01083a063

Demirbas, A. (2004). Combustion characteristics of different biomass fuels. *Progress in Energy and Combustion Science*, *30*(2), 219–230. https://doi.org/10.1016/j.pecs.2003.10.004

Demirbaş, A. (2002). Fuel characteristics of olive husk and walnut, hazelnut, sunflower, and almond shells. *Energy Sources*, *24*(3), 215–221. https://doi.org/10.1080/009083102317243601

Dhar, N. K., Dat, R., & Sood, A. K. (2013). Advances in Infrared Detector Array Technology. *Optoelectronics - Advanced Materials and Devices*, 13. https://doi.org/http://dx.doi.org/10.5772/57353

Elsaidy, A., Kassem, M., Tantawy, H., & Elbasuney, S. (2018). The Infrared Spectra of Customized Magnesium/Teflon/Viton (MTV) Decoy Flares to Thermal Signature of Jet Engine. *Journal of Engineering Science and Military Technologies*, *17*(17), 1–12. https://doi.org/10.21608/ejmtc.2017.21267

Energy and Natural Resources Ministry of Turkey. (2018). Biomass Potential of Turkey. Retrieved March 25, 2019, from https://www.enerji.gov.tr/tr-tr/sayfalar/biyokutle

EPDK. (2017). *EPDK 2017 Energy Development Report*. Retrieved from http://epdk.gov.tr/Detay/Icerik/3-0-0-102/yillik-rapor-elektrik-piyasasi-gelisim-raporlari

Finch, R. A., & Taylor, R. E. (1969). Apparatus for Determining Thermophysical Properties of Solids by Direct Electrical Pulse Heating. *Review of Scientific Instruments*, *40*(9), 1195–1199. https://doi.org/10.1063/1.1684197

Flower, M., & Gibbins, J. (2009). A radiant heating wire mesh single-particle biomass combustion apparatus. *Fuel*, *88*(12), 2418–2427. https://doi.org/10.1016/j.fuel.2009.02.036

Friedl, A., Padouvas, E., Rotter, H., & Varmuza, K. (2005). Prediction of heating values of biomass fuel from elemental composition. *Analytica Chimica Acta*, *544*(1-2 SPEC. ISS.), 191–198. https://doi.org/10.1016/j.aca.2005.01.041

Gan, M., Fan, X., Chen, X., Ji, Z., Lv, W., Wang, Y., Jiang, T. (2012). *Reduction of Pollutant Emission in Iron Ore Sintering Process by Applying Biomass Fuels*. *52*(9), 1574–1578.

Gilat, A., & Subramaniam, V. (2013). *Numerical Methods for Engineers and Scientists* (3rd ed.). https://doi.org/https://doi.org/10.1017/CBO978113910818

Glassman, I., & Yetter, R. A. (2008). *Combustion* (Fourth). https://doi.org/10.1016/C2011-0-05402-9

Goddard, R. H. (2016). *Diffusion Flames and Heterogeneous Combustion*. Retrieved from https://cefrc.princeton.edu/sites/cefrc/files/combustion-summer-school/lecture-notes/3.-Day-3-Lecture_sharp_with_Special.pdf

Gogebakan, Z., Gogebakan, Y., & Selçuk, N. (2008). Co-firing of olive residue with lignite in bubbling FBC. *Combustion Science and Technology*, *180*(5), 854–868. https://doi.org/10.1080/00102200801894117

Gokcol, C., Dursun, B., Alboyaci, B., & Sunan, E. (2009). Importance of biomass energy as alternative to other sources in Turkey. *Energy Policy*, *37*(2), 424–431. https://doi.org/10.1016/j.enpol.2008.09.057

Goshayeshi, B., & Sutherland, J. C. (2014). A comparison of various models in predicting ignition delay in single-particle coal combustion. *Combustion and Flame*, *161*(7), 1900–1910. https://doi.org/10.1016/j.combustflame.2014.01.010

Gürkan, N. P. (2015). *Turkish Olive And Olive Oil Sectoral Innovation System: A Functional - Structural Analysis*. Middle East Technical University.

H Liu, B. G. (1995). The significance of reburning coal rank on the reduction of NO in drop tube furnace. *8th International Symposium on Transport Phenomena in Combustion*.

InfraTec. (2019). Electromagnetic Spectrum. Retrieved March 28, 2019, from

https://www.infratec.eu/sensor-division/service-support/glossary/infrared-radiation/

Jovanovic, R., Milewska, A., Swiatkowski, B., Goanta, A., & Spliethoff, H. (2011). Numerical investigation of influence of homogeneous/heterogeneous ignition/combustion mechanisms on ignition point position during pulverized coal combustion in oxygen enriched and recycled flue gases atmosphere. *International Journal of Heat and Mass Transfer*, *54*(4), 921–931. https://doi.org/10.1016/j.ijheatmasstransfer.2010.10.011

Khatami, R., & Levendis, Y. A. (2011). On the deduction of single coal particle combustion temperature from three-color optical pyrometry. *Combustion and Flame*, *158*(9), 1822–1836. https://doi.org/10.1016/j.combustflame.2011.01.007

Koppejan, J. (2012). *The Handbook of Biomass Combustion and Co-firing*. https://doi.org/10.4324/9781849773041

Law, C. K. (2006). *Combustion Physics*. https://doi.org/10.1017/CBO9780511754517

Leckner, B. (1972). Spectral and total emissivity of water vapor and carbon dioxide. *Combustion and Flame*, *19*(1), 33–48. https://doi.org/10.1016/S0010-2180(72)80084-1

Levendis, Y. A., Joshi, K., Khatami, R., & Sarofim, A. F. (2011). Combustion behavior in air of single particles from three different coal ranks and from sugarcane bagasse. *Combustion and Flame*, *158*(3), 452–465. https://doi.org/10.1016/j.combustflame.2010.09.007

Magalhães, D., Kazanç, F., Ferreira, A., Rabaçal, M., & Costa, M. (2017). Ignition behavior of Turkish biomass and lignite fuels at low and high heating rates. *Fuel*, *207*(x), 154–164. https://doi.org/10.1016/j.fuel.2017.06.069

Magalhães, D., Kazanç, F., Riaza, J., Erensoy, S., Kabaklı, Ö., & Chalmers, H. (2017). Combustion of Turkish lignites and olive residue: Experiments and kinetic modelling. *Fuel*, *203*, 868–876. https://doi.org/10.1016/j.fuel.2017.05.050

Magalhães, D., Panahi, A., Kazanç, F., & Levendis, Y. A. (2019). Comparison of single particle combustion behaviours of raw and torrefied biomass with Turkish lignites. *Fuel*, *241*(October 2018), 1085–1094. https://doi.org/10.1016/j.fuel.2018.12.124

Magalhães, D., Riaza, J., & Kazanç, F. (2019). A study on the reactivity of various chars from Turkish fuels obtained at high heating rates. *Fuel Processing Technology*, *185*(October 2018), 91–99. https://doi.org/10.1016/j.fuproc.2018.12.005

Majumder, A. K., Jain, R., Banerjee, P., & Barnwal, J. P. (2008). Development of a new proximate analysis based correlation to predict calorific value of coal. *Fuel*, *87*(13–14), 3077–3081. https://doi.org/10.1016/j.fuel.2008.04.008

Mandø, M. (2013). Direct combustion of biomass. In *Biomass Combustion Science, Technology and Engineering*. https://doi.org/10.1533/9780857097439.2.61

Marek, E., & Wiatkowski, B. (2015). Experimental studies of single particle combustion in air and different oxy-fuel atmospheres. *Applied Thermal Engineering*, *74*, 61–68. https://doi.org/10.1016/j.applthermaleng.2014.05.026

Mason, P. E., Darvell, L. I., Jones, J. M., Pourkashanian, M., & Williams, A. (2015). Single particle flame-combustion studies on solid biomass fuels. *Fuel*, *151*(2015), 21–30. https://doi.org/10.1016/j.fuel.2014.11.088

Ministry of Customs and Trade. (2018). *2017 Yılı Zeytin ve Zeytinyağı Raporu*.

Modest, M. F. (2013). *Radiative Heat Transfer*. https://doi.org/10.1016/C2010-0-65874-3

Neavel, R. C. (1981). Coal Structure and Coal Science: Overview and Recommendations. *Advances in Chemical Science*, 73–82.

Paterson, N., Kandiyoti, R., Dugwell, D., Wu, L., & Gao, L. (2008). The use of wire mesh reactors to characterise solid fuels and provide improved understanding of larger scale thermochemical processes. *International Journal of Oil, Gas and Coal Technology*, *1*(1/2), 152. https://doi.org/10.1504/ijogct.2008.016737

Rabacal, M., Pereira, S., & Costa, M. (2018). Review of Pulverized Combustion of Non-Woody Residues. *Energy and Fuels*, *32*(4), 4069–4095. https://doi.org/10.1021/acs.energyfuels.7b03258

Rawle, A. (2003). Basic Principles of Particle Size Analysis. In *Malvern Instruments Technical Paper* (Vol. 44). Retrieved from https://www.researchgate.net/publication/279693634_The_Basic_Principles_of_Particle_Size_Analysis

Riaza, J., Ajmi, M., Gibbins, J., & Chalmers, H. (2017). Ignition and Combustion of Single Particles of Coal and Biomass under O2/CO2 Atmospheres. *Energy Procedia*, *114*(November 2016), 6067–6073. https://doi.org/10.1016/j.egypro.2017.03.1743

Riaza, J., Gibbins, J., & Chalmers, H. (2017). Ignition and combustion of single particles of coal and biomass. *Fuel*, *202*, 650–655. https://doi.org/10.1016/j.fuel.2017.04.011

Riaza, J., Khatami, R., Levendis, Y. A., Álvarez, L., Gil, M. V., Pevida, C., Pis, J. J. (2014a). Combustion of single biomass particles in air and in oxy-fuel conditions. *Biomass and Bioenergy*, *64*, 162–174. https://doi.org/10.1016/j.biombioe.2014.03.018

Riaza, J., Khatami, R., Levendis, Y. A., Álvarez, L., Gil, M. V., Pevida, C., Pis, J. J. (2014b). Single particle ignition and combustion of anthracite, semi-anthracite

and bituminous coals in air and simulated oxy-fuel conditions. *Combustion and Flame*, *161*(4), 1096–1108. https://doi.org/10.1016/j.combustflame.2013.10.004

Riaza, J., Mason, P., Jones, J. M., Gibbins, J., & Chalmers, H. (2019). High temperature volatile yield and nitrogen partitioning during pyrolysis of coal and biomass fuels. *Fuel*, *248*(July 2018), 215–220. https://doi.org/10.1016/j.fuel.2019.03.075

Richards, P. L. (2013). *Bolometers for infrared and millimeter waves Bolometers for infrared and millimeter waves*. *1*(1994). https://doi.org/10.1063/1.357128

Robinson, L. C., & Moeller, K. D. (1974). Methods of Experimental Physics, Volume 10: Physical Principles of Far-Infrared Radiation. *Physics Today*, *27*(1), 78–79. https://doi.org/10.1063/1.3128402

Rubio, B., Mayoral, M. C., Izquierdo, M. T., & Andre, J. M. (2001). Different approaches to proximate analysis by thermogravimetry analysis. *Thermochimica Acta*, *370*, 91–97.

Sami, M., Annamalai, K., & Wooldridge, M. (2001). Co-firing of coal and biomass fuel blends. *Progress in Energy and Combustion Science*, *27*(2), 171–214. https://doi.org/10.1016/S0360-1285(00)00020-4

Sciazko, A., Komatsu, Y., Zakrzewski, M., Akiyama, T., Hashimoto, A., Shikazono, N., Kobayashi, Y. (2016). Experimental attempts to investigate the influence of petrographic properties on drying characteristics of lignite in superheated steam atmosphere. *Energies*, *9*(5). https://doi.org/10.3390/en9050371

Shan, L., Kong, M., Bennet, T. D., Sarroza, A. C., Eastwick, C., Sun, D., Liu, H. (2018). Studies on combustion behaviours of single biomass particles using a visualization method. *Biomass and Bioenergy*, *109*(September 2017), 54–60. https://doi.org/10.1016/j.biombioe.2017.12.008

Soldani, M. F. (2015). Infrared signature: Theory and example of practical measurement methods. *2nd IEEE International Workshop on Metrology for Aerospace, MetroAeroSpace 2015 - Proceedings*, 472–478. https://doi.org/10.1109/MetroAeroSpace.2015.7180703

Stewart, S. M., & Johnson, R. B. (2016). *Blackbody Radiation*. https://doi.org/10.1201/9781315372082

Trubetskaya, A. , Glarborg, P. , Jensen, P. A., Jensen, A. D., & Shapiro, A. (2016). Fast pyrolysis of biomass at high temperatures.

van Lith, S. C., Alonso-Ramirez, V., Jensen, P. A., Frandsen, F. J., & Glarborg, P. (2006). Release to the gas phase of inorganic elements during wood combustion. Part 1: Development and evaluation of quantification methods. *Energy and Fuels*, *20*(3), 964–978. https://doi.org/10.1021/ef050131r

Vassilev, S. V., Kitano, K., & Vassileva, C. G. (1996). Some relationships between coal rank and chemical and mineral composition. *Fuel*, *75*(13), 1537–1542. https://doi.org/10.1016/0016-2361(96)00116-0

WHO. (2013). Air Pollution and Cancer - IARC Scientific Publication No. 161. In *International Agency for Research on Cancer*. https://doi.org/10.1007/s13398-014-0173-7.2

Yang, Y. B., Sharifi, V. N., Swithenbank, J., Ma, L., Darvell, L. I., Jones, J. M., Williams, A. (2008). Combustion of a single particle of biomass. *Energy and Fuels*, *22*(1), 306–316. https://doi.org/10.1021/ef700305r

Yuzbasi, N. S., & Selçuk, N. (2011). Air and oxy-fuel combustion characteristics of biomass/lignite blends in TGA-FTIR. *Fuel Processing Technology*, *92*(5), 1101–1108. https://doi.org/10.1016/j.fuproc.2011.01.005

Zhang, Li, Xu, S., Zhao, W., & Liu, S. (2007). Co-pyrolysis of biomass and coal in a free fall reactor. *Fuel*, *86*(3), 353–359. https://doi.org/10.1016/j.fuel.2006.07.004

Zhang, Linghong, Xu, C. (Charles), & Champagne, P. (2010). Overview of recent advances in thermo-chemical conversion of biomass. *Energy Conversion and Management*, *51*(5), 969–982. https://doi.org/10.1016/j.enconman.2009.11.038

Zygarlicke, C., McCollor, D., & Crocker, C. (1999). Ash Emissivity Characterization and Prediction. In *U.S. Department of Energy - NETL*.

APPENDICES

A. Linear Fitting

Linear model used in data fitting is shown below,

$$t = p_1 m + p_2$$

where m is particle mass, t is relevant combustion time and p_1, p_2 are the coefficients of the linear model.

- Volatile Combustion Time Linear Fit

  Mid-wave Infrared:
  Coefficients with 95% confidence bounds:

  $$p1 = 0.2324\ (0.1454, 0.3194)$$
  $$p2 = 0.133\ (-0.6418, 0.9078)$$

  Goodness of fit:
  Sum of Squares Due to Error (SSE) = 3.974
  R-Square = 0.6837
  Adjusted R-Square = 0.6626
  Root Mean Square Error (RMSE) = 0.5147

  Long-wave Infrared:
  Coefficients with 95% confidence bounds:

  $$p1 = 0.2242\ (0.1329, 0.3154)$$
  $$p2 = 0.1747\ (-0.6379, 0.9872)$$

  Goodness of fit:
  Sum of Squares Due to Error (SSE) = 4.37
  R-Square = 0.6465

Adjusted R-Square = 0.6229

Root Mean Square Error (RMSE) = 0.5398

- Char Combustion Time Linear Fit

Mid-wave Infrared:

Coefficients with 95% confidence bounds:

$$p1 = 1.154\ (1.005, 1.304)$$

$$p2 = 5.921\ (4.569, 7.273)$$

Goodness of fit:

Sum of Squares Due to Error (SSE) = 10.67

R-Square = 0.9554

Adjusted R-Square = 0.9519

Root Mean Square Error (RMSE) = 0.9058

Long-wave Infrared:

Coefficients with 95% confidence bounds:

$$p1 = 1.155\ (0.9994, 1.31)$$

$$p2 = 6.087\ (4.69, 7.485)$$

Goodness of fit:

Sum of Squares Due to Error (SSE) = 12.56

R-Square = 0.9479

Adjusted R-Square = 0.9442

Root Mean Square Error (RMSE) = 0.9472

B. d^2-Law Implementation

The d^2-law of droplet burning is considered analogous to single particle solid combustion mechanism. The law is given below,

$$t = \frac{r^2}{K}$$

where t is total combustion time, r is the spherical particle radius and K is a constant that includes thermophysical values of the fuel.

The particles are assumed to be in a spherical shape with the same density, hence the following relation is obtained,

$$\frac{m}{\rho} = \frac{4}{3}\pi r^3$$

where m is the particle mass, ρ is density and r is the spherical radius of the particle.

Then the d^2-law can be rewritten in terms of mass as,

$$t = \left(\frac{3}{4\pi\rho}\right)^{2/3} \frac{1}{K} m^{2/3}$$

where π, ρ and K are constants.

The final form is rearranged as,

$$t = Cm^{2/3}$$

where C is a constant.

- Total Combustion Time Fit

  Mid-wave Infrared:

  Coefficient with 95% confidence bounds:

  $$C = 4.339\ (4.207, 4.471)$$

  Goodness of fit:

  Sum of Squares Due to Error (SSE) = 13.96

  R-Square = 0.9571

  Adjusted R-Square = 0.9571

  Root Mean Square Error (RMSE) = 0.9986

  Long-wave Infrared:

  Coefficient with 95% confidence bounds:

  $$C = 4.368\ (4.243, 4.493)$$

  Goodness of fit:

  Sum of Squares Due to Error (SSE) = 14.49

  R-Square = 0.9555

  Adjusted R-Square = 0.9555

  Root Mean Square Error (RMSE) = 0.9827